

UNIVERSITY OF COPENHAGEN
FACULTY OF SCIENCE



Towards a room temperature single photon source based on atomic vapour

PhD Thesis

Michael Zugenmaier

This thesis has been submitted to the
PhD School of the Faculty of Science
University of Copenhagen

**Towards a room temperature
single photon source
based on atomic vapour**

PhD thesis

Michael Zugenmaier

*Center for Quantum Optics (QUANTOP)
Niels Bohr Institute
Graduate School of Science
Faculty of Science
University of Copenhagen*

Academic supervisor: Prof. Eugene S. Polzik

Evaluation committee:

External referees: Prof. Ian Walmsley
Prof. Hugues de Riedmatten

NBI local head: Assoc. Prof. Jens Paaske

Thesis submitted: April 30, 2018

Disputation: June 1, 2018

Abstract

Efficient quantum communication over long distances requires quantum repeaters along the communication line. Quantum repeaters based on room temperature systems offer advantages due to their scalability. However, atomic motion has until now prevented these systems to reach long lifetimes of heralded single collective excitations in room temperature systems. We study the characteristics of vapour cells with anti-relaxation coating which allows for long lifetimes. We demonstrate efficient heralding and readout of single collective excitations created in warm caesium vapour. Using the concept of motional averaging, we can achieve a lifetime of the collective excitation of 0.27 ± 0.04 ms, two orders of magnitude longer than previous warm vapour experiments on the single photon level. We verify the non-classicality of the correlations between heralding and readout fields by a significant violation of the Cauchy-Schwarz inequality with $R = (1.4 \pm 0.1) > 1$. The spectral and temporal analysis of the noise contributions that contaminate the single photon readout allows us to identify leakage of excitation light and intrinsic four-wave mixing as two main contributions. In a proof-of-principle experiment we confirm an experimental solution to suppress the four-wave mixing noise. We discuss possibilities to identify and possibly eliminate the remaining noise sources and thus with an improved setup to advance towards the applicability as an on-demand single photon source.

Resumé

Effektiv kvantekommunikation over store afstande kræver kvanterepetere langs kommunikationslinjen. Kvanterepetere baseret på systemer ved stuetemperatur åbner mulighed for fordele pga. deres skalerbarhed. Dog har atomar bevægelse hidtil forhindret opnåelsen af lange levetider hos enkeltstående kollektive excitationer i systemer ved stuetemperatur. Vi undersøger de egenskaber ved dampceller med antirelaksationbelægning, som muliggør opbevarelsen af lange levetider. Vi demonstrerer effektiv varsling og udlæsning af enkeltstående kollektive excitationer skabt i varm cæsiumdamp. Ved at benytte konceptet bevægelsesmidling kan vi opnå en levetid for den kollektive excitation på 0.27 ± 0.04 ms, to størrelsesordnere længere end forudgående eksperimenter med varm damp på enkeltfotonniveau. Vi verificerer ikke-klassikaliteten af korrelationerne mellem varslings- og udlæsningsfelterne ved et signifikant brud på Cauchy-Schwarz' ulighed med $R = (1.4 \pm 0.1) > 1$. Den spektrale og tidlige analyse af støjbidrag, som besmitter enkeltfotonudlæsningen, tillader os at identificere lækage fra excitationlys og intrinsisk firbølge-mixing som to hovedbidrag. I et proof of principle-eksperiment bekræfter vi en eksperimentel løsning til undertrykkelse af støjen fra firbølge-mixing. Vi diskuterer muligheder for at identificere og muligvis eliminere de tilbageværende støjkilder og derved, gennem en forbedret forsøgsopstilling, avancere mod anvendelse som en on-demand enkeltfotonkilde.

Preface

This thesis represents an attempt to present most of the work that I have been a part of in the research group of professor Eugene Polzik in QUANTOP (the Danish National Research Foundation Center for Quantum Optics) at the Niels Bohr Institute, University of Copenhagen.

All of the experimental efforts reported on have been achieved as a group effort under the conduct of Eugene Polzik. Due to the close collaboration with the PhD student Karsten Dideriksen, there is a certain overlap with his master thesis.

I want to name some of my coworkers here, to all of whom I am very grateful.

First of all, I am very thankful to Karsten Dideriksen for his thorough work on the experiment during all those years and for bringing his good spirit to the lab. Furthermore, I owe him thanks for the help with the Danish abstract in this thesis. A huge thanks also to Boris Albrecht, who started interfacing the setup with computer control and contributed his DLCZ experience to the experiment.

I want to thank Jürgen Appel for getting me started in the beginning, for his scientific curiosity and for the great help with electronics throughout the experiment. I am also grateful to Georgios Vasilakis for introducing me to the cell experiments and for his patient theoretical explanations. I owe thanks to Johannes Borregaard for developing the theory behind the experiment, and for taking his time to explain the derivations in all details.

Furthermore, I want to thank the fellow cell-mates Rodrigo Thomas, Merlin Enault-Dautheribes, Anne Fabricant, Kasper Jensen, Heng Shen and Hans Staerkind for interesting discussions and help with various aspects of the cell experiment. I am grateful to the fiber-group, Stefan Christensen, Jean-Baptiste Béguin and Heidi Sørensen for their welcoming attitude in the beginning of my stay at Quantop.

I want to thank Jörg H. Müller for his patient instruction on daily experimental

and all other issues, and Anders S. Sørensen for his advise regarding theoretical problems.

I am especially grateful to Eugene Polzik for all the support, the mentoring and the trust during all those years.

I want to thank all previous and current members of the Quantop group for a great time together.

Besides, I want to thank my family and especially Anna Ludl, without whose understanding it would not have been possible to accomplish any of this.

Contents

Contents	iii
1 Introduction	1
1.1 Quantum states of light	2
1.1.1 Statistics of light states	3
1.2 Single photon source	4
1.3 Entanglement	4
1.4 Quantum teleportation and entanglement swapping	5
1.5 Quantum repeater and DLCZ-scheme	6
1.6 Vapour cells	8
1.7 This work	9
I Theoretical background	11
2 Theory	13
2.1 The caesium atom	13
2.2 Light-atom interaction	14
2.3 Light interaction with atomic ensembles	16
2.4 Readout	19
2.5 Motional averaging	20
2.6 Four-wave mixing	26
2.7 Input-output relations	28
2.8 Nonclassical correlations	31
2.8.1 Modelling the correlations	32
2.8.2 Lifetime of collective excitations	35
II Experiment	37
3 Experimental methods	39

3.1	Excitation light	39
3.1.1	Narrowed laser via optical feedback	39
3.1.2	Lock cavity	42
3.2	Vapour cell	42
3.2.1	Encapsulated design	44
3.2.2	Laser-bonded design	44
3.2.3	Integrated cavity	45
3.2.4	CO ₂ laser melting and anodic bonding	46
3.2.5	Atomic density	46
3.3	Cell cavity	47
3.4	Filtering and detection	48
3.5	Optical pumping and magnetic field	50
3.6	Experimental control and sequence	52
3.6.1	Frequencies	53
4	Characterization of cells	55
4.1	Figures of merit	55
4.2	Cell transmission	56
4.2.1	Integrated cavity cell	59
4.3	Issue of disappearing atoms	60
4.3.1	Conclusion	62
4.4	Cell cavity drift due to atomic relaxation	62
4.5	Atomic decay and coherence times	64
4.5.1	Continuous MORS	64
4.5.2	Pulsed MORS - characterization of state initialization	66
4.5.3	Pulsed MORS - snapshot of time evolution	67
4.6	Microwave spectroscopy	75
4.6.1	Discussion of microwave spectroscopy results	79
4.6.2	Conclusion of microwave spectroscopy	80
5	DLCZ-type experiment	83
5.1	Scaling with power	84
5.2	Spectrum of write and read fields	86
5.3	Violation of Cauchy-Schwarz inequality	90
5.3.1	Error estimation on correlation values	93
5.4	Spinwave decay	93
5.5	Time evolution of pulses	95
6	Suppression of four-wave mixing	99
6.1	Readout of RF-excitations	99
6.2	Options to suppress four-wave mixing	102
6.2.1	Hyperfine storage	102
6.2.2	Cavity suppression	103
6.2.3	Four-wave mixing detection	103

6.2.4	Polarization selection rules	103
6.2.5	Magic detuning	104
6.3	Read-out on D1 line	105
6.3.1	Setup at 895 nm	105
6.3.2	Comparison of D ₁ and D ₂ : Filter cavity scan	106
6.3.3	Comparison of D ₁ and D ₂ : Read-out pulse shape	108
7	Discussion	111
7.1	Quantum repeater compatibility	112
7.2	Limitations and improvements	113
7.2.1	Increasing the storage time	115
8	Conclusion and outlook	117
III	Appendix	119
A	Write process for Zeeman transition	121
A.1	From Hamiltonian to light-atom coupling θ	121
A.2	Number of classical photons	125
A.3	N_{clas} in terms of optical depth	126
B	Tables of cavity specifications	129
	Bibliography	131

Introduction

In the last decades, quantum information science has been an area of very active research. It is seen as one of the cornerstones of the second quantum revolution [DM03], that is the development of new technologies based on quantum physics. The work presented in this thesis has emerged in this spirit, combining well-established physics with new ideas to find applicable solutions for quantum technologies.

The first quantum revolution occurred at the beginning of the 21st century. Starting from the attempt to describe black-body radiation, quantum mechanics was born and the well-established classical theory of electromagnetic radiation was turned upside down. Historically there had been a lot of dispute whether light was to be considered wave-like or particle like. After the wave theory developed by Huygens and Hooke was confirmed by experimental results of Young's slit experiments and Fresnel's diffraction experiments, the wide-spread belief was that this question had finally been answered in favour of the wave theory. Together with the formalism developed by Maxwell in the second half of the 19th century, the framework for electro-magnetism seemed to be in place. However, when Planck in 1900 required to introduce a quantization of the energy of the electro-magnetic field to be able to describe the frequency dependency of the black-body radiation, this world-view started to change and quantum physics was born. The quantization was then also successfully applied by Einstein to explain the theory of the photo-electric effect in 1905. While the photo-electric effect was first seen as a proof of the quantization of light, it was shown later, that the quantization of the atomic transitions is sufficient to explain the photo-electric effect [LS69]. It took until the 1970's for the field of quantum optics to emerge, a discipline dedicated to study the quantum nature of light. It became apparent that identifying a single photon state and thus contradicting classical theories is very challenging by measuring the photon number distribution, and much simpler by observing the correlations between photodetection events. The main idea for the correlation measurement is that for a classical

field impinging on a semi-reflective beamsplitter there will be measurable intensity both in the reflected and the transmitted beam path. On the contrary, a single light quantum will be either reflected or transmitted, leaving the respective other path empty. The resulting correlation of detection events in both paths allows to identify states of light that cannot be described by classical theory, so-called non-classical states. In the experiment of [Cla74], two photons were produced subsequently from an atomic cascade transition with short-lived intermediate state. The correlations between these two photons were then analysed and shown to be non-classical. A few years later the "antibunching" effect itself was observed [KDM77]. [GRA86] performed a single photon interference effect. They created correlated photon pairs via an atomic cascade transition, then used the detection of one photon to herald the presence of the other. First they identified that this setup performed as a single photon source, then they injected the output into a Mach-Zehnder interferometer and observed single photon interference. Another milestone was the observation of single photons heralded from a spontaneous parametric down-conversion photon pair source on grounds of their statistical properties by [HM86].

We will introduce quantum states of light and their statistical properties in the next subsection. Then, we will briefly touch upon single photon sources and their figures of merit. Entanglement and teleportation and their impact on quantum communication will then be introduced before we move on to quantum repeaters. A short section about vapour cell applications and a presentation of the idea of this work will conclude the introduction.

1.1 Quantum states of light

A coherent state of light is described classically as a stable oscillation of the electro-magnetic field. We can expand any state of light in the basis of coherent states weighted by a quasiprobability distribution. This expansion is called the Glauber-Sudarshan P representation [Gla63] [Sud63]. If the quasiprobability is positive and bounded, then the light is considered classical, otherwise it is non-classical [GK05]. This means that only coherent states and their statistical mixtures are classical states. Examples of classical light are light from thermal sources or coherent laser light. Examples for non-classical light are squeezed states and photon-number states such as a single photon state.

A photon is defined as an elementary excitation of a single mode of the electro-magnetic field. A single photon state can be defined [BFMP13] as the light field for which the measurement with a number-resolving detector of perfect detection efficiency yields one for the mean number and zero for the variance.

1.1.1 Statistics of light states

Let us consider a stable and perfectly coherent beam of light. In a quantum picture one might be tempted to imagine this as a stream of photons with regular time intervals between them. This is however not the case. The discrete nature of the photons will lead to statistical fluctuations of the photon flux. It can be shown that the probability to find k photons within a perfectly coherent beam of light is given by the Poisson distribution [Fox06]

$$p(k) = \frac{\bar{n}^k}{k!} e^{-\bar{n}} \quad (1.1)$$

with average photon number \bar{n} . Light states that follow Poissonian statistics are called coherent states, and typically the output of a laser can be well described by such a state. The Poissonian distribution has a variance $(\Delta n)^2 = \bar{n}$. We can use this fact to classify light by its photon statistics into super-Poissonian, if $(\Delta n)^2 > \bar{n}$, and sub-Poissonian, if $(\Delta n)^2 < \bar{n}$.

It is not difficult to think of light that has super-Poissonian statistics. Any excess classical intensity fluctuation on a coherent state will lead to an increased variance. Sub-Poissonian light, on the other hand, has a narrower distribution than coherent light. There is no classical counter-part for sub-Poissonian light, thus it is called non-classical.

The electromagnetic radiation emitted by a hot object is known as blackbody radiation. It can be shown that for such a thermal light field, considering a single mode, the probability to find k photons is given by [Fox06]

$$p(k) = \frac{1}{\bar{n} + 1} \left(\frac{\bar{n}}{\bar{n} + 1} \right)^k \quad (1.2)$$

where the average photon number is \bar{n} . This thermal state has a variance $(\Delta n)^2 = \bar{n} + \bar{n}^2$ and thus falls into the category of super-Poissonian states.

A sub-Poissonian state of light has to have smaller variance than the coherent state, and thus has to be even more "stable". Here we can for example imagine a stream of equidistant photons. This yields the sub-Poissonian variance $(\Delta n)^2 = 0$ and thus a non-classical photon state, a so called photon-number state. The main difficulty in the experimental verification of such a sub-Poissonian state is photon loss, or with a similar effect imperfect detection efficiency. If we model the loss as a beamsplitter that randomly scatters photons out of the equidistant photon stream, the transmitted photons will have more and more random separations, the more losses the beamsplitter causes. This randomness leads in the limit of high losses to a Poissonian statistics.

1.2 Single photon source

Many of the experiments mentioned above were done using single photons. These can be created in many different ways. We refrain here from presenting a detailed description, which can be found in [MPFB13]. In general, single photon sources can be divided into two categories: probabilistic and deterministic sources. Probabilistic sources are based on photon-pair emission, where one of the photons is used to herald the other. Typically, the probability of photon-pair emission has to be kept low to avoid the emission of multiple pairs. This reduces the rate of photons available. Probabilistic sources are still the most widely used single photon sources [BFMP13]. Deterministic sources that deliver single photons on demand are often based on single emitters. Intense research is conducted to develop these sources.

We will briefly introduce the main figures of merit for the performance of single photon sources. Single photon sources are ideally emitting single-photon states. However, emission of multi-photon states remains possible, which can limit the usefulness of the device. Thus, *anti-bunching* is an important figure of merit for a single photon source. It can be quantified with correlation measurements [BT56]. For multi-photon experiments it is often important to interfere single photons from different sources e.g. to create entanglement (see section 1.3). To achieve good interference it is important that the photons are *indistinguishable* both spectrally and temporally. In practice, this is typically tested with a Hong Ou Mandel interference experiment [HOM87], combining two single photons on a beamsplitter. For many experiments and especially multi-photon experiments, the *generation rate and efficiency* are crucial parameters. These will not only determine the experiment duration but low efficiency can also limit the usefulness of the source for application schemes.

Many experiments require efficient storage and retrieval of light after a variable delay [NLK⁺13]. Quantum memories are devices with this capability for non-classical light states. They have been demonstrated using many different platforms e.g. rare-earth ion doped crystals [CUB⁺11] and warm atomic vapours [RML⁺11], using a variety of protocols. We refrain from presenting a complete list here, a broad overview including a discussion of the figures of merit can be found in [SAA⁺10].

1.3 Entanglement

In classical physics, a two-state system can be in either one of the two states. These two states can e.g. be horizontal or vertical polarization of a single photon. A different example would be the presence of a single photon or vacuum. We will label the two possible states $|0\rangle$ and $|1\rangle$. A quantum-mechanical two-

state system, also called a qubit, can be in the superposition state

$$|\psi\rangle = \alpha |0\rangle + \beta |1\rangle \tag{1.3}$$

A measurement of the state projects it on the measurement basis, e.g. $|0\rangle, |1\rangle$. The prefactors α and β will determine the probabilities of the measurement outcome. Even more interestingly, several systems can be entangled with each other. This means that their combined state cannot be written as a product of independent states. The state

$$|\phi^+\rangle = \frac{1}{\sqrt{2}}(|0\rangle_A |0\rangle_B + |1\rangle_A |1\rangle_B) \tag{1.4}$$

is an example of an entangled state between A and B. A measurement only on system A (or only on system B) will lead to a mixed state with equal probabilities for projection of system A (or B) on $|0\rangle$ or $|1\rangle$. However, if we measure one system, then we also project the state of the other system, thus its measurement outcome will be fixed, if we use the same basis. Since this entanglement is independent of the spatial separation of the systems, this "spooky action at the distance" was questioned sharply in the early days of quantum physics [EPR35]. Bell proposed a boundary that rules out local hidden variables as an alternative explanation [Bel64]. Based on this, and similar work [CHSH69], Aspect performed an experiment falsifying local hidden variable theories [ADR82]. Recent work with refined experiments is even considered loophole-free [HBD⁺15].

Entanglement can be useful for secure quantum communication. The fact that the measurement outcomes are uncorrelated, if the systems A and B in equation 1.4 are measured in carefully chosen bases¹, allows for quantum communication that can be immune against intercepting eaves-droppers [BB84]. The no-cloning theorem states that an arbitrary unknown quantum state, e.g. a state as in equation 1.3 with unknown α and β cannot be duplicated [WZ82]. It can however be teleported to a different location as we will see below.

1.4 Quantum teleportation and entanglement swapping

Quantum teleportation is the transfer of quantum information from one location to another, only using classical communication and previously shared entanglement between sending and receiving location [BBC⁺93].

As an example, let us consider that the qubit in equation 1.3 on system X should be teleported to system B, while systems A and B are already entangled. Two-

¹E.g. polarization state bases {horizontal, vertical} and {diagonal(+45°), diagonal(-45°)}

qubit entanglement can be expanded in the Bell state basis

$$|\phi^\pm\rangle = \frac{1}{\sqrt{2}}(|0_A\rangle|0_B\rangle \pm |1_A\rangle|1_B\rangle) \quad (1.5)$$

$$|\psi^\pm\rangle = \frac{1}{\sqrt{2}}(|0_A\rangle|1_B\rangle \pm |1_A\rangle|0_B\rangle). \quad (1.6)$$

Let us assume that the entangled state of A and B is prepared in $|\phi^-\rangle$. The initial state can then be described as

$$|\psi_{XAB}\rangle = \frac{\alpha}{\sqrt{2}}(|0_X0_A0_B\rangle - |0_X1_A1_B\rangle) + \frac{\beta}{\sqrt{2}}(|1_X0_A0_B\rangle - |1_X1_A1_B\rangle). \quad (1.7)$$

This can be rewritten in terms of Bell states of X and A as

$$\begin{aligned} |\psi_{XAB}\rangle = \frac{1}{2} [& |\phi_{XA}^+\rangle (\alpha|0_B\rangle - \beta|1_B\rangle) + |\phi_{XA}^-\rangle (\alpha|0_B\rangle + \beta|1_B\rangle) \\ & + |\psi_{XA}^+\rangle (-\alpha|0_B\rangle + \beta|1_B\rangle) + |\psi_{XA}^-\rangle (-\alpha|0_B\rangle - \beta|1_B\rangle)]. \quad (1.8) \end{aligned}$$

A joint measurement on X and A, determining their Bell state, then projects the qubit B into the corresponding state. Classical communication about the outcome of the Bell state measurement of X and A lets B know, which local operations B has to perform to correct the signs. After performing these local operations, the initial state of qubit X has been transferred to qubit B, while there is no entanglement left and the initial state of qubit X has been destroyed. With linear optics, it is not possible to distinguish all four Bell states [CL01], which limits the efficiency of successful teleportation to 50%.

Experimental observation of quantum teleportation was first reported with single photons [BPM⁺97]. Teleportation using photons is interesting for quantum information transfer over long distances. Reducing transmission losses by using free-space coupling to a satellite, the record distance for quantum teleportation (1400 km) has been recently achieved by [RXY⁺17].

One can extend the range of entanglement by means of entanglement swapping. This can be seen as follows. Let us assume that A and B share a Bell state, and X and Y share a Bell state. Performing a Bell state measurement on the qubits of X and A then destroys the initial entanglement, but creates entanglement between B and Y. Again, limited Bell state measurement efficiency with linear optics reduces the efficiency of entanglement swapping. The concepts presented in this section can be used for quantum communication as we will see in the following.

1.5 Quantum repeater and DLCZ-scheme

The natural choice for transmitting quantum information over long distances is to use single photons as flying qubits. Photons provide information transport

at the speed of light and they can travel long distances while only being weakly perturbed by the environment. However, if photons are sent through a fiber, the transmission losses actually matter and limit the communication distance. In classical communication, repeater stations are used to amplify the signal and counteract the losses. This does not work for qubits. Here a chain of quantum repeaters, as proposed by [BDCZ98] and [DLCZ01] can help to overcome the limiting exponential scaling with communication distance. The main idea of the so-called DLCZ-protocol, named after the authors of [DLCZ01], is to split the total communication distance in many short segments. Entanglement can be created probabilistically on each short segment. Subsequent entanglement swapping of neighbouring segments leads after repeating this process to entanglement between the sender and the receiver. The successfully entangled links are required to store their entanglement. The reason is that if entanglement creation or swapping on some segments fails, only those affected segments need to start over again. This procedure leads to a speed-up of the entanglement creation over long distances that results in a polynomial growth of the communication time with distance [DLCZ01].

After the publication of [DLCZ01] a lot of activity was directed towards experimental realization of the DLCZ-protocol with atomic ensembles. Already two years later [KBB⁺03] reported non-classical correlations between the heralding and the readout photons from an ensemble of cold caesium atoms with a violation of the Cauchy-Schwarz inequality by $R \approx 1.8 > 1$ and a write-read delay of about 400 ns. Non-classical correlations, although not at single-photon level were also observed by [vdWEA⁺03]. The performance of the experimental realizations was further improved during the next years. The longest memory times have been achieved in optical lattices [RDZ⁺10], reaching up to 0.22 s [YWBP16]. Cross-correlations have been shown up to $g_{W,R}^{(2)} \approx 600$ [LdRF⁺06], and retrieval efficiencies exceeding 80% have been reported [YWBP16], [BBV⁺14], [STTV07].

The performance of several quantum repeater protocols based on atomic ensembles and linear optics has been reviewed in [SSdRG11]. Experimentally, elementary nodes and links of the DLCZ-protocol have been realized with cold atomic ensembles [CLD⁺07], [YCZ⁺08], [CdRF⁺05], [LCD⁺07].

For completeness we mention briefly that there are also other quantum repeater schemes that are not based on atomic ensembles but e.g. on single ions [SDS09], single atoms in cavities [BKK⁺15] or Rydberg atoms [HHH⁺10]. The challenge for quantum repeaters is typically the need for quantum memories to be able to store the entanglement. However, protocols have been developed that work without the need for quantum memories [MSD⁺12], [MKL⁺14].

There has also been a lot of experimental progress with rare-earth ion-doped crystals as a platform instead of cold atoms. These solid state systems offer the possibility for spectral multiplexing [SSM⁺14]. Furthermore, record coherence

times of nuclear spins of several hours have been reported [ZHA⁺15]. Recently, DLCZ-type sources featuring temporal multimode storage have been achieved in rare-earth ion-doped crystals [KMdR17], with storage times on the order of 1 ms [LJE⁺17].

As we have seen above, cold atoms and rare-earth ion-doped crystals can serve as excellent atom-photon interface. However cold atoms require laser-cooling and solid-state systems require cryogenic temperatures to achieve their excellent properties. This technological complexity impedes the scalability of these platforms. This drawback makes room-temperature systems such as atomic vapour cells more interesting.

1.6 Vapour cells

Atomic vapour cells are used for a variety of sensitive sensing applications, e.g. for magnetic fields [BR07] [SLDR13], [JBT⁺16]. Glass cells with alkali atomic vapour, additionally filled with a noble gas as buffer gas are commonly used. The buffer gas ensures that the alkali atoms due to frequent collisions with buffer gas atoms take a long time until they collide with the cell walls. Collisions with the glass wall affect the atomic state, thus the use of buffer gas extends the atomic coherence time. Another technique to prolong the coherence time is the use of anti-relaxation coating of the cell walls. This removes the detrimental effect of the wall-collisions and allows for very long coherence times, which have been reported up to minutes [BKLB10]. The long coherence times have permitted many interesting experiments, such as demonstrating quantum memory for light [JSC⁺04], long-lived entanglement between macroscopic objects [JKP01] and teleportation between light and matter [SKO⁺06]. The disadvantage of anti-relaxation coated cells is that they are typically more difficult to fabricate, and only sustain a limited temperature range. Buffer gas cells and anti-relaxation coated cells lead to very different atomic motion. Buffer gas limits the atomic motion, which makes these cells suitable for short time-scale experiments.

Buffer gas cells have been used to demonstrate various different types of quantum memories. Electromagnetically introduced transparency (EIT) was reported on the single photon level [EAM⁺05], [HB10], [PGN08], [MSKT15]. Raman memory providing broadband storage was demonstrated [RML⁺11], recently even with cavity-enhancement [SMC⁺16]. A gradient index quantum memory was presented by [HCS⁺11] and recently [KLB⁺18] presented a noise-free ultra-fast quantum memory. The four-wave mixing process has been utilized to create correlated photon pairs [POS⁺17], [ZGS⁺17].

A different approach is the DLCZ-scheme in buffer gas cells. Here, heralded creation of excitations and subsequent readout after a delay time has been achieved with cross-correlations up to $g_{W,R}^{(2)} \approx 28$ [DYD⁺17]. Delay times on

the order of a few microseconds have been shown [BFV12]. Furthermore, spatial multimode application has been demonstrated [CW12].

1.7 This work

Typically, buffer gas experiments rely on having immobilized atoms during the experiment duration. This only allows for very short durations on the microsecond scale. The idea of the experiment presented in this thesis is to apply a DLCZ-scheme to a vapour cell with anti-relaxation coating. Letting the atoms cross the interaction beam many times effectively averages the interaction strength. This can be used to create symmetric collective excitations that are immune to atomic motion. The delay time between heralding and read-out is set by the coherence time of the created excitation, which typically exceeds the microsecond range by several orders of magnitude.

This allows for quantum information applications along the lines of the original DLCZ-proposal, where long storage times are beneficial for long-distance communication. Furthermore, it can be used as a source of narrowband on-demand single photons.

The thesis is structured as follows. We will start out with an explanation of the theoretical background in chapter 2. We will then describe the setup of the experiment in chapter 3. The subsequent chapter 4 discusses vapour cells and characterization measurements. The main results of the DLCZ-type experiment will be presented in chapter 5. Chapter 6 is dedicated to the proof-of principle experiment with improved noise performance. We will discuss the results, the limitations and possible improvements in chapter 7, and then conclude in chapter 8.

Part I

Theoretical background

Theory

2.1 The caesium atom

In our experiment we work with caesium-133 atoms. It is a stable alkali atom, that has one valence electron in the $6^2S_{1/2}$ ground state. The single valence electron leads to a comparably simple electronic level structure. For us the relevant transitions are the D_2 transition to the $6^2P_{3/2}$ level with a wavelength of about 852 nm and the D_1 transition to the $6^2P_{1/2}$ level with a wavelength of about 895 nm, as shown in fig. 2.1. The interaction of the total electron angular momentum J with the total nuclear angular momentum $I = 7/2$ splits the ground state into the hyperfine levels $F = 4$ and $F = 3$, where F is the total atomic angular momentum. Both levels are populated at room temperature since the ground state hyperfine splitting of $h\nu_{hfs} = h \cdot 9.2\text{GHz}$ is much smaller than the thermal energy at room temperature $k_B T (\approx h \cdot \text{THz})$. In the

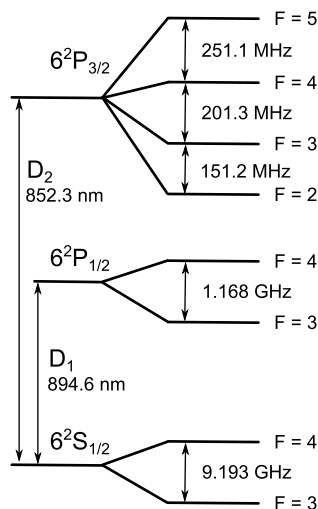


Figure 2.1: Hyperfine level structure for the D_1 line and D_2 line of caesium. Figure adapted from [Jul03]

presence of a weak static magnetic field B_x along the x -direction, the interaction of the total atomic angular momentum F with the magnetic field leads to the Zeeman effect, splitting each level F into $2F + 1$ magnetic sublevels labeled with the magnetic quantum number $m_F = F_x/\hbar$, that is the projection of F on the magnetic field direction. The energy shift of the atomic levels is given by [Ste15]

$$\Delta E_{|F, m_F\rangle} = \mu_B g_F m_F B_x \quad (2.1)$$

where μ_B is the Bohr magneton and g_F the hyperfine Landé factor. The frequency of neighbouring magnetic levels, that is levels with $\Delta m_F = \pm 1$, is thus shifted by the linear Zeeman frequency $\nu_Z = \mu_B g_F B_x / h$. When increasing the magnetic field, the quadratic Zeeman splitting is no longer negligible. Including the quadratic splitting, for two neighbouring levels this yields [JKP01]

$$\frac{E_{|F, m_F+1\rangle} - E_{|F, m_F\rangle}}{h} = \nu_Z - \frac{\nu_Z^2}{\nu_{hfs}} (2m_F + 1) \quad (2.2)$$

2.2 Light-atom interaction

We are interested in the interaction between light and a single atom. This has been studied in many textbooks e.g. [Ste15], we will recap the derivation here, following [HSP10]. We assume an atom at position \vec{r} with ground states denoted $|g_m\rangle$ and excited states $|e_m\rangle$, where we have used Dirac notation for the atomic states. We use the dipole approximation, where we can write the interaction Hamiltonian as

$$H_{int} = -\vec{d} \cdot \vec{E} \quad (2.3)$$

with the electric dipole operator for the atom \vec{d} and the electric field \vec{E} . We decompose the electric field in terms oscillating with positive and negative frequencies

$$\vec{E} = \vec{E}^{(+)} + \vec{E}^{(-)} = \vec{E}_0^{(+)} e^{-i\omega t} + \vec{E}_0^{(-)} e^{i\omega t} \quad (2.4)$$

and perform a similar decomposition with the dipole operator

$$\vec{d} = \vec{d}^{(+)} + \vec{d}^{(-)} = \sum_{m, m'} \vec{d}_{g_{m'} e_m} |g_{m'}\rangle \langle e_m| + \vec{d}_{e_m g_{m'}} |e_m\rangle \langle g_{m'}| \quad (2.5)$$

where we have defined the dipole matrix element $\vec{d}_{g_{m'} e_m} = \langle g_{m'} | \vec{d} | e_m \rangle$. The dipole matrix element determines the coupling strength between levels $|g_{m'}\rangle$ and $|e_m\rangle$. The dipole-allowed transitions, characterized by non-vanishing dipole matrix elements can then be combined into a convenient set of selection rules which can be found in any standard textbook, e.g. [Ste15]. We can perform the rotating wave approximation, thus neglecting the terms oscillating at twice the

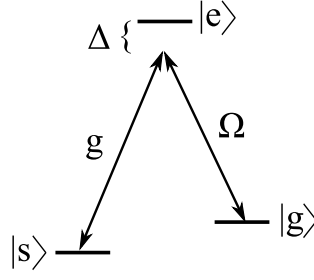


Figure 2.2: Schematic of three level system.

optical frequency. This yields

$$H_{int} = -(\vec{E}^{(-)} \cdot \vec{d}^{(+)} + \vec{d}^{(-)} \cdot \vec{E}^{(+)}) \quad (2.6)$$

For a simple two-level atom¹ with one ground state $|g\rangle$ and one excited state $|e\rangle$ we can write the interaction Hamiltonian

$$H_{int} = -\frac{\hbar}{2} \left(\Omega_{eg} |e\rangle \langle g| + \Omega_{eg}^* |g\rangle \langle e| \right) \quad (2.7)$$

where the Rabi frequency $\Omega_{eg} = 2\vec{d}_{ge}\vec{E}_0^{(+)} / \hbar$ determines the rate at which the atom gets transferred from $|g\rangle$ to the $|e\rangle$ and back. Choosing a suitable duration of the coupling allows to deterministically transfer the atom from one to the other state. [Ste15]

Our next example is a three level atom with two ground states $|g\rangle, |s\rangle$ and one excited state $|e\rangle$ as shown in fig. 2.2. We assume that the transition $|g\rangle \rightarrow |e\rangle$ is driven by an off-resonant light field with Rabi frequency Ω_{eg} , whereas the transition $|s\rangle \rightarrow |e\rangle$ is driven by a vacuum field with coupling g . Including the atomic Hamiltonian in the rotating frame $H_A = -\hbar\Delta |e\rangle \langle e|$ with $\Delta = \omega_L - \omega_e$ the detuning between light frequency and excited level, yields an atom-field Hamiltonian

$$H = -\hbar\Delta |e\rangle \langle e| - \hbar \left(\frac{\Omega_{eg}}{2} \sigma_{eg} + g\sigma_{es} + H.c. \right) \quad (2.8)$$

We have introduced the atomic operators $\sigma_{ij} = |i\rangle \langle j|$ here. The Hamiltonian can be simplified as follows using adiabatic elimination. We start from the Heisenberg equations of motion

$$\frac{d\sigma_{eg}}{dt} = \frac{i}{\hbar} [H, \sigma_{eg}] \approx 0 \quad ; \quad \frac{d\sigma_{es}}{dt} = \frac{i}{\hbar} [H, \sigma_{es}] \approx 0 \quad (2.9)$$

where the approximation is valid for weak drive and large detuning. Furthermore, in this case the excited state population will be negligible, that is

¹we do not include spontaneous emission here

$\sigma_{ee} \approx 0$. Inserting the resulting approximated atomic operators into the initial Hamiltonian gives an interaction Hamiltonian similar to eq. 2.7. However, now the coupling between the ground and excited states is given by an effective Raman-Rabi frequency $\Omega_{eff} = \frac{\Omega g^*}{2\Delta}$. Similar to the two-level model, coherent and deterministic transfer from one ground state to the other is possible [Ste15].

This is in contrast to the incoherent process of spontaneous emission. The rate of spontaneous emission from the excited state R_{sc} is given by multiplying the rate of spontaneous emission γ with the excited state population. As derived in [Ste15], this gives $R_{sc} \approx \gamma\Omega^2/(4\Delta^2)$, neglecting atomic coherences. We note the different scaling with detuning compared to the Raman-Rabi coupling. Since we are interested in a deterministic and coherent transfer of population, we require the Raman scattering to dominate over spontaneous emission. Due to the different scalings with Δ , this can be achieved by working at large detunings. We can achieve an increase in the light-atom coupling strength by using an atomic ensemble instead of just a single atom. This will be the topic in the next section.

Similar to the simple three level system, one can derive an effective ground state Hamiltonian for an atom with several ground and excited states, which gives according to [HSP10]

$$H'_{int} = \sum_{m,m'} V_{m',m}(\vec{r}) |g_{m'}\rangle \langle g_m| \quad (2.10)$$

where the coupling matrix $V_{m',m}$ can be expressed as

$$V_{m',m} = -\sum_{m''} \frac{\Omega_{m,m''} g_{m',m''}^*}{2\Delta_{m''}} \quad (2.11)$$

We note that [HSP10] sets $\hbar = 1$ and uses cgs units.

2.3 Light interaction with atomic ensembles

We now consider an ensemble of atoms with two ground states, $|g\rangle$ and $|s\rangle$, interacting with a weak quantum field while being driven by a strong classical field. The two ground states can be expressed in terms of angular momentum operators. We introduce the atomic collective annihilation operator

$$a_A = \frac{\sum_k \sigma_{gs}^{(k)}}{\sqrt{2\langle J_x \rangle}} \quad (2.12)$$

where J_x is the collective spin projection $J_x = \sum_k j_x^{(k)}$. We can easily see the effect of this operator by applying its conjugate to an ensemble of N atoms,

where all atoms are prepared in the ground state.

$$a_A^\dagger |g_1 \dots g_N\rangle = \frac{1}{\sqrt{N}} \sum_i |g_1 \dots s_i \dots g_N\rangle \quad (2.13)$$

It yields a symmetric superposition where each atom contributes equally to the single excitation. The resulting state is called a symmetric Dicke state or *W*-state [Dic54]. We will combine all other possible collective excitations under the name "asymmetric" collective excitations. We account for the position of each atom k , writing $\sigma_{gs}(\vec{r}) = \sum_k \sigma_{gs}^{(k)} \delta(\vec{r} - \vec{r}_k)$ and $j_x(\vec{r}) = \sum_k j_x^{(k)} \delta(\vec{r} - \vec{r}_k)$ and redefine the atomic annihilation operator

$$a_A(\vec{r}) = \frac{\sigma_{gs}(\vec{r})}{\sqrt{2\langle j_x(\vec{r}) \rangle}} \quad (2.14)$$

Assuming that classical and quantum field travel both in the z -direction, [HSP10] show that the Hamiltonian can be reduced to one dimension. Introducing a complete set of mode functions $\{u_m(\vec{r}_\perp; z)\}$ in the plane perpendicular to z we can expand the atomic annihilation operator in this basis

$$a_{A,m}(z) = \int d^2\vec{r}_\perp u_m(\vec{r}_\perp; z) a_A(\vec{r}) \quad (2.15)$$

We can furthermore introduce the annihilation operator for the quantum field $a_{L,m\sigma}(z)$ in mode m and polarization σ such that the electric field of frequency ω_0 is given by

$$\vec{E}(\vec{r}) = \sqrt{\frac{2\pi\omega_0}{c}} \sum_{m,\sigma} \vec{e}_\sigma u_m(\vec{r}_\perp; z) e^{i(k_0 z - \omega_0 t)} a_{L,m\sigma}(z) + \text{H.c.} \quad (2.16)$$

With all the above definitions and assuming all atoms in $|g\rangle$, the authors arrive at the so-called parametric gain Hamiltonian

$$H_G = \int dz \left[\frac{|\Omega(z, t)|^2}{4\Delta} \sum_m a_{A,m}^\dagger(z) a_{A,m}(z) - \left(\frac{g^*(z)\Omega(z, t)}{2\Delta} \sum_m e^{i\Delta k z} a_{L,m}^\dagger(z) a_{A,m}^\dagger(z) + \text{H.c.} \right) \right] \quad (2.17)$$

with the atomic density $n(z)$ and the coupling constant

$$g(z) = \vec{d}_{e,s} \vec{e}_q \sqrt{2\pi\omega n(z)/c} \quad (2.18)$$

with the quantum field polarized along the unity vector \vec{e}_q and the light frequency ω . We have included the frequency difference between the driven and the quantum mode in the wavenumber difference Δk in the phase factor. The

first term in the Hamiltonian is the ac-Stark shift of the atomic ground state. The second term contains the parametric gain part, creating collective atomic excitations while simultaneously creating photons.

A parametric gain Hamiltonian $H = \zeta a_L^\dagger a_A^\dagger + \text{H.c.}$ with light-atom coupling ζ leads to a two-mode squeezed state [GK05]², which can be expressed in number states as

$$|\zeta\rangle_2 = \frac{1}{\cosh \zeta} \sum_{n=0}^{\infty} (-\tanh \zeta)^n |n, n\rangle_{A,L} \quad (2.19)$$

where $\zeta = -i\tilde{\zeta}t/\hbar$. From this we can draw several conclusions. First, this is an entangled state between light and atoms. The fact that the number of photons is deterministically connected with the number of atomic excitations, allows heralding of the atomic state conditioned on the detection of scattered photons. This characteristic is fundamental for the employment of this scheme as a single photon source. Experimentally, limited detection efficiency and excess noise counts pollute the two-mode squeezed state and hinder the unambiguous heralding of atomic excitations. The effect of noise on the conditioned state has been described in [CBB⁺14]. Second, we see that an excitation probability of p for the single excitation $|1, 1\rangle_{A,L}$, results in a excitation probability p^2 for the double excitation $|2, 2\rangle_{A,L}$ etc. for higher excitations. For unit detection efficiency and number-resolving detection we could tell the states apart. In practice, we need to keep the scattering probability low to avoid multiple excitations. Third, if we only consider either the light mode or the atomic mode, it can be shown [GK05] that the resulting state follows a thermal distribution.

We note that the coupling g in the parametric gain term contains the atomic density. This confirms the increase of the desired Raman-Rabi coupling with the number of atoms, compared to the spontaneous emission rate, as mentioned in the previous section.

Atoms at different z-positions contribute to the scattered field with different phases according to the phase factor $e^{i\Delta kz}$. This can be seen as imprinting a spinwave with wavenumber Δk onto the atomic ensemble. We have chosen here a collinear configuration of drive and quantum field. In a non-collinear configuration the imprinted phase would be $e^{i\Delta\vec{k}\cdot\vec{r}}$. Already a small angle leads to considerable size of $\Delta\vec{k}$ since the contributing \vec{k} -vectors belong to optical frequencies (e.g. $\alpha = 0.16^\circ \rightarrow |\Delta\vec{k}| \approx 2\pi/300 \mu\text{m}^{-1}$). Movement of the atoms on the order of $\approx 1/|\Delta\vec{k}|$ washes out the imprinted phase. Since the phase is crucial for efficient readout of the spinwave, atomic motion is a main limitation for long-time storage of spinwaves. This is why, even though a small angle between driving and quantum field facilitates the separation of the two fields, we will focus on the co-propagating design in our experiment. For warm atomic vapour, co-propagating geometries furthermore eliminate differential Doppler

²See also [Chr14], appendix

shifts. We note, that in the co-propagating case there is still a wavenumber difference along the z -direction. The wavelength of the corresponding spinwave can limit the allowed length of the atomic ensemble along z . For the hyperfine transition this has been shown in [BZP⁺16] to be relevant if the length of the atomic ensemble is more than about $1/3$ of the spinwave wavelength. In our experiment we will work with spinwaves that have three orders of magnitude larger wavelength, thus this effect will be negligible.

2.4 Readout

Let us assume that we have stored collective excitations during the write process according to the previous section. Now for the readout we swap the classical drive and the quantum field. [HSP10] derive the Hamiltonian for this case, yielding

$$H_{BS} = \int dz \left[\frac{-|\Omega(z, t)|^2}{4\Delta} \sum_m a_{A,m}^\dagger(z) a_{A,m}(z) - \frac{|g(z)|^2}{4\Delta} \sum_m a_{L,m}^\dagger(z) a_{L,m}(z) - \left(\frac{g^*(z)\Omega(z, t)}{2\Delta} \sum_m e^{i\Delta k' z} a_{L,m}^\dagger(z) a_{A,m}(z) + \text{H.c.} \right) \right] \quad (2.20)$$

The structure of this Hamiltonian is very similar to the write case.³ The first term is again the ac-Stark shift of the atomic ground state, the second is the index of refraction of the atomic ensemble. The last line describes a beamsplitter interaction, where an atomic excitation is annihilated while a photon is created and vice versa. We have written the wavenumber difference in the readout Hamiltonian as $\Delta k'$, indicating that it may be different from the write process.

Similar to the write process there is an enhancement of the coupling by $\sqrt{N_A}$ from using an ensemble of N_A atoms. During the read process there is also collective interference, that ensures the directionality of the readout. It is based on the phase factor that appears in the beam splitter part. We can write the successful read state according to [SSdRG11], [Pet09] as

$$|\psi_{read}\rangle = \frac{1}{\sqrt{N_A}} \sum_{j=1}^{N_A} c_j c'_j e^{i(\vec{k}_w - \vec{k}_h)\vec{r}_j} e^{i(\vec{k}_r - \vec{k}_{sp})\vec{r}_j} |g_1 \dots g_{N_A}\rangle \quad (2.21)$$

where we have used the indices w, h for classical and quantum fields in the write process, and r, sp respectively in the readout. The parameters c_j and c'_j signify here the contribution of the individual atoms to the collective excitation. In order to maximize the readout in a specific direction, the terms of the sum should add constructively, that means the phase factors should yield unity. This

³For the beamsplitter Hamiltonian the definition $a_{A,m}(z) = \int d^2\vec{r}_\perp u_m^*(\vec{r}_\perp; z) a_A(\vec{r})$ is chosen by [HSP10]

can be achieved with the trivial solution

$$\vec{k}_w = \vec{k}_h \quad \text{and} \quad \vec{k}_r = \vec{k}_{sp} \quad (2.22)$$

which implies degenerate atomic ground states. This solution is not suitable for us since we require a frequency separation between the classical and quantum fields in order to filter the quantum photons from the classical photons before detection. For stationary atoms, the different terms in the sum will interfere constructively if the phase-matching condition

$$\vec{k}_w - \vec{k}_h = -(\vec{k}_r - \vec{k}_{sp}) \quad (2.23)$$

is fulfilled. From this follows, that the direction in which the desired photon (sp) is scattered, is given by the write and read beams as well as the scattered heralding photon (h). We will work with co-propagating geometry, where we detect the forward-scattered heralding photon. Thus the desired scattered photon in the read process will be also forward-scattered. As discussed in the previous section, when the atoms move significantly compared to the wavelength of the stored spinwave, it washes out the phase of the spinwave and thus ruins the collective interference necessary for efficient directional readout.

In the considered model the collective excitation can either be coherently read out or incoherently scattered due to spontaneous emission. From the derivation of [HSP10] it follows, that the coherent readout will dominate for large optical depth of the ensemble. This enables an efficient interface between atoms and light.

2.5 Motional averaging

We have seen in the previous sections that atomic motion can be detrimental to the deterministic readout of stored collective excitations. We have however also seen, that atomic motion on a length scale significantly shorter than the wavelength of the spinwave does not affect the readout of a collective excitation stored in the symmetric mode. The concept of motional averaging developed in [BZP⁺16] allows us to address the symmetric mode, enabling efficient readout of a collective excitation stored in an atomic ensemble at room temperature.

This section describes the main results that have been already presented in [BZP⁺16], with the addition of using several excited states. The derivations and steps in the calculation can be found in more detail in Appendix A.

We will in the following derivation consider an atomic ensemble with two ground states $|g\rangle$ and $|s\rangle$ at room temperature inside a low finesse cavity. This so-called "cell cavity" is in the derivation assumed to be one-sided, that means all the light is coupled through one of the mirrors. The outcoupled field is sent through a filter cavity. The setup is sketched in fig. 2.3

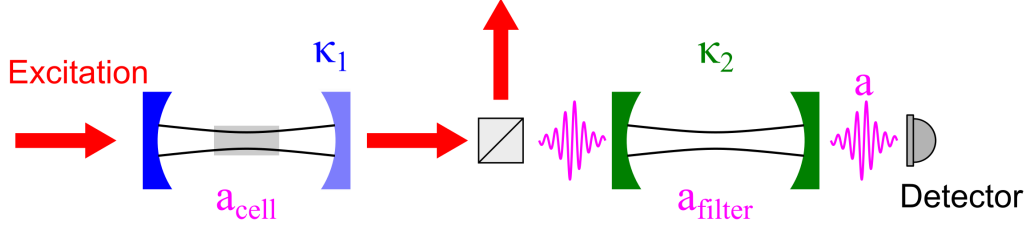


Figure 2.3: Schematic of the setup. A classical field (red) excites the atoms in the cell cavity (blue). The quantum field (purple) is filtered out and passes through a filter cavity (green) before hitting the detector.

For the write process we consider all atoms initially in $|g\rangle$. A classical field couples this level to the excited states, while the undriven quantum field couples $|s\rangle$ to the excited states. We start with a Hamiltonian similar to [BZP⁺16] adding the relevant levels

$$\hat{H} = \sum_{j=1}^N \sum_m -\Delta_m \hat{\sigma}_{e_m e_m}^{(j)} - \left(\frac{\Omega_j^{(m)}(t)}{2} \hat{\sigma}_{e_m 0}^{(j)} + g_j^{(m)}(t) \hat{a}_{cell} \hat{\sigma}_{e_m 1}^{(j)} + H.c. \right) \quad (2.24)$$

where we sum over N atoms and include each excited level $|e_m\rangle$ as well as its respective detuning Δ_m to the light. (In our current D₂ scheme $m \in \{1, 2, 3\}$). The quantum field inside the cell cavity is described by \hat{a}_{cell} . For small perturbations we can derive an expression for the field after the filter cavity (Appendix A) given by

$$\hat{a} = -\frac{\kappa_2 \sqrt{\kappa_1}}{4} \sum_{j=1}^N \theta_j(t) \hat{\sigma}_{10}^{(j)} \quad (2.25)$$

where κ_1 is the decay rate of the cell cavity and κ_2 is the decay rate of the filter cavity. The coefficient $\theta_j(t)$ describes the time-dependent coupling between light and atoms and is defined as

$$\theta_j(t) = \int_0^t dt' \int_0^{t'} dt'' \int_0^{t''} dt''' e^{-\frac{\kappa_2}{2}(t-t')} e^{-\frac{\kappa_1}{2}(t'-t'')} \sum_m e^{-(\frac{\gamma}{2} - i\Delta_m)(t''-t''')} g_j^{(m)}(t'') \Omega_j^{(m)}(t''') \quad (2.26)$$

Here the integral over t''' stems from the equations of motion, the integral over t'' comes from the cell cavity build-up and the integral over t' comes from the filter cavity build-up. In [BZP⁺16] they assume a Gaussian transverse beam profile with a fixed waist radius w along the cell cavity. This yields for the couplings

$$\Omega_j^{(m)}(t'') = \Omega_m e^{\frac{-x_j^2(t'') - y_j^2(t'')}{w^2}} \sin(k_c z_j(t'')) \quad (2.27)$$

$$g_j^{(m)}(t'') = g_m e^{\frac{-x_j^2(t'') - y_j^2(t'')}{w^2}} \sin(k_q z_j(t'')) \quad (2.28)$$

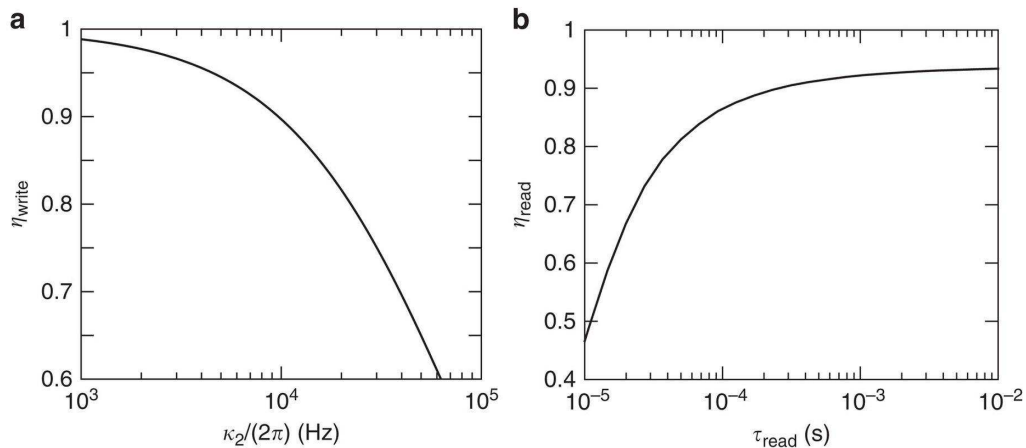


Figure 2.4: **a** write efficiency versus filter decay rate obtained from simulation. **b** optimal readout efficiency as a function of the readout duration τ_{read} obtained from simulation. Here $\tau_{read} = 3/\Gamma_{read}$, where Γ_{read} is the readout rate. According to [BZP⁺16] the finesse of the filter cavity was varied between 20 and 100 to get the optimal readout efficiency. The underlying assumption for the simulation was collective excitation into $|3,3\rangle$. Cell and beam dimensions, detuning and write pulse length correspond to our typical experimental conditions. Figure adapted from [BZP⁺16].

where the z -components are given by the standing wave in the cavity. The write efficiency is defined as the probability of having stored a single collective excitation in a symmetric Dicke state upon detection of a heralding photon. As [Pet09] derived, the write efficiency over the write duration t_{int} can be calculated from $|\langle\theta_j(t)\rangle_e|^2$ and $\langle|\theta_j(t)|^2\rangle_e$ as shown below. The latter includes correlations between positions of individual atoms. [BZP⁺16] performed a Monte Carlo simulation with atoms in a rectangular cell, experiencing collisions with the cell walls that redistribute the velocity and randomize the direction of motion. Using dimensions similar to our experimental setup, this yielded an exponential decay time of the correlations of $\Gamma \approx 1.3v_{thermal}/w \approx 2\pi \cdot 0.75$ MHz. Thus the write efficiency can be written as

$$\eta_{write} \approx \frac{\int_0^{t_{int}} |\langle\theta_j(t)\rangle_e|^2 dt}{\int_0^{t_{int}} \langle|\theta_j(t)|^2\rangle_e dt} \approx \frac{1}{1 + \frac{\kappa_2}{2\Gamma + \kappa_2} \left(\frac{4L^2}{\pi w^2} - 1\right)} \quad (2.29)$$

where $2L$ is the length of the transverse profile of the cell. In the second approximation we have assumed $L > w$, $\kappa_1 \gg (\Gamma, \kappa_2)$, and a detuning beyond the Doppler width of the atomic transition. From this equation we can draw two conclusions. A better filling of the cell cross section by the beam, reducing the factor $\frac{4L^2}{\pi w^2}$, increases the write efficiency. Furthermore, a good write efficiency requires a slow decay of the filter cavity with respect to the decay time of the correlations, such that the factor $\frac{\kappa_2}{2\Gamma + \kappa_2}$ decreases. This is visualized in fig 2.4 a. It shows the write efficiency obtained by [BZP⁺16] via simulation. We note

that a comparison with the analytical equation 2.29 confirms good agreement for small κ_2 . For higher κ_2 the analytical expression overestimates the write efficiency, e.g. for the experimental value of $\kappa_2/(2\pi) \approx 66$ kHz we calculate $\eta_{write} \approx 73\%$.

We can intuitively understand the dependencies in eq. 2.29 as follows. Upon conditioning, we want to project the atomic state on the symmetric Dicke state. This requires all atoms to contribute equally to the collective excitation. Since we have a transverse beam profile across the cell cross section, the light-atom interaction depends on the transverse atomic position. Without the filter cavity, the detection of the heralding photon at a specific time gives every atom an individual coupling strength to the collective excitation. The resulting state has only little overlap with the symmetric Dicke state. If we however wash out the timing information of the heralding photon by adding a random delay to the heralding photon, where the delay is longer than the transverse atomic position correlations, we ensure that every atom contributes equally to the collective excitation. Thus we create a symmetric Dicke state by averaging over the atomic positions, which is known as "motional averaging". The write efficiency can be increased by increasing the beam size, thus faster motional averaging. Alternatively the slower the filter cavity decay time, the better the averaging of the position correlations.

Number of classical photons In the supplementary information of [BZP⁺16] there is a derivation to estimate the number of classical photons that need to be filtered out per scattered heralding photon. In appendix A, the derivation is extended for several excited states. Similar to the original derivation we relate the required number of classical photons to d , the hypothetical on-resonant optical depth in the absence of Doppler broadening. This definition has already been used previously, e.g. [GALS07b]. The resulting equation is (see eq. A.40)

$$N_{clas} = \frac{64N\pi^2}{\gamma^2 d^2 F^2} \frac{\beta_2'^2}{\beta'} \frac{1}{\left| \sum_m \frac{g^{(m)} \Omega^{(m)}}{g^{(i)} \Omega^{(i)}} \frac{1}{\Delta_m} \right|^2} \quad (2.30)$$

where F is the cell cavity finesse, γ is the excited state lifetime and β' and β_2' include Clebsch-Gordan factors as defined in the appendix. The equation depends both on the number of atoms N and the optical depth d . These can be determined experimentally via a Faraday angle measurement or an absorption spectroscopy measurement. The measurement of the Faraday angle and its relation to the number of atoms is briefly explained in section 2.7, further details on Faraday angle and absorption spectroscopy measurements can be found in e.g. [Jen11], [Jul03]. The relation between Faraday angle and optical depth can be found in [BZP⁺16] and in the appendix A. For a typical set of experimental

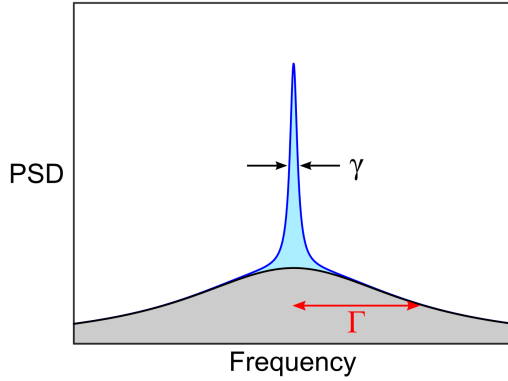


Figure 2.5: Example of expected write spectrum. Narrow peak from symmetric collective excitation with FWHM γ . Broad contribution from asymmetric collective excitations with half width corresponding to the correlation decay time Γ .

parameters, that is an optical depth⁴ of 412 and a Finesse of $F = 18$, we estimate a number of classical photons that is required to be filtered out per scattered photon of $N_{class} = 1.2 \cdot 10^8$. These classical photons are very close in frequency (typical Zeeman splitting 2.4 MHz). Thus we require a dedicated filter setup to separate quantum and classical fields.

Write spectrum The spectrum of the scattered light field a' before the filter cavity can be calculated by Fourier transformation of $a'^{\dagger}(t)a'(t)$ using equation 2.25. This is done in [BZP⁺16] where it is separated into a contribution from the averaged couplings and a contribution including the position correlations. These have very different spectral widths. The rate of the exponential correlation decay Γ gives the width (HWHM) of the latter contribution. For our parameters we expect a broad Lorentzian of about $\Gamma = 2\pi \cdot 0.75$ MHz. The averaged contribution is according to the derivation in [BZP⁺16] Fourier limited by the write pulse duration. If the excitation light itself is not Fourier limited but is spectrally broader, we expect that the spectrum of the Raman-scattered light will follow the spectral width of the excitation light. An expected sample spectrum is shown in fig. 2.5

Readout The authors consider a single excitation stored in the symmetric mode in the ensemble and a classical drive Ω to read out the excitation and transform it into a cavity photon. The Hamiltonian for this interaction is similar to 2.24, with ground and storage state exchanged. The authors separate the interaction into average time-independent couplings and time-dependent fluctuations. Treating these fluctuations as small perturbations they find that the cavity field can be expressed as $a_{cell} \approx a_{cell}^{(0)} + a_{cell}^{(2)}$. The field from the cell cavity is sent to the filter cavity to remove the excitation light. The authors derive the

⁴Here we have extrapolated a Faraday angle measurement 1.5° at $\Delta = 1.6$ GHz and room temperature to the detuning $\Delta = 925$ MHz and the operating temperature of around 42°C

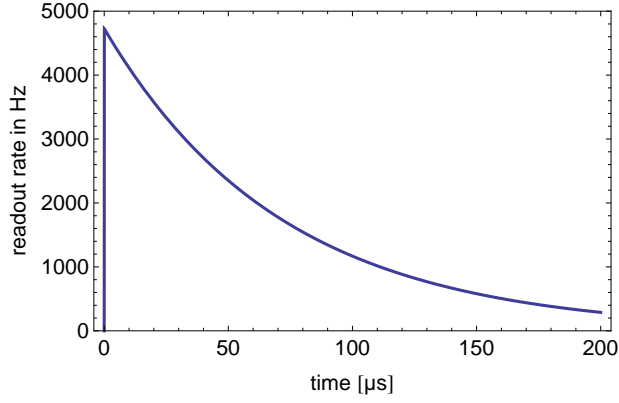


Figure 2.6: Read count rate versus readout time calculated for lowest order of perturbation using the caesium levels $|4,4\rangle \leftrightarrow |3,3\rangle$

readout efficiency

$$\eta_{read} = \frac{\kappa_2^2 \kappa_1}{4} \int_0^{\tau_{read}} dt \int_0^t dt' \int_0^{t'} dt'' e^{-\kappa_2/2(2t-t'-t'')} \langle a_{cell}^\dagger(t') a_{cell}(t'') \rangle \quad (2.31)$$

where τ_{read} is the duration of the readout pulse. To lowest order in perturbation this yields

$$\eta_{read,0} \approx \frac{1}{\frac{\pi}{dF} + 1} \quad (2.32)$$

in the limit of a very weak and very long readout pulse.

The term dF/π is the optical depth multiplied with the number of passes in the cell cavity. The read efficiency increases when this effective optical depth increases. We note, that the result is equivalent to the result $\eta_r = C/(1+C)$ for cold atoms given by [GALS07a] with the cooperativity parameter $C = g^2 N / (\kappa \gamma)$.

In [BZP⁺16] an expression for the field in lowest perturbation order is derived. We do not rewrite this lengthy expression here. However, we show the resulting expected read count rate versus time for typical parameters in fig. 2.6 where we observe that the read count rate decays exponentially. We note that the rate and the decay of the rate may easily be confused. We try to consistently name the rate at which photons are created during the read process "read count rate", while the decay of the created photon rate happens with the "readout rate" Γ_{read} . The scaling of these rates with different parameters is not straightforward. However, as intuitively expected, higher read excitation light power leads to faster readout.

In practice the excitation should be read out within a short time to avoid decoherence of the stored excitation. This requires to take into account higher order perturbations which reduces the read efficiency. The read efficiency to second order is given by a lengthy expression that we refrain from writing here. It can

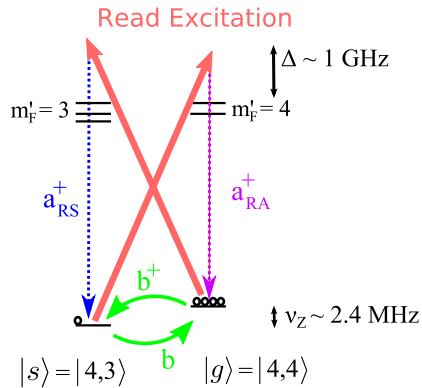


Figure 2.7: Level scheme for four-wave mixing

be found in the supplement of [BZP⁺16]. The resulting read efficiency is shown in fig. 2.4. Here the horizontal axis is the readout duration $\tau_{read} = 3/\Gamma_{read}$.

2.6 Four-wave mixing

The theoretical explanations in [BZP⁺16] cover most of what is needed for the single collective excitation experiment in this thesis. This is not a lucky coincidence but it was planned. However, the theoretical explanation was initially developed to fit the storage of collective excitations on hyperfine states. For experimental reasons explained in 4.6, we changed the experiment to operate on Zeeman levels instead. Apart from causing small changes in the coupling strengths, it also has the following big impact. The classical excitation was for hyperfine states always very far-detuned (> 9 GHz) from one of the ground states. Thus we could model the atom as a lambda system. For Zeeman states, the classical excitation couples to both ground states since the detuning differs only by the Larmor frequency. This means that e.g. the read excitation light acts simultaneously as the desired read field and as a write field. This so-called four-wave mixing process has been studied in detail previously. While for many experiments four-wave mixing has been an intrinsic noise process [MCS⁺15], other experiments have actually used it as a benefit as e.g. for the creation of correlated photons [POS⁺17].

For a slightly different system, a vapour cell without any cavity, [DCW14] have investigated the four-wave mixing process. They do not use motional averaging but instead buffer gas to keep the atoms from moving and washing out the stored spinwave phase. Similar to their derivation we consider a four-level system as shown in fig. 2.7. For the atomic collective excitation we use collective creation (b^\dagger) and annihilation (b) operators. The transitions from the ground states $|g\rangle$ and $|s\rangle$ are driven by a classical field \mathcal{E} . The scattered photons in the quantum fields are labelled⁵ a_{RA}^\dagger and a_{RS}^\dagger . The Hamiltonian describing this

⁵We use the same names for the quantum fields as [DCW14], even though the original

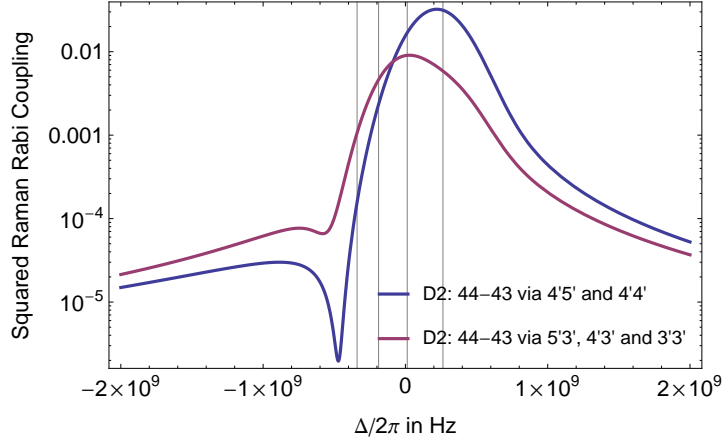


Figure 2.8: Squared Raman Rabi Coupling $|\sum_m g_m \Omega_m w[\frac{\Delta_m + i\gamma/2}{\Gamma_D}] / \Gamma_D|^2$ for the transition $|4,3\rangle \leftrightarrow |4,4\rangle$ via the D2 line versus light detuning. Zero detuning corresponds to the D2 line without hyperfine splitting. The black vertical lines show the caesium hyperfine resonances of $|F' = 2\rangle$ to $|F' = 5\rangle$ from left to right. For the readout we have χ^2 in blue and ξ^2 in red.

system is then given by

$$H_R = i\hbar\chi a_{RA}^\dagger b + i\hbar\xi a_{RS}^\dagger b^\dagger + H.c. \quad (2.33)$$

with the coupling coefficients χ and ξ . The part of the Hamiltonian coupled via χ is a beamsplitter Hamiltonian, creating a photon upon annihilation of an atomic collective excitation. The ξ part is a parametric gain Hamiltonian, creating simultaneously photon and atomic collective excitation. The total Hamiltonian including both parts is called a "Faraday interaction" Hamiltonian [HSP10], which is also the basis for the MORS experiment in section 4.5.

Comparing this Hamiltonian with the relevant equations 2.25 and A.21 of the previous motional averaging case, we infer that the couplings χ and ξ are proportional to $\sum_m g_m \Omega_m w[\frac{\Delta_m + i\gamma/2}{\Gamma_D}] / \Gamma_D$ with the respective excited levels labelled m . The square of this sum is shown in fig. 2.8. We see that far detuned ($\approx 1 \text{ GHz} \gg \Gamma_D \approx 225 \text{ MHz}$) from the resonances, the ratio of the coupling strengths is on the order ≤ 2 . This means that both, beamsplitter and parametric gain interaction will have significant contribution to the dynamics of the interaction.

[DCW14] have calculated an expression for the mean number of scattered quantum photons as a function of time. With the assumption that the incoming quantum fields are in a vacuum state and the mean number of initial spinwave

"Stokes" and "Anti-Stokes" labelling is not correct here since our initial state is at higher energy.

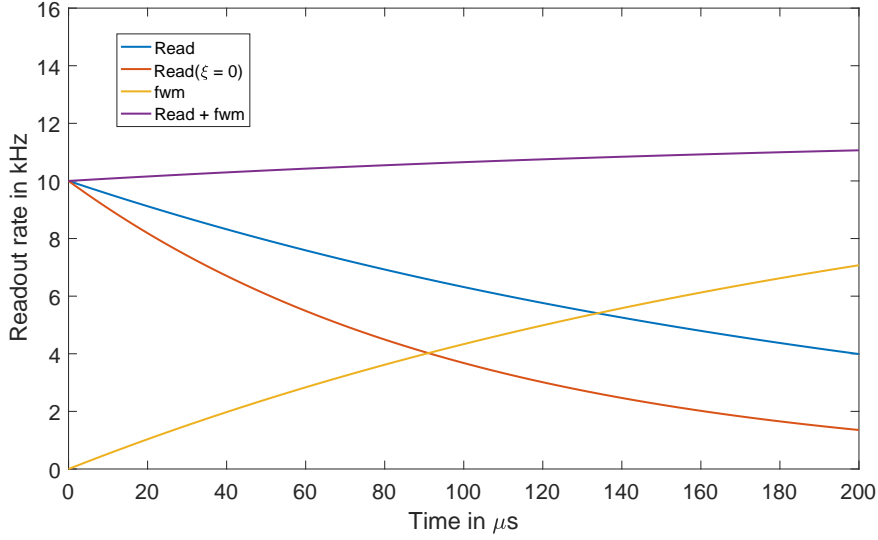


Figure 2.9: Readout rate versus readout time according to eq. 2.34 for an example value of $\chi = 100 \sqrt{\text{Hz}}$. We have chosen $\zeta = \chi/1.36$ for the readout of the collective excitation (blue), the four-wave mixing noise (yellow) and their sum (purple). In red we show the readout for vanishing ζ .

excitations is $n_b = \langle b^\dagger(0)b(0) \rangle$ they find

$$\langle a_{RA}^\dagger(t)a_{RA}(t) \rangle = \chi^2 e^{t(\zeta^2 - \chi^2)} n_b + \frac{\chi^2 \zeta^2}{\zeta^2 - \chi^2} (e^{t(\zeta^2 - \chi^2)} - 1) \quad (2.34)$$

$$\langle a_{RS}^\dagger(t)a_{RS}(t) \rangle = \zeta^2 e^{t(\zeta^2 - \chi^2)} n_b + \frac{\zeta^2}{\zeta^2 - \chi^2} (\zeta^2 e^{t(\zeta^2 - \chi^2)} - \chi^2) \quad (2.35)$$

During the readout process the desired (single) photon is on the transition labelled RA . In the absence of four-wave mixing, i.e. $\zeta \rightarrow 0$, the second term in the corresponding line vanishes and we have an exponentially decaying readout of the stored collective excitation as in the previous section. If four-wave mixing is significant and $\chi^2 > \zeta^2$, the exponential decay of the readout is slowed down. Since the initial amplitude of the exponential is still χ^2 , this means that the total number of photons scattered during the readout time window can actually be larger than the number of stored spinwaves. This can be understood as four-wave mixing that is enhanced by the initial presence of spinwaves. On top of this, the second term adds a contribution that increases over time and that is independent of the number of stored spinwaves. An example of this situation is shown in fig. 2.9.

2.7 Input-output relations

We will later require measurements to characterize the properties of the vapour cells (see section 4. We will therefore briefly introduce the formalism that has

been traditionally used in these experiments. We consider an ensemble of N caesium atoms distributed among the Zeeman levels m_F of a single hyperfine manifold F , with the quantization axis defined by a bias magnetic field along the x -axis. We can then express the total macroscopic angular momentum J by [JSSP04]

$$J_y = \frac{1}{2}[J_+ + J_-] = N \sum_{m=-F}^{F-1} \frac{C(F, m)}{2} (\rho_{m+1, m} + \rho_{m, m+1}) \quad (2.36)$$

$$J_z = \frac{1}{2i}[J_+ - J_-] = N \sum_{m=-F}^{F-1} \frac{C(F, m)}{2i} (\rho_{m+1, m} - \rho_{m, m+1}) \quad (2.37)$$

$$J_x = N \sum_{m=-F}^F m \rho_{mm} \quad (2.38)$$

where $C(F, m) = \sqrt{F(F+1) - m(m+1)}$ and $\rho_{i,j} = \frac{1}{N} \sum_{k=1}^N |i\rangle_k \langle j|_k$ for $i, j \in -F, -F+1, \dots, F$ is the density operator. We have written $J_{\pm} = J_y \pm iJ_z$ for the angular momentum ladder operators.

The evolution of the macroscopic spin J with a large longitudinal component J_x along the bias field and the transverse components J_y and J_z can be described by two time constants, T_1 and T_2 . The longitudinal component decays⁶ as $J_x(t) = J_x(0)e^{-t/T_1}$. The transverse components decay exponentially with T_2 .

We define the atomic polarization similar to [Jul03] as

$$p = \frac{1}{F} \sum_{m=-F}^F m \rho_{m,m} \quad (2.39)$$

With this definition $p = 1$ corresponds to all atoms being in the extreme $m = F$ level.

In contrast to the previous sections, where we focused on counting photons scattered into a specific mode, here we will use balanced polarimetry to analyse the light. This allows us to measure the Stokes components of the light. For light propagating in the z -direction, these are defined as [Jul03]

$$S_x = \frac{1}{2}(n_{ph}(x) - n_{ph}(y)) \quad (2.40)$$

$$S_y = \frac{1}{2}(n_{ph}(+45^\circ) - n_{ph}(-45^\circ)) \quad (2.41)$$

$$S_z = \frac{1}{2}(n_{ph}(\sigma_+) - n_{ph}(\sigma_-)) \quad (2.42)$$

where $n_{ph}(x)$ is the number of photons with x polarization.

⁶We note that this exponential decay is a simplification of the expected double exponential decay with fast and slow decay constants, see [GKR⁺05].

Starting from the dipole interaction Hamiltonian one can derive input-output relations for the atomic and light operators. The details can be found in [Jul03]. Here we will only state the relation that will be used in the Magneto-Optical Resonance Spectroscopy (MORS) measurement

$$S_y^{out} = S_y^{in} + a^{(F)} S_x J_z \quad (2.43)$$

where S_x is approximately constant⁷ and S_y^{in} can be assumed zero. The superscripts *in* and *out* refer to the state before and after the interaction. The interaction parameter $a^{(F)} = -a_1 \gamma \lambda^2 / (8\pi A \Delta_F)$ depends on the FWHM γ of the excited state, the wavelength λ and the beam cross section A . Δ_F is the laser detuning from the excited state $F'=5'$ when addressing the $F=4$ manifold, and from $F'=2'$ when addressing the $F=3$ manifold. The parameter a_1 is given by [Jul03]

$$a_1 = \frac{1}{120} \left(-\frac{35}{1 - \Delta_{35}/\Delta_F} - \frac{21}{1 - \Delta_{45}/\Delta_F} + 176 \right) \quad \text{for } F = 4 \quad (2.44)$$

$$a_1 = \frac{1}{56} \left(\frac{45}{1 + \Delta_{24}/\Delta_F} - \frac{21}{1 + \Delta_{23}/\Delta_F} - 80 \right) \quad \text{for } F = 3 \quad (2.45)$$

where Δ_{ij} describes the splitting between the excited manifolds i and j . The laser detunings used here are meant to have positive sign for red detuning of the laser.

From equation 2.43 we see that the light after the interaction carries information about J_z . We can thus characterize the transverse atomic spin component and its decay by analysing the light at the output. We will make use of this when characterizing vapour cells.

For an atomic ensemble with macroscopic spin component J_z , and a linearly polarized laser beam propagating along z we can observe Faraday rotation. The output beam will be linearly polarized with an angle θ_F between planes of polarization of input and output. This Faraday angle is given by [Jen11]

$$\theta_F = -\frac{a_1 \gamma \lambda^2 \rho L}{8\pi \Delta} \cdot \langle J_z \rangle \quad (2.46)$$

where ρ is the atomic density and L the length of the ensemble. $\langle J_z \rangle$ is the expectation value of the macroscopic spin component J_z . This relation can be used for characterization of the longitudinal spin component and its decay.

⁷ S_x is the difference in number of photons polarized along x and along y . Using light linearly polarized along x makes this approximately constant.

2.8 Nonclassical correlations

We have in the previous sections investigated the use of an atomic ensemble as a single photon source. We will now focus on the next step, the analysis of the output.

We use the normalized second-order auto-correlation function

$$g_{RR}^{(2)} = \frac{\langle I_R^2 \rangle}{\langle I_R \rangle^2} = \frac{\langle a_R^\dagger a_R^\dagger a_R a_R \rangle}{\langle a_R^\dagger a_R \rangle^2} = \frac{\langle a_R^\dagger a_R (a_R^\dagger a_R - 1) \rangle}{\langle a_R^\dagger a_R \rangle^2} \quad (2.47)$$

where we have used the commutation relation for creation and annihilation operators for the last equality. The photon number operator $a^\dagger a$ yields for a single photon state by definition one. This antibunching manifests itself in $g_{RR}^{(2)} = 0$. We have seen previously that only the conditional output, that is the readout photon state conditioned on the detection of a heralding photon is expected to be a single photon state. We name the corresponding correlation function $g_{RR|W}^{(2)}$. For the unconditional output, we expect similar to the heralding photon state a thermal state which yields $g_{WW}^{(2)} = 2$ and $g_{RR}^{(2)} = 2$. The advantage of the second-order auto-correlation function is, that it is independent of imperfect detection efficiencies in the limit of low noise. The classical boundary is set by the coherent state which gives $g_{RR}^{(2)} = 1$. States with lower second-order auto-correlation cannot be described in a classical framework and are thus called non-classical.

We will make use of a non-classicality witness that was pioneered by [Cla74]. He considered the cross-correlation between two fields given by

$$g_{WR}^{(2)} = \frac{\langle I_W I_R \rangle}{\langle I_W \rangle \langle I_R \rangle} = \frac{\langle a_W^\dagger a_W a_R^\dagger a_R \rangle}{\langle a_W^\dagger a_W \rangle \langle a_R^\dagger a_R \rangle} \quad (2.48)$$

For a classical field the Cauchy-Schwarz inequality

$$\langle I_W I_R \rangle^2 \leq \langle I_W^2 \rangle \langle I_R^2 \rangle \quad (2.49)$$

has to be fulfilled. Thus, if the inequality is violated the two fields are non-classically correlated. We can rewrite this inequality in terms of correlation functions as

$$1 \leq R_{CS} = \frac{(g_{WR}^{(2)})^2}{g_{WW}^{(2)} g_{RR}^{(2)}} \quad (2.50)$$

Later [SSB⁺12] showed that the above inequality still holds in the case of imperfect detection efficiencies. This witness for non-classicality has been applied in the first implementation of a DLCZ-type experiment [KBB⁺03]. Assuming thermal states for the heralding stage and the unconditional readout with $g_{WW}^{(2)} = g_{RR}^{(2)} = 2$, it suffices in general for the verification of non-classicality to

show $g_{WR}^{(2)} > 2$. This has been used in many recent experiments, e.g. [BFV12], probably due to simpler experimental requirements.

2.8.1 Modelling the correlations

We would like to estimate the expected correlations between detection events. The correct but very cumbersome way would be to combine the four-wave mixing model with the motional averaging and calculate the distribution of the scattered photons in the detection mode. We try to use a different approach. We first identify the different contributions to the detected counts, then assume (or guess) the distributions for these contributions and finally calculate the expected correlations. We note that assuming the distributions includes clever guess-work and we might easily be mistaken. Furthermore, as [MCS⁺15] have shown, adding four-wave mixing and readout as incoherent processes can lead to wrong correlation values. We thus have to take the outcome of this model with a grain of salt. As we shall see in the experimental section however, the model predictions yield reasonable agreement with the experimental results.

From the assumption of thermal states for the output both for write and unconditional readout, we can calculate the expected cross correlation under the following conditions. For perfect detection efficiency, photon number-resolving detection and in the absence of further noise counts this yields

$$g_{WR}^{(2)} = \frac{\langle n_W n_R \rangle}{\langle n_W \rangle \langle n_R \rangle} = \frac{\sum_{n=0}^{\infty} n^2 p(n)}{(\sum_{n=0}^{\infty} n p(n))^2} = 1 + \frac{1}{p_0} \quad (2.51)$$

where we have used n_W and n_R for the number of photons detected during write and read, respectively. We have assumed thermal states with the probability distribution $p(n) = (1 - p_0)p_0^n$, such that p_0 is the probability to have at least one photon in the detection mode. We have furthermore assumed perfect readout efficiency such that $p(n_R) = \delta_{n_W n_R}$. From the above equation, we see that we can reach higher and higher cross-correlation values the lower the scattering probability is.

Imperfect detection efficiency and excess noise counts can have significant impact on the cross correlation. We therefore extend our calculation to include these effects. We start by expressing everything in terms of the probability of creating spinwaves. This yields

$$\langle n_w n_r \rangle = \sum_{x=0}^{\infty} p(x) \sum_{n_w, n_r=0}^{\infty} p(n_w|x) p(n_r|x) n_w n_r. \quad (2.52)$$

where $p(x) = (1 - p_0)p_0^x$ is the probability of having x spin waves excited. The probabilities of getting write and read clicks, conditioned on having x spin

waves excited are

$$p(n_w|x) = \sum_{k=0}^{\inf\{n_w, x\}} \eta_d^k (1 - \eta_d)^{x-k} \binom{x}{k} p_N^{(w)}(n_w - k) \quad (2.53)$$

$$p(n_r|x) = \sum_{k=0}^{\inf\{n_r, x\}} (\eta_d \eta_{RO})^k (1 - \eta_d \eta_{RO})^{x-k} \binom{x}{k} p_N^{(r)}(n_r - k) \quad (2.54)$$

with η_d (η_{RO}) as the detection (read-out) efficiency and $p_N(y)$ as the probability of getting y noise clicks within a pulse. Similarly the mean number of counts during the write process can be calculated

$$\langle n_w \rangle = \sum_{x=0}^{\infty} p(x) \sum_{n_w=0}^{\infty} p(n_w|x) n_w. \quad (2.55)$$

The counts during the read process can be calculated with the same equation after replacing n_w by n_r . In practice the probabilities are only calculated up to a certain cut-off number of spin waves. We should note that in this model we do not separate heralding photons from symmetric and asymmetric collective excitations into different distributions, but we use one common thermal distribution. This approximation is mainly founded on experimental observations $g_{WW}^{(2)} \approx 1.9$. Using two independent thermal processes would result in an auto-correlation that is significantly lower than 2, which would be the value expected for a single purely thermal process.

The next step is to calculate the probabilities of the noise counts. There are different noise processes that can contribute. Leakage (*leak*) of excitation light through the filter to the detector, background counts (*bg*) from detector dark counts or stray light, and four-wave mixing noise (*fwm*). There are two more noise contributions that we observe during the read in the experiment. We will now anticipate these findings from sections 5.2 and 5.5. One of them is spectrally broad, the other narrow. The origin is not yet fully understood. We suspect that they are both related to a scattering process, thus we assume a common thermal distribution for them (labelled *bc*). We further assume that the photons from the four-wave mixing process also follow a thermal distribution. We admit that this last approximation is not very well-founded, but rather a guess. Each thermal distribution is given by

$$p_{thermal}(p_i, k) = (1 - p_i) p_i^k \quad (2.56)$$

where p_i is the probability to have at least one thermal photon. For brevity we will write $p_{th}(k)$ in the following. For the thermal distribution the mean number is connected to p_i via $p_i = \bar{n}/(1 + \bar{n})$.

The leakage light stems from coherent laser light. Thus it follows a Poisson distribution. The background counts are in our case dominated by detector

dark counts, that also follow a Poisson distribution. For this distribution, the probability to have k events is

$$p_{\text{Poisson}}(\bar{n}, k) = \bar{n}^k e^{-\bar{n}} \frac{1}{k!} \quad (2.57)$$

where \bar{n} is the mean number of events. We can thus write the noise contribution in the write process as

$$p_N^{(w)}(n_N) = p_{\text{Poisson}}(\bar{n}_{bg,w} + \bar{n}_{leak,w}^{(det)}, n_N) \quad (2.58)$$

The noise contribution in the read process is

$$p_N^{(r)}(n_N) = \sum_{f=0}^{n_N} \sum_{b=0}^f p_{th}^{(bc)}(b) p_{th}^{(fwm)}(f-b) p_{\text{Poisson}}(\bar{n}_{bg,r} + \bar{n}_{leak,r}^{(det)}, n_N - f) \quad (2.59)$$

We will compare the experimental results with this model in section 5.3.

It is instructive to consider a simple approximation of the model developed above. We can for low excitation probabilities $p_0 \ll 1$, and low noise counts $p_N^{(w)} = p_N^{(w)}(1) \ll 1$, $p_N^{(r)} = p_N^{(r)}(1) \ll 1$ and $p_N^{(w)}(> 1) = p_N^{(r)}(> 1) \approx 0$, simplify the equations 2.52 and 2.55 to

$$\langle n_w \rangle \approx \eta_d p_0 + p_N^{(w)} \quad (2.60)$$

$$\langle n_r \rangle \approx \eta_R \eta_d p_0 + p_N^{(r)} \quad (2.61)$$

$$\langle n_w n_r \rangle \approx \eta_R \eta_d^2 p_0 + \langle n_w \rangle \langle n_r \rangle \quad (2.62)$$

where in the last line we can identify the first term as the readout of collective excitations while the second term are the independent coincidences. From these equations we can calculate

$$g_{WR}^{(2)} = \frac{\langle n_w n_r \rangle}{\langle n_w \rangle \langle n_r \rangle} \approx 1 + \frac{\eta_R \eta_d^2 p_0}{(\eta_R \eta_d p_0 + p_N^{(r)})(\eta_d p_0 + p_N^{(w)})} \quad (2.63)$$

We can now draw three conclusions. First, in the absence of noise ($p_N^{(w)}, p_N^{(r)} \rightarrow 0$), we recover the initial expression $g_{WR}^{(2)} = 1 + \frac{1}{p_0}$ while allowing for imperfect detection efficiency. Second, if we consider noise that we can shift such that we either detect it during the write or during the read process⁸, then detecting it during the write process will lead to a higher cross-correlation value since in practice $\eta_R < 1$. However, if there are further noise contributions during the read process, there will be a trade-off. This is due to the term $p_N^{(w)} p_N^{(r)}$ that is minimal if all the noise is detected either during the write or the read process.

⁸Here we are anticipating the time-dependent noise from the leakage which we can only minimize for a short time window.

Third, if the noise during the read process is dominating over the readout, that is $p_N^{(r)} > \eta_R \eta_a p_0$, we can approximate the cross-correlation as

$$g_{WR}^{(2)} \approx 1 + C\eta_R \quad (2.64)$$

with the constant parameter C . In the next subsection, we will use this approximation to estimate the decay of the cross-correlation.

2.8.2 Lifetime of collective excitations

One important figure of merit of the envisioned single photon source investigated in this thesis is the programmable delay time between the heralding step and the single photon readout. It is thus interesting to understand the effects of a waiting time between the write and read pulse on the collective excitations and on the readout and we attempt a rough estimate in the following. According to the definitions in section 2.7, the mean number of collective atomic excitations is given by

$$\langle b^\dagger b \rangle \propto \left\langle \sum_j \sigma_{sg}^{(j)} \sum_k \sigma_{gs}^{(k)} \right\rangle \propto \langle (J_y - iJ_z)(J_y + iJ_z) \rangle \propto \langle J_y^2 \rangle + \langle J_z^2 \rangle - \langle J_x \rangle \propto e^{-2t/T_2} \quad (2.65)$$

where we have used $\langle [J_y, J_z] \rangle = i\langle J_x \rangle$ and assumed that the macroscopic spin component J_x decays much slower than T_2 .

The mean number of readout photons is according to equation 2.34 in the absence of four-wave mixing proportional to the number of collective excitations at the time of the read pulse. Here we assume that the readout happens on a timescale much faster than T_2 . For a delay τ_D between write and read pulse, this yields for the mean number of readout photons

$$\langle a^\dagger a \rangle \propto \langle b^\dagger b \rangle(\tau_D) = \langle b^\dagger b \rangle(0) e^{-2\tau_D/T_2} \quad (2.66)$$

The readout efficiency is proportional to the mean number of read out photons, thus with the approximation 2.64 we expect also the cross-correlation $g_{WR}^{(2)}$ to decrease for longer delay time with a rate $2/T_2$.

Part II

Experiment

Experimental methods

In this chapter we will mainly describe the setup that is used for the DLCZ-type experiment. The setups for the cell characterization measurements may be different and are detailed in the respective sections.

The optical setup can be subdivided into three main parts (see fig. 3.1). To begin with we prepare the excitation light using a narrowed laser. Then this light is sent to the atomic part before it continues to the filtering and detection setup. Each part will be described in detail in the sections below.

3.1 Excitation light

For the creation of the excitation pulses we require a laser that is narrow in linewidth compared to the filter bandwidth since the scattered photons will have similar linewidth as the excitation light. Furthermore we need to pulse the light power and adjust the frequency of the excitation pulses.

3.1.1 Narrowed laser via optical feedback

We use a home-built external cavity diode laser (ECDL) with additional phase-stabilized weak optical feedback from a cavity transmission. This idea has been applied in various different implementations, using a Fabry-Perot cavity [Hua09], a V-shaped cavity [HNB12] or a triangular cavity [Hay11] [LRB⁺07]. In short, it is related to the operation mode of an ECDL. Spectrally narrow light is sent back into the laser and stabilizes the emission frequency and decreases the laser linewidth. A theoretical analysis of the linewidth reduction has been presented in [LCB89].

We chose the triangular cavity design for two reasons. It avoids direct reflection of non-resonant light back to the laser as in the case of a Fabry-Perot cavity and it allows us simultaneously to filter the light going to the experiment. In a V-cavity this would lead to high losses, since the feedback power is typically

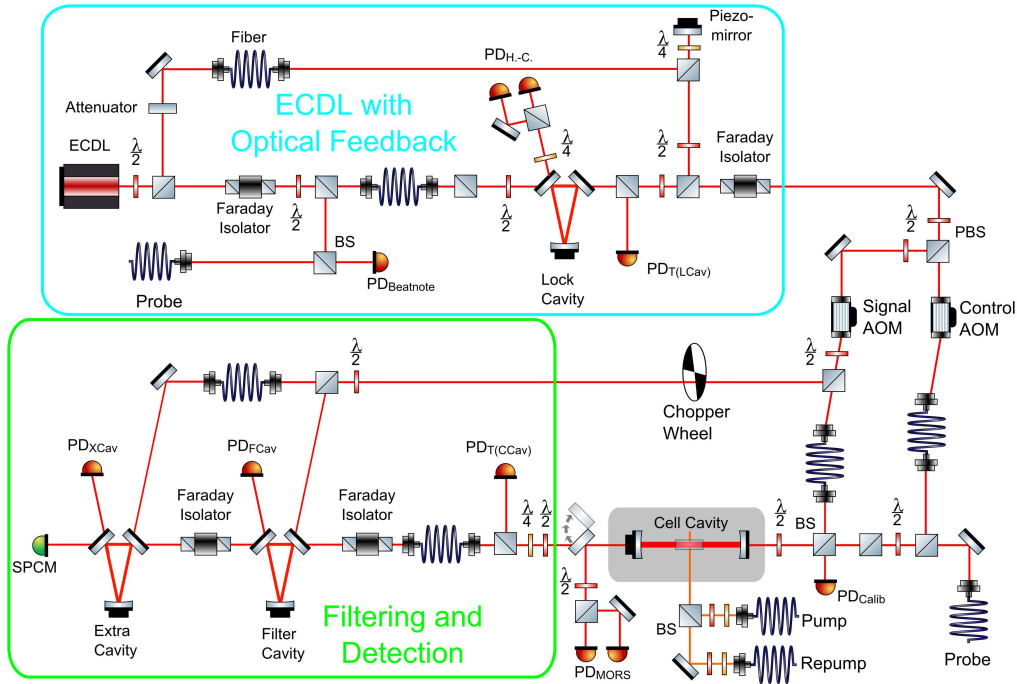


Figure 3.1: Schematics of the optical setup. Only relevant optical elements drawn. Abbreviations are PD: photo diode, AOM: acousto-optic modulator, BS: beamsplitter, PBS: polarizing beamsplitter, SPCM: single photon counting module, ECDL: external cavity diode laser. Beamsplitter cubes are polarizing if not indicated otherwise. Drawing based on *svg component library* by A. Franzen

small. We tried various implementations with triangular cavities that I will briefly present. The first version used the light from the ECDL coupled via mode-matching optics into a triangular cavity. Part of the transmitted light was then retro-reflected through the cavity into the laser (see also [ED16]). The disadvantages of this setup are on the one hand the bad mode-matching of the ECDL output to the cavity. This makes the cavity transmission spectrum not only hard to understand, but can also lead to mode jumps to different transversal cavity modes which also experience optical feedback. On the other hand, the counter-propagating cavity mode that is driven by scattering at the cavity's mirror surfaces leads to optical feedback from the cavity itself. This feedback with random phase will compete with the desired optical feedback and can lead to instabilities and mode jumps.

For the second iteration we solved the mode-matching problem by introducing a single mode fiber between the ECDL and the cavity for mode cleaning (see also [Did14a]). This led to a much cleaner cavity spectrum and better optical feedback locking. However, on top of the random feedback from the counter-propagating cavity mode we also noticed scattering from the angled fiber (APC) leading to competing feedback.

In the third and final iteration as shown in fig. 3.1 we used an isolator in front of the fiber to avoid unwanted feedback. Instead of retro-reflecting through the cavity we coupled part of the transmission through a second single mode fiber which sent the optical feedback via a PBS to the ECDL. We put neutral density (ND) filters in front of this second fiber in order to eliminate direct optical feedback from the fiber or the cavity. Then we could adjust the power of the desired optical feedback that only had to pass through the ND filters once. By replacing the ND filters by an optical isolator we would have reduced significantly the losses of the desired optical feedback. However, the power gain would have been minimal since the power of the optical feedback is low (about -50 dB of the laser output power) and the possibility to forward-couple through the fiber makes the mode-matching between ECDL and fiber mode convenient. In our setup the lock cavity is simultaneously used as a frequency filter since we use the light transmitted through the lock cavity for the experiment. This filters out remaining broadband laser noise [Hay11].

Without optical feedback the linewidth of the ECDL is broader than the cavity resonance. With optical feedback we observe broadening of the resonances when scanning the cavity length. The frequency of the ECDL locks via optical feedback to the cavity resonance and thus keeps high transmission when the length of the cavity tunes the resonance frequency within the capture range. The capture range depends on the power of the optical feedback. However, it is important to send back optical with the correct phase. When the optical feedback enters the ECDL with the wrong phase it interferes destructively and keeps the laser away from this frequency. When the ECDL is optically locked to the cavity, we can estimate the excursions of the transmitted light from the lock cavity resonance from the in-loop Hänsch-Couillaud signal to be typically less than 10 kHz.

A more thorough investigation of the locked laser linewidth was performed for the previous setup iteration in [Did14b] and yielded a linewidth of about 30 kHz over a 10 s window. We assume that the linewidth characteristics did not change significantly from the previous setup iteration to the one described here.

There are two feedback loops active in the optical feedback setup. The first one acts on a piezo-actuated mirror in the feedback path, adjusting the optical path length of the feedback light, to keep it in the regime of constructive interference. This is achieved by keeping the laser on resonance with the cavity. The error signal is derived in a Hänsch-Couillaud setup [HC80], analyzing the circularly polarized components of the light reflected from the cavity incoupling mirror. The reason for choosing a Hänsch-Couillaud lock was the technical simplicity. First, the required birefringence is typically given when using a triangular cavity. Second, a Hänsch-Couillaud setup does not require modulation of the laser, which might even lead to undesired sidebands. We have thus ensured

that the laser stays locked to the cavity resonance as long as the cavity length relative to the free-running laser frequency does not drift out of the capture range. The free-running laser usually stays within a range of a few tens of MHz over a day. The length of the lock cavity however easily drifts by a wavelength over minutes. We therefore implemented a slow (\approx Hz) feedback loop to keep the cavity length stable. The laser light which is locked to the cavity resonance is overlapped with a reference laser (the "probe" laser) and sent on a fast photodiode. From the resulting beatnote signal an error signal is derived in an RF interferometer setup similar to [SEG⁺99]. Via a proportional-integral (PI) controller the feedback signal is sent to the piezo-actuated cavity mirror. The reference laser is stabilized to an atomic reference. Therefore, this second feedback loop does not only improve the long-term stability of the first feedback loop by counteracting cavity drifts, but it also keeps the locked laser stable relative to an absolute atomic frequency reference.

3.1.2 Lock cavity

The lock cavity is a triangular cavity with a roundtrip length of about 1.5 m. The single curved mirror is piezo-actuated, the two flat mirrors are used as in and out-couplers. Astigmatism is kept negligible [RW92] since the opening angle of the triangular cavity is below 2° . The cavity spacer is an H-profile made of aluminium. A wall-thickness of the profile of about 15 mm provides passive stability. The flat mirrors are glued on home-designed bending plates that allow alignment while keeping longterm stability. The spacer is simultaneously used for the lock cavity and the filter cavity in the arrangement shown in fig. 3.2. This was intended to reduce noise from common-mode length changes of the spacer and will be discussed in section 3.4. The spacer rests inside a vacuum tube which is closed on both ends with windows, but not evacuated. There has been no significant change of the cavity stability whether or not the tube was evacuated. We have performed a ring-down measurement at a wavelength of 852 nm and determined the linewidth of the cavity of $\text{FWHM} = (72 \pm 5)$ kHz. For more details see appendix B.

3.2 Vapour cell

The atomic ensemble is in our case an atomic vapour of caesium-133 atoms, contained in a glass cell as shown in fig. 3.3. The exact design of our glass cells varies, but the main pieces are a reservoir with a drop of caesium and a channel where the atom-light interaction takes place. The channel is connected to the reservoir by a small "micro-hole", that allows the caesium vapour pressure to equilibrate, while at the same time keeping the rate at which atoms travel between the two chambers low. The inner walls of the glass cell are coated with anti-relaxation coating. This coating, which consists in our case of carbon

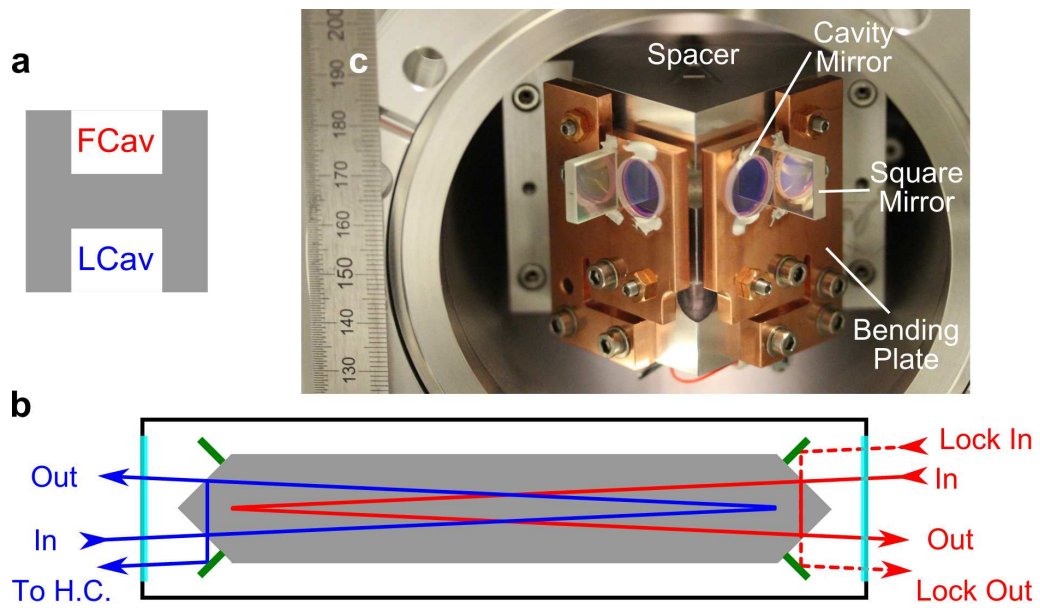


Figure 3.2: Lock and filter cavity. **a** Cross-section and **b** top view sketch of lock cavity (blue) and filter cavity (red) arrangement on the same H-shaped spacer (grey). Additional square mirrors (green) couple the locking beams through the same windows as the inputs and outputs of the cavity. The lock cavity reflection is sent to the Hänsch-Couillaud (H.C.) setup. The filter cavity is locked using a counter-propagating beam. **c** Photo of the cavity setup.

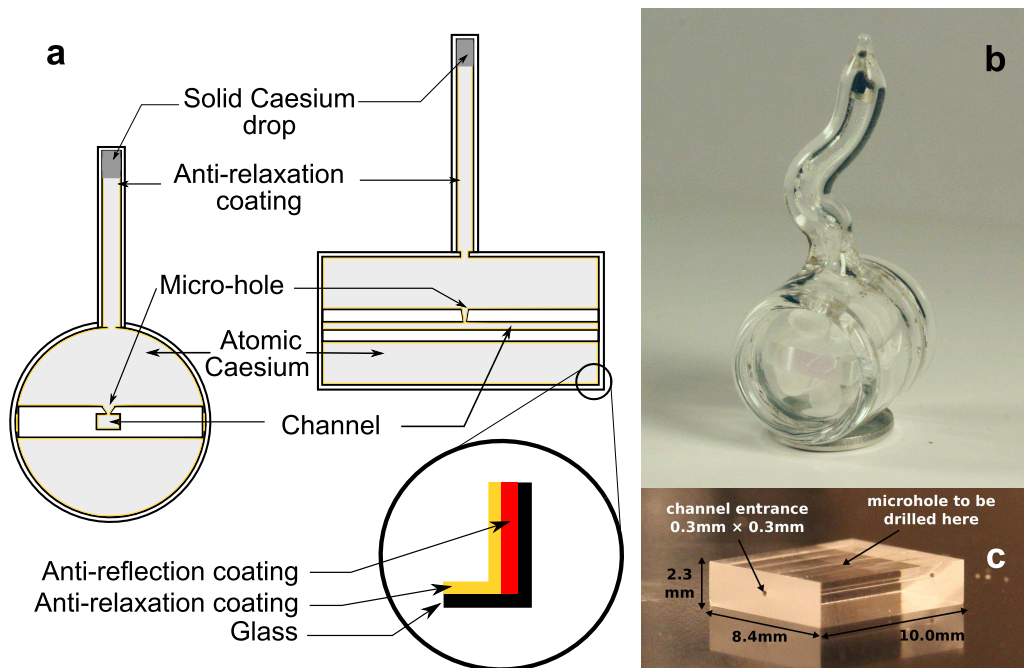


Figure 3.3: The encapsulated microcell design. **a** Sketch of components. **b** Photo of finished microcell. **c** Photo of chip. The images are adapted from [ED16] (a) and [She14] (b), (c).

chains (alkanes or alkenes, sometimes simply called paraffin) with roughly 30 carbon atoms, preserves the atomic state upon many wall collisions [BKLB10]. We will investigate the properties of the vapour cells more in detail in section 4.2.

The cells are evacuated prior to filling with caesium and anti-relaxation coating. It is important that the glass cell is vacuum-tight to avoid oxidizing of the chemically very reactive caesium.

Although many experiments in our group are still conducted using cells with relatively large volumes ($> (5 \text{ mm})^3$), we will focus here mostly on so-called microcells with channel dimensions of $300 \mu\text{m} \times 300 \mu\text{m} \times 1 \text{ cm}$. These dimensions are a compromise between on the one hand a small cross-section for fast motional averaging and a long length for high optical depth and on the other hand low clipping losses for the transmitted light. The basis for all our microcells is the "chip", a rectangular glass substrate with square cross-section channel, as shown in fig. 3.3 c). The micro-hole is a laser-drilled hole from the surface to the channel with a minimal diameter of 20 to $30 \mu\text{m}$.

Most of the cells are fabricated and filled by the skill-full glass-blowing techniques of M. Balabas. One of the main challenges in the cell fabrication has been to achieve high quality optical access along the long channel axis. We present in the following a few solutions to this challenge.

3.2.1 Encapsulated design

The encapsulated design had been developed before the start of this PhD work. An example of such a cell is shown in fig. 3.3 b). The chip with micro-hole is inserted in a tube and closed off with anti-reflection coated windows on both ends. This design allows high quality optical access along the cell. The tube is rather large (half inch diameter) to avoid lens effects for the pump and repump, and to allow space for glass-blowing without the flame heating up the optically relevant center part of the window. After the preparation of the glass body, it is evacuated. Via the attached reservoir ("stem") it is filled with caesium and anti-relaxation coating and then closed by glass-blowing. The biggest part of our micro-cells is in the encapsulated design. An investigation of their properties is presented in section 4.2. Achieving good optical transmission through the channel is very challenging and requires skilled glass-blowing. It has therefore been a long-standing idea in our group to connect windows to the channel ends by some other means. We will discuss possible solutions in the following.

3.2.2 Laser-bonded design

In collaboration with F. Zimmermann and S. Nolte from the University of Jena, a laser-bonded cell design has been developed and tested. Their group had shown successful welding of glass by using femtosecond laser pulses at high

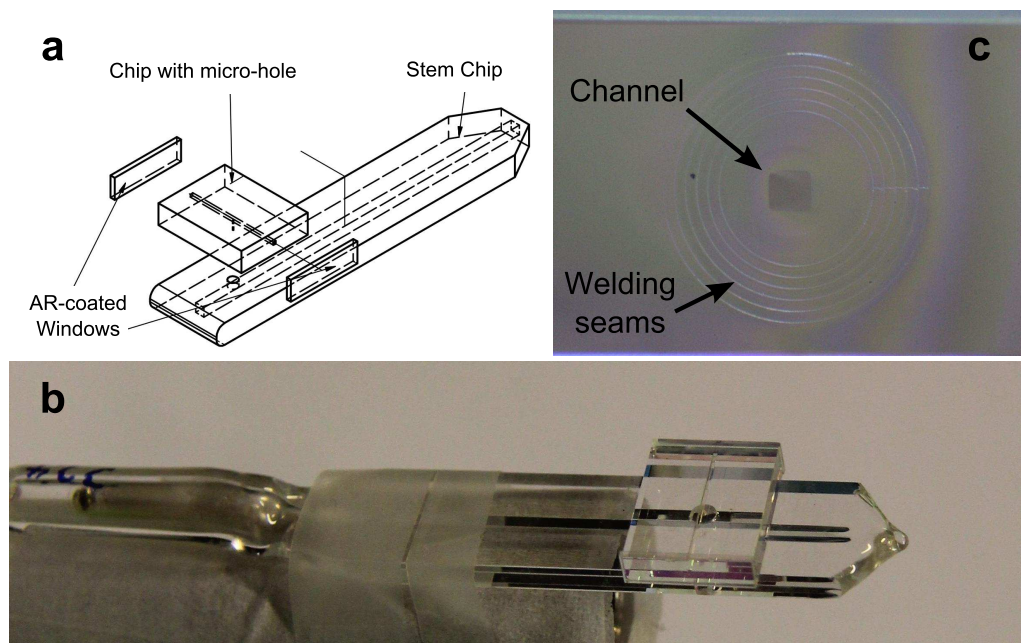


Figure 3.4: The laser-bonded microcell design. **a** Sketch of components. **b** Photo of finished laser-bonded cell in holder. **c** View through the window. The whitish lines encircling the channel cross section are the welding seams between chip and window.

repetition rates [RZTN16]. This welding technique was used to connect the windows on both ends of the chip, and to connect an adapter that allowed later filling and glass-blowing at a distance of a few cm. The arrangement, the welding seams and the finished laser-bonded cell are shown in fig. 3.4. Prior to the welding procedure, the glass pieces had been polished and optically contacted. After successful preliminary tests of the vacuum-tightness of the welded connection, a few cells with this design were fabricated. This design has a few advantages. The optical transmission loss should be given only by the anti-reflection coating and the loss due to passing through the glass of the window.¹ The fabrication procedure of the glassware can in principle be industrialized and the cell can be miniaturized. The design opens new possibilities for closely-spaced multichannel cells, providing good spatial resolution and simplifying large-scale testing of cell properties. We note however, that the fabrication method is a complex process, including many steps (polishing, optical contacting, welding) as well as special equipment (femtosecond laser).

3.2.3 Integrated cavity

One reason for the requirement of high optical transmission is the need for a cavity around the cell. A cavity around the cell will always be affected by losses from the window. A different approach is to include the cavity mirrors

¹This assumes no further losses due to the later anti-relaxation coating and filling.

within the encapsulated cell. This solves the issue of window losses at the expense of reduced cavity length tunability. Furthermore it crucially relies on initial cavity alignment. We have made preliminary tests with encapsulated cells with integrated cavities. Due to glass-blowing constraints on the thickness of the substrates, we actually sandwiched the mirrors between the chip and the windows, where the windows were connected to the outer tube by glass-blowing. Instead of a regular chip we used capillaries with an inner diameter of 1 to 6 mm. The increased diameter compared to the microcells was meant to reduce the possible clipping losses due to mirror misalignment. The results are briefly presented in section 4.2.1.

3.2.4 CO₂ laser melting and anodic bonding

For completeness we briefly mention two other techniques that have been tested. Other group members (R. Thomas, K. Jensen and B. Albrecht) have investigated the use of a focussed CO₂ laser to locally melt the interface between window and chip. Melting along the edge from all four sides should then lead to a vacuum-tight connection between window and chip. When testing this procedure, cracks appeared along the edges. Even if these cracks did not compromise the vacuum-tightness at first, they started to do so after hours or days. We assume that the cracks appear due to the high temperature gradients during the melting procedure, leading to inhomogeneous stress in the glass. A different approach was the use of anodic bonding, a technique frequently used to connect thin wafers. It has also been shown to work for 7 mm-sized vapour cells [DKL⁺14]. Although following a similar procedure as in this reference, our anodic bonding tests with chips and windows have until now not led to successful bonding. Further investigation will be necessary to identify the possible reasons.

3.2.5 Atomic density

If not indicated otherwise, we use the cell G2 which is an encapsulated cell with alkane coating for our experiments. We typically heat the cell up to a temperature of about 42.3°C to increase the atomic density. The current through the magnetic field coils already heats up the cell to around 38°C, the additional heating is done with a high-resistance heating wire wound around the coil frame. The heating wire is intertwined to suppress the creation of a magnetic field. The temperature is measured with a temperature sensor placed in the air inside the shield above the cell. From an absorption spectroscopy measurement at a temperature of 43°C we determine an atomic density of around $17.5 \cdot 10^{16} \text{ m}^{-3}$. Comparing this value to the theoretical value given in [Ste10], we estimate that we overestimate the temperature systematically by 3 to 5°C. This may be due to the thermal coupling of the cell to the table via the cell

holder. The atomic density at our typical temperature is about 7 times higher than at room temperature.

3.3 Cell cavity

The cell cavity is placed around the cell and consists of two mirrors that are mounted on the optical table. Both mirrors have a radius of curvature of 110 mm. Their spacing of 218 mm leads to a waist radius of $55 \mu\text{m}$, which has been experimentally confirmed to yield a good compromise between clipping losses and filling factor of the cell cross section. The incoupling mirror has a reflectivity of $R_{in} = 0.997$, and the outcoupling mirror has a reflectivity of $R_{out} = 0.8$. This yields an empty cavity finesse of $\mathcal{F}_e \approx 28$. If a cell is placed inside the cavity, then the transmission losses of the cell reduce the cavity finesse. We measure a finesse $\mathcal{F}_{G2} \approx 18$ for the cell cavity with cell G2. This is less than what we expected since we had measured the single pass cell transmission to be 98% in a previous experiment. We attribute the reduction in transmission to the fact, that this transmission measurement was performed with a powermeter and did thus not take into account possible wavefront distortion which matters when placed inside a cavity. The cell cavity is by design asymmetric in reflectivities to ensure efficient outcoupling through the outcoupling mirror. Dividing the output coupler transmission by the total loss yields an outcoupling efficiency of $\eta_{out} \approx T_{cell}(1 - R_{out}) / (1 - R_{in}R_{out}T_{cell}^2) \approx 62\%$, where we have multiplied the expression by T_{cell} since a photon has to cross the cell on average once before arriving at the output coupler.

The FWHM of the cell cavity is 38 MHz. Since it is significantly larger than the Zeeman splitting it should allow us during a Raman scattering process within the Zeeman levels to have both, excitation and scattering frequency, nearly resonant in the cell cavity. We note that atomic phase shifts can make this slightly more complicated, see section 4.4.

We lock the cell cavity with the probe laser. As mentioned in section 3.1.1, the probe laser is stabilized with respect to an atomic transition. At the same time it is far detuned (≈ 1.6 GHz) from the atomic resonance, which reduces the interaction of the atoms in the cell with the probe laser. This makes the probe laser a good choice for locking the cell cavity. The probe laser is modulated by ± 300 kHz around the center frequency with a modulation frequency of 10 kHz. The transmitted light (in the case of a MORS measurement the reflected light) is detected with a photodiode. The error signal is extracted with a lock-in amplifier and sent to a PI controller that gives feedback on the piezo-actuated outcoupling mirror to stabilize the cavity length. The cell cavity and the magnetic shield are covered in a box to protect them against temperature drifts and acoustic noise.

3.4 Filtering and detection

In the DLCZ-type experiment, the scattered photons will be collinear with the excitation light. Hence, we need to filter around 10^8 excitation photons per heralding photon (see section 2.5) after the output from the cell cavity. Our filtering includes two stages: polarization filtering and spectral filtering.

As shown in fig. 3.6 a), the magnetic field is oriented perpendicular to the excitation and scattered light propagation direction. For the excitation light we use linear polarization in vertical (y) direction. This is perpendicular to the magnetic field direction, which gives $\sigma_+ + \sigma_-$ -polarization for the atoms. As shown in fig. 3.6 c) and d), we choose the scattered heralding and readout photons to be π -polarized. Thus, we can use a polarization selective element to separate excitation and scattered photons. In our setup, we use a Glan-Thompson polarizer that can reduce the transmission of the excitation light down to $5 \cdot 10^{-5}$. We need to carefully adjust the output polarization from the cavity with a half-wave plate and a quarter-wave plate to reach this reduction. We note that we typically cannot reach this extinction level for both write and read pulse. We suspect, that remaining birefringence in the cavity leads to polarization-rotation of the output light. This rotation depends on the atomic state, hence it changes over time when the atomic state decays (see section 4.4). Optimizing the polarization extinction during the write pulse, we have typically at least one order of magnitude worse extinction during the read pulse.

The spectral filtering consists of two cavities, the filter cavity and the extra cavity. Both cavities are intended to filter out the excitation light during write and read pulses. We will refer to the remaining transmission of this light as leakage. The filter cavity also serves a second purpose. It is a narrowband cavity with a linewidth of FWHM= (66 ± 1) kHz to achieve motional averaging (see section 2.5). The extra was added later, when the filter cavity with an expected leakage reduction to about $2 \cdot 10^{-4}$ at a Zeeman splitting of 2.4 MHz proved not be sufficient, hence the name "extra" cavity. Both cavities are triangular cavities with flat incoupling and outcoupling mirrors and piezo-actuated curved mirror. The filter cavity uses the same spacer as the lock cavity and is oriented as shown in fig 3.2.

The filter cavity is situated in a vacuum tube. This was intended to shield the lock cavity and filter cavity from acoustic noise. Since we do not see any noise performance improvements whether the tube is evacuated or not, we conclude that most of the noise is transmitted via the holders that support the cavities mechanically. Closing off the tube however helps against pressure drifts, that occur e.g. when opening the door. When we lock the narrow laser via optical feedback to the lock cavity and then send it through the filter cavity, we observe substantial noise at a frequency around 400 Hz. The magnitude of this noise is such, that the average transmission through the filter cavity

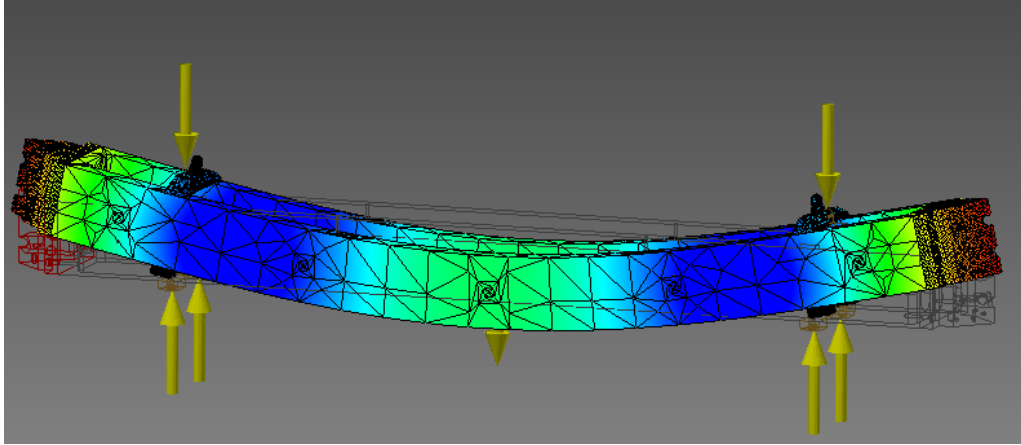


Figure 3.5: Fundamental bending mode, visualized via Autodesk Inventor modal analysis. Displacement is coloured from small (blue) to large (red). We considered gravity acting on the whole spacer which is supported by resting on the bottom feet and being slightly clamped (with a force of 1 N) at the top

decreases to 66%, considerably lower than the maximum transmission of 90%. We attribute this noise to the vertical bending motion of the spacer. This claim is supported by a modal analysis of the cavity structure with Autodesk Inventor. The eigenfrequencies of the fundamental bending mode is according to the modal analysis at 445 Hz. The corresponding displacement is visualized in fig. 3.5. Using the same spacer for lock cavity and filter cavity was meant to reduce relative drifts of the cavities. In the bending mode, the cavity lengths are anti-correlated, which yields the opposite of the intended advantage.

Compared to the filter cavity with a round trip length of about 1.49 m, the extra cavity is significantly shorter with a round trip length of 198 mm. A block of aluminium with holes drilled for the optical path serves as a spacer for the extra cavity. The flat mirrors are mounted in adjustable gimbal mounts screwed to the spacer. This design has been presented previously in [ED16]. The linewidth of the extra cavity is $\text{FWHM} = (894 \pm 2) \text{ kHz}$ which yields a leakage reduction to $3.5 \cdot 10^{-2}$ at a Zeeman splitting of 2.4 MHz. Further specifications of the cavities can be found in appendix B.

Both cavities are locked using modulated light coupled into the counter-propagating mode. The modulation is similar to that of the cell cavity lock light, achieved by stepping the frequency of the lock light via an AOM with a rate of 10 kHz. The frequency step of $\pm 3 \text{ kHz}$ is here much smaller than for the cell cavity due to the narrower linewidth. The AOM used for the modulation is the "signal" AOM (see fig. 3.1). For each cavity the transmitted lock light is detected, the signal demodulated and fed back on the cavity piezo via a PI controller. An optical isolator between the cavities avoids cross-talk of lock light between the cavities. Even though the lock light is in the counter-propagating mode, scattering on the mirror surfaces can end up in the forward

mode. Hence, a chopper wheel blocks the lock light during the experiment to avoid excess noise counts in the SPCM.

The scattered photons are sent to a single photon counting module² (SPCM), which is an avalanche photodiode operating in Geiger mode. The dark count rate of the detector is only 10 Hz. We experimentally determined the quantum efficiency $\eta_{SPCM} = 52\%$ of the detector at a wavelength of 852 nm. This was done by comparing the detector counts of an attenuated beam with a power meter measurement of the non-attenuated beam with the help of calibrated attenuators. The pulse-width of the SPCM output is 15 ns, the dead-time of the detector is according to the specifications 43 ns.

Since the SPCM is operating in Geiger mode, it is typically not photon number resolving. However, the temporal shape of the photons is in our case comparable to the photon lifetime in the filter cavity which is about $2 \mu\text{s}$. This is much longer than the dead time of the detector. Thus, for low photon rates we can consider the SPCM effectively as photon number resolving.

The photons have to pass many optical elements from the output of the cell cavity to the SPCM. The detection efficiency (including the quantum efficiency of the SPCM) is measured individually during each measurement run in situ by sending a "check pulse" with calibrated power through the setup (see section 3.6). Typically this leads to a detection efficiency from the cell cavity output to the detected count of typically around 9%. A big part of the transmission losses is due to the filter cavity ($T \approx 66\%$). The other main contributors are the isolators (each $T \approx 88\%$), the extra cavity ($T \approx 90\%$) and the fiber connection ($\approx 78\%$). The latter is present, since the cell cavity, due to historical reasons and space constraints, is on a different optical table than the lasers and the other cavities.

3.5 Optical pumping and magnetic field

For the DLCZ-type experiment, we need to initialize the atoms in one Zeeman sublevel. We have chosen the state $|4, 4\rangle$ as the initial ground state. Two diode lasers are used to optically pump the atoms into this state. The repump laser is locked on the $F=3$ to $F'=2,3$ crossover transition of the D_2 line. Its main task is to bring the atoms that have dropped into $F=3$ back into the $F=4$ manifold, hence the name "repump". The pump laser is locked on the $F=4$ to $F'=4$ transition of the D_1 line. The beams are overlapped on a non-polarizing beamsplitter before they are expanded with a pair of cylindrical lenses to achieve good overlap with the elongated channel. The pump and repump beams are sent on the cell "from the side", that is perpendicular to the excitation beam. Pump and repump light are collinear with the magnetic field and σ_+ polarized. They optically pump

²LaserComponents Count-10

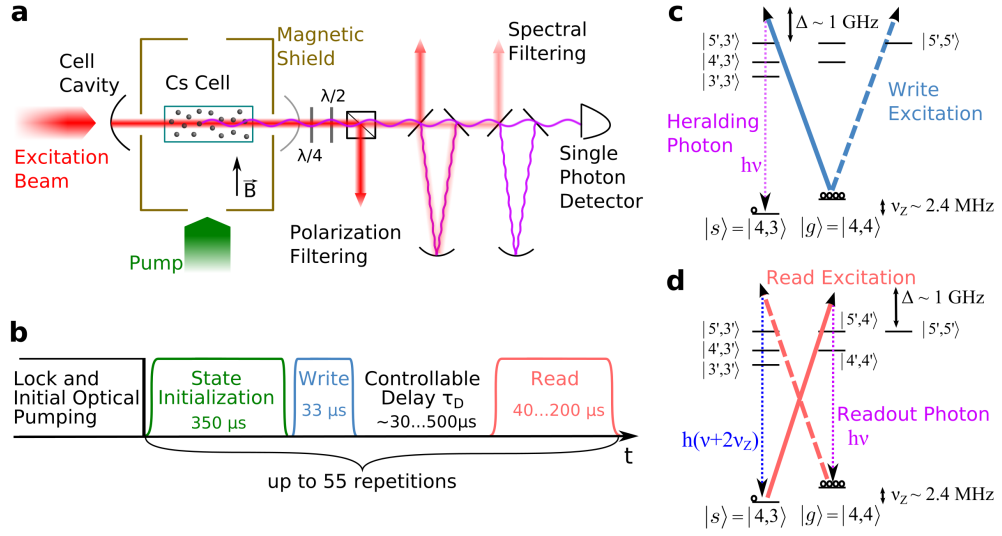


Figure 3.6: **a** Setup schematics, overview. **b** Experimental sequence. **c** Level scheme for write process, **d** level scheme for read process. Only relevant levels shown.

the atoms into the state $|4,4\rangle$, which is a dark state for the pump light. We typically achieve an atomic spin polarization of $> 98\%$.

Our experiments will mainly address Zeeman transitions. Since the splitting depends on the magnetic field, it is crucial that the atoms experience a stable and homogeneous magnetic field. In our lab environment there are many sources of potential magnetic field noise. The cell is therefore residing in a magnetic shield to protect it against these disturbances from the outside. The shields and coil systems have been used in many previous experiments and a detailed description can be found in [Fab14]. We will only give a brief overview here. The magnetic shield consists of three layers of μ -metal and one layer of iron, shielding against low frequency noise. The innermost layer is an aluminium cylinder, shielding against high frequency noise, while providing at the same time the frame for various sets of coils. We typically have two of these sets of coils in use. The main B_x coil creates a bias field in x -direction. Since the field B_x decreases along the z -axis, which is the long direction of the cell, we use a double saddle coil to compensate these inhomogeneities. We perform most of the presented experiments at a Zeeman splitting of $\nu_Z \approx 2.38$ MHz, which corresponds to a magnetic field of 6.8 G. We note that this yields a quadratic Zeeman splitting of around 1.43 kHz. Hence, we are not resolving the Zeeman levels with our spectral filtering. Besides the static magnetic field coils we also have a Helmholtz coil pair inside the aluminium layer, which is used to drive radio-frequency (RF) transitions.

3.6 Experimental control and sequence

The DLCZ-type experiment requires us to apply a sequence of light pulses. This sequence is shown in fig. 3.6. The general timer of the experiment is the chopper wheel. It rotates with a constant speed, opening the lock path for 24 ms and blocking it for 41 ms. The state of the chopper is detected by an FPGA, which accordingly controls the experiment.

The FPGA runs with a clock frequency of 80 MHz and reads out the SPCM counts every clock cycle. The pulse sequence actions are executed every $1 \mu\text{s}$. The frequencies for all AOMs are created by a DDS board. For historical reasons, the DDS board is connected to a different FPGA, which we will call DDS-FPGA to avoid confusion. In the DDS-FPGA we pre-set a table of possible frequencies. The FPGA communicates to the DDS-FPGA via TTL signals which frequencies to pick. The DDS-FPGA checks for these TTL signals every $1 \mu\text{s}$. An overview over the chosen frequencies is given in section 3.6.1.

The only parts of the experiment that are not affected by the chopper are the laser sources. For the narrow laser this means, that the optical feedback and the beatnote lock are constantly active. If the laser lock fails, it relocks automatically. Probe, pump and repump frequency stabilizations are completely independent. We will briefly outline the experimental sequence below.

Locking: This phase starts when the chopper has opened the lock beams. The first task here is to verify that the laser, filter cavity and extra cavity are locked. If not, the cavities are scanned to find the maximum transmission and then locked. The cell cavity has to be checked and relocked manually. If yes, this is the duration where the PI controllers are active and feedback is sent to the cavities, including the cell cavity, to stabilize their length. This implies that the narrow laser and the probe laser frequencies are dithered. The pump and repump lights are off. The phase stops by freezing all the locks shortly before the chopper blocks the lock beams.

Initial optical pumping: When the chopper has blocked the lock beams, the FPGA shuts off all the beams and opens the pump and repump beam via their respective AOMs. The duration of this stage is about 4 ms.

DLCZ-type: Each sequence consists of up to 56 repetitions of the following steps. The number of repetitions is chosen such that we utilise fully the time window given by the chopper wheel.

- **State initialization:** The state initialization only differs from the previous optical pumping in terms of the duration. We have experimentally confirmed, that pumping the atoms into $|4, 4\rangle$ takes longer initially when starting from a thermalized ensemble, than when only write and read

pulses have disturbed the atomic state. Therefore we have in each repetition a short state initialization phase of typically $350 \mu\text{s}$. Since the pump and repump light do not increase the SPCM counts, we use this duration also to determine the background counts if the SPCM is gated on.

- **Write:** We turn off pump and repump beams before the write process starts. For the write pulse we use the "control" AOM (see fig. 3.1) with a frequency tuned one Zeeman frequency below the lock light frequency. To avoid spectral broadening, the beginning and the end of the pulse are shaped smoothly over about $15 \mu\text{s}$ by controlling the RF power sent to the AOM. The pulse duration is $33 \mu\text{s}$, measured from half-on to half-off time. We gate on the SPCM and start detecting counts with the start of the first repetition of the write pulse. In section 6.1, we will replace the optical write pulse by a RF excitation of similar duration.
- **Delay:** During the following delay time τ_D , all beams are turned off. The duration is variable, with a lower limit of $30 \mu\text{s}$ to avoid overlapping write and read pulses.
- **Read:** For the read pulse we use again the "control" AOM, now with a frequency tuned one Zeeman frequency above the lock light frequency. The smoothly shaped pulse with similar switching time as the write pulse has a duration of $200 \mu\text{s}$, measured from half-on to half-off time. For the data analysis we can choose a shorter time window for the read.

Check pulse: After the end of the last repetition there is one last state initialization phase, followed by the check pulse. For this pulse, we use π -polarized light, i.e. with the polarization of the scattered photons, at the expected frequency of the scattered photons. This allows us to check the detection efficiency for each measurement individually. The pulse is switched by the "signal" AOM and the pulse duration is 1 ms. The light power is chosen very low (about 1 pW) to ensure that there is no leakage during the write and read pulses. After the end of the check pulse we gate off the SPCM .

3.6.1 Frequencies

We will give a brief overview of the frequencies used in the experiment. Pump and repump light are locked on atomic transitions as detailed in section 3.5. Before being sent on the atoms, they are shifted up in frequency by 80 MHz by an AOM used for switching. The probe laser is stabilized with respect to an atomic transition. The resulting detuning on the atoms after being shifted down in frequency by an AOM is $\Delta_{\text{probe}} \approx 1.52 \text{ GHz}$ blue from the $F=4$ to $F'=5$ caesium D_2 transition. We have chosen a beatnote frequency of $f_{\text{beatn}} = 750 \text{ MHz}$, such that the narrow laser ends up with a detuning of $\Delta_{\text{Narrow}} = 928 \text{ MHz}$ blue

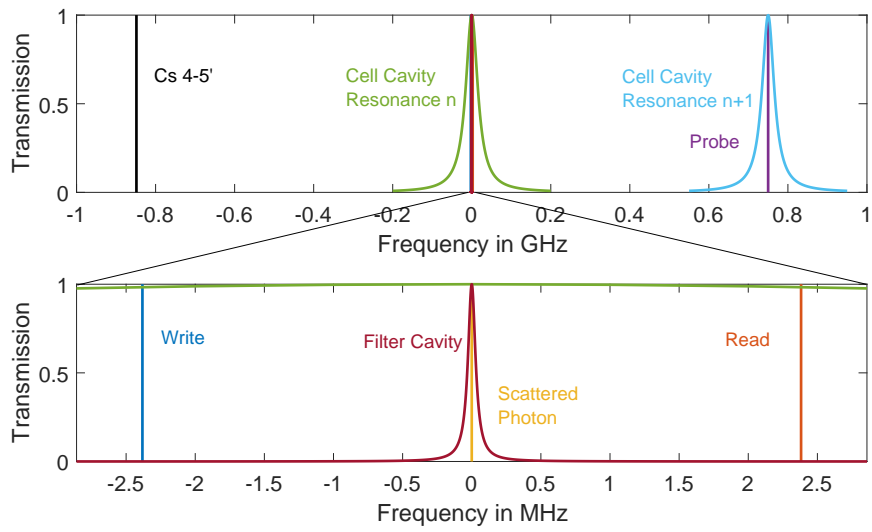


Figure 3.7: Overview of the frequencies used in the experiment. The origin of the frequency axis is the frequency of the narrow-band scattered photons. Expected cavity transmissions are plotted in relevant regions as Lorentzians. The lower graph zooms into the center region of the upper graph.

from the $F=4$ to $F'=5$ caesium D_2 transition. The detunings and the relevant resonances of cell cavity and filter cavity are plotted in fig. 3.7

Characterization of cells

4.1 Figures of merit

There are three main figures of merit for us determining the quality of the vapour cells: on-resonant optical depth, coherence time and cross section. The optical depth is set by the length of the cell, the temperature and the finesse of the cavity around the cell. The lower the losses due to the cell windows and body, the higher finesse and thus the higher interaction strength we can achieve with this cavity. The length of the cell is a easily accessible design parameter. The maximum achievable temperature depends on the chemical properties of the anti-relaxation coating. The cell transmission has shown considerable variation and will be covered in the section below. The coherence time T_2 limits in the end the storage time of the collective excitation, thus the time-bandwidth product. The cross section sets the timescale of motional averaging, simultaneously affecting T_2 and the transmission due to clipping. The cross section is also a well-defined design parameter. Thus, with all the above interconnections we can translate the initial figures of merit into new experimental figures of merit. For given cell dimensions these are: maximum achievable temperature, off-resonant transmission and coherence time.

In the following we will present an investigation of the transmission properties of encapsulated microcells. Then we will address the issue of disappearing atoms that can occur at elevated temperatures. Regarding the atomic state and the coherence time we will present two experiments. The first demonstrates a - to the best of our knowledge - novel technique to measure populations in different atomic states after some waiting time. This allows an estimate of the purity of the readout. The second is a microwave spectroscopy measurement that measures the coherence time on the hyperfine transition.

4.2 Cell transmission

We investigated the transmission of the cells by following the properties of 20 encapsulated microcells (J1-J20) through the fabrication process. We measured the transmission of the cells and of its components in two different ways. Either by simply measuring the power in front and behind with a powermeter. The measurement with the powermeter was quickly to perform, the precision was however limited to about 1%. Alternatively we inserted the cell into a testing cavity with similar parameters compared to the cell cavity, except for a higher output coupler reflectivity (97%) for more precise transmission measurements. We then compared the linewidth of the empty cavity with the linewidth when the cell was aligned inside the cavity and calculated the single pass loss. The advantage of the cavity measurement was besides higher precision that the transmission was measured in an environment similar to the later experiment, accounting for possible mode distortion. If a lower transmission is not due to absorption or scattering but due to reflection, this will change the cavity spectrum. Depending on the phase of the reflection this can lead to elaborate cavity spectra, especially in the case of multiple reflecting surfaces.

We started with measuring the transmission of the initial components, yielding 0.6% single pass loss for a single antireflection-coated window of 1.6 mm thickness and 0.1% single pass loss for a 10 mm long glass chip with a 300 μm square channel. The glass pieces were then assembled with careful glass-blowing techniques by M. Balabas, before annealing at 560°C. While cells from generation E (2013) only showed a typical transmission of 93% to 95%, probably limited by the hot flame affecting the anti-reflection coating, the assembly technique reached typical transmission of above 97% for generation J (2016) cells.

Before filling with anti-relaxation coating the cells are washed with hydrochloric solution. This had been tested previously by co-workers not to have any effect on the anti-reflection properties of the window.

We then tested the cells again after coating with anti-relaxation coating and filling with caesium vapour. The applied coatings were all carbon chain coatings. We tested standard paraffin, alkene, alkene with specified carbon chain length (25-55) and a mixture of alkane and alkene (C30). These coatings had been evaporated into the cells at different temperatures. A higher evaporation temperature leads to a higher vapor pressure and thus more carbon chain molecules available in the cell after closing it off from the paraffin reservoir. The resulting thickness of the coating has an impact on the coherence time. The range of evaporation temperatures had been chosen for each coating type individually such that the coating resulted in reasonable coherence times. In fig. 4.1 on the left we show the cell transmission after the application of anti-relaxation coating and filling with caesium vapour versus the evaporation temperature and in fig. 4.1 on the right we show the difference between the transmission of

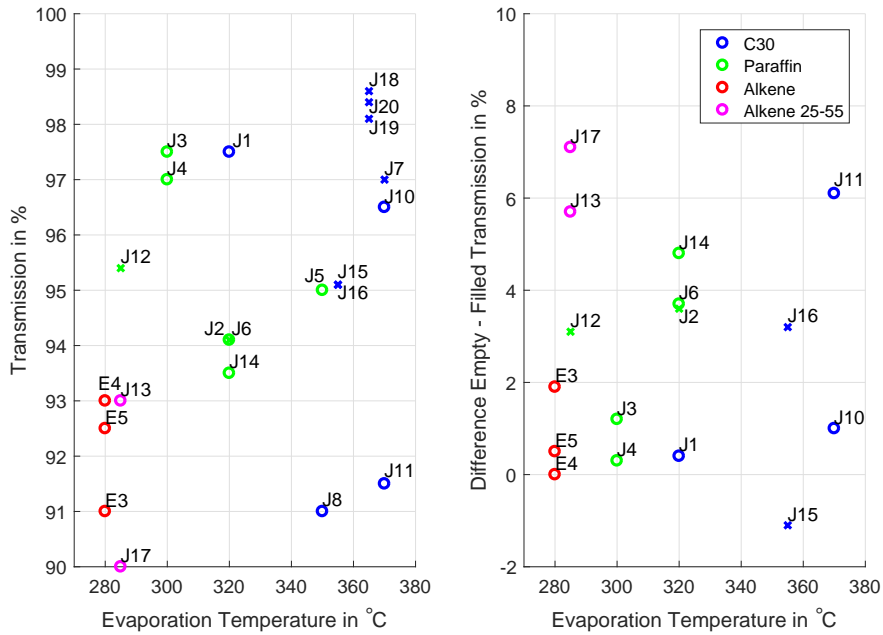


Figure 4.1: Left: transmission of filled cells versus anti-relaxation coating evaporation temperature, Right: Difference in cell transmission before and after anti-relaxation coating versus coating evaporation temperature. Circles (crosses) measured with powermeter (cavity). Cell J9 not shown in left figure had transmission lower than 90%. Cells not included on the right have not been measured before filling. Cells E3...5 from previous generation are shown for reference.

the empty cell and the filled cell versus evaporation temperature. We do not observe a clear trend of the transmission with the evaporation temperature. Assuming that a higher evaporation only leads to a thicker anti-relaxation coating we conclude that either this thickness does not have significant influence on the transmission or that the reduced transmission cannot be simply explained by extra absorption by the coating. We note that in one case (J15) we even get an improvement of the cell transmission after coating. This could be due to residuals in the channel that were cleaned away during the coating procedure.

We further investigated the relation between transmission and coherence time. This is shown for about 36 encapsulated microcells and one laser-bonded cell with different coating materials in fig. 4.2. We notice that the alkene cells on average have longer coherence times than paraffin cells, that in turn have longer coherence times than cells with C30 coating. It occurs rarely that a cell has both long coherence time and high transmission simultaneously. The results from the exceptional cells I16 and F1 however speak against a potential hard limit of simultaneous excellence. The spread of the results shows that there is no straightforward relationship between coherence time and transmission. Other parameters (curing time, microhole diameter, cleanliness) that have not been

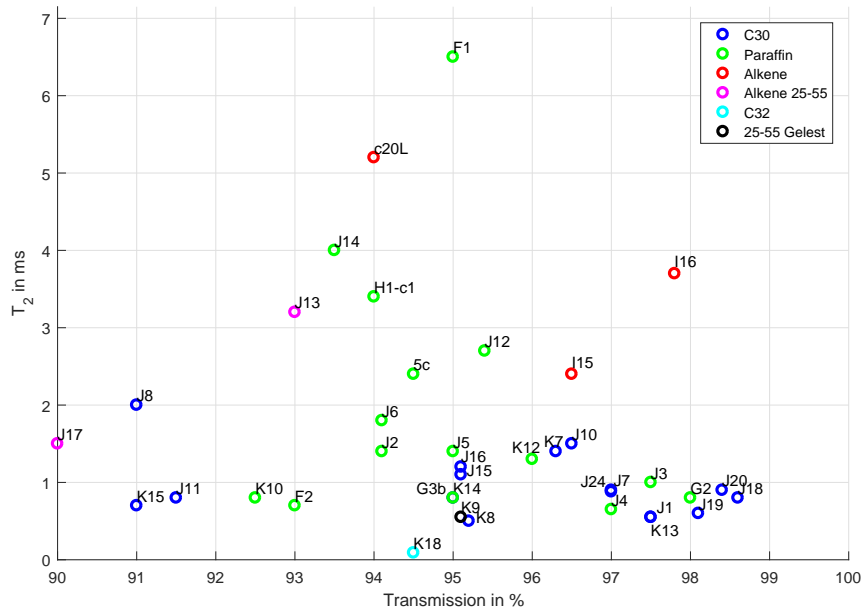


Figure 4.2: Coherence time versus cell transmission. Shown are the results from 36 encapsulated microcells and one laser-bonded cell (J24) with different coating materials.

investigated here, seem to have significant influence on the results.

The measured reduction in transmission can be either due to losses (absorption, scattering) or reflections. We verify that both can have relevant influence by measuring the reflections from two empty laser-bonded cells, and from two coated and filled laser-bonded cells under zero degree angle of incidence. While the empty cells showed a reflection of 0.2% and 0.4%, we measured reflections of 1% and 2% for the filled cells respectively. Inside a cavity this can lead to coupled cavity effects. Even if the reflectivity of the window is much lower than the reflectivity of the cavity mirrors, it can have a significant effect on the transmission of the cavity. As an example, a surface inside a cavity similar to the cell cavity with 0.8% reflection into the cavity mode could change the cavity transmission by about 10% depending on the phase of the reflection due to its exact position [Rak00]. Tilting the cell to avoid reflections into the cavity mode typically leads to increased losses by clipping. However, the issue of variations in transmission is solved by using a cell design where windows are attached at a slight angle. This was implemented starting from cell K13. For previous cells exhibiting the reflection issue the cavity can usually be optimized to obtain maximum transmission, by adjusting the cell position and angle. This was typically done in the transmission measurements presented above.¹ It should be noted, that also for the cell G2 that was chosen for the

¹Chronologically, we only realized later that reflections are probably causing the sensitivity

DLCZ-type experiment, the reflection could cause a relative change in transmission by up to 10%.

4.2.1 Integrated cavity cell

Towards the end of this PhD project we had the opportunity to measure the characteristics of three integrated cavity cells, that are cells with mirrors inside the encapsulation. We measured the finesse after the assembly via glass-blowing, and after coating with alkene/paraffin coating and filling with caesium.

The cell L8 has a capillary with an inner diameter of $d = 1$ mm, one high-reflective mirror ($R_{HR} = 99.7\%$) and one lower-reflectivity mirror ($R_{PR} = 99\%$). Compared to a measurement with the bare mirrors, the finesse dropped by a factor 5 after glass-blowing, resulting in Finesse of $\mathcal{F} = 117$. This reduction is attributed to clipping losses. After the subsequent filling with caesium and coating with alkene, the finesse dropped again by more than a factor 5. It is unclear if second drop in finesse is related to the anti-relaxation coating, or due to clipping in the narrow capillary, since the parts inside the cell appeared not to be well fixed in place.

The other two cells with a capillary of $d \approx 6$ mm, each with a pair of high-reflective mirrors, showed very good finesse after the glass-blowing assembly ($\mathcal{F} \approx 1100$), only marginally worse than measured for the bare mirrors. For one of the cells (L9), the transmission was however only 13%, indicating that the glass assembly outside the cavity introduced significant losses. One could also observe cracks in one of the mirror substrates. They probably appeared due to the glass-blowing flame, inhomogeneously heating up the few mm thick mirror substrate. The cracks did not seem to affect the high reflective surface at the beam position, such that the finesse could still be high. After filling with caesium and coating with alkene, the finesse dropped to $\mathcal{F} \approx 260$. This is equivalent to a total intracavity loss of 2.4%. The cell transmission on resonance dropped even further to 0.4%.

For the third cell (L4), filling with anti-relaxation coating failed. After the cell had been emptied and cleaned with hydrochloric acid (10%), we observed a significant drop in finesse by about a factor of three. Repeating the cleaning process decreased it even further. We therefore conclude that the hydrochloric acid attacks the high-reflective coating.

The conclusion we draw from the preliminary results with the integrated cavity cells is two-fold. On the one hand, it is encouraging that we have reached a total intracavity loss of 2.4%. On the other hand, this is only marginally better than for the top-performing encapsulated cells. At the same time we have only managed to produce cells with rather large capillaries. Reliable alignment

of alignment.

and fabrication of microcells with integrated cavities and low clipping losses remains a distant prospect.

4.3 Issue of disappearing atoms

It occurred several times, that the caesium atoms seemed to disappear from the channel of the microcells since there was no atomic signal (spectroscopy or MORS) from the channel. This happened for various microcells with different coatings and it only happened when the cell was at temperatures above 30°C. However, it seemed to occur at random times and was not correlated with a specific temperature. When the atoms disappeared from the channel we could still measure an atomic signal from the encapsulated volume outside the chip. This led to the conclusion that the microhole became clogged by anti-relaxation coating. The caesium atoms inside the channel are slowly (within minutes) absorbed by the anti-relaxation coating and in this case cannot be replaced by atoms from the reservoir. The clogging may happen more easily at elevated temperatures because the anti-relaxation coating becomes less viscous. However, assuming a simple flow of melted coating into the microhole does not provide a full explanation since the clogging happened with the microhole oriented up as well as down. Typically after heating the cell to about 80°C, we can observe atoms inside the channel again. We assume that a homogeneous redistribution of anti-relaxation coating has then opened the microhole again. We also have cases where this heat treatment is not successful. For one of the cells, the laser-bonded cell J24, we have tested a different method to free the microhole. Inspired by [HK02] we focused a laser with wavelength $\lambda = 460$ nm and a power of $P \approx 1$ W into the microhole. With a spot diameter of around 100 μm we did not achieve any success, even for very long (≈ 20 s) illumination duration. However, with tighter focussing down to about 30 μm the unclogging was successful. Photos from before, during and after are shown in fig. 4.3. The top row displays a side view. The vertically oriented channel is connected by the conical microhole to the reservoir that is on the left, outside of the picture. In a) the surface of the conical shape has a homogeneous matt finish and we observe a lot of scattered light from the channel. The bright spot of scattered light is caused by the room light. The violet laser that is then directed from the left through the conical part into the center of the microhole. b) shows the situation after the 0.9 s long laser pulse. We see that the matt finish has become more transparent in the conical part, and the distribution of light scattered from the channel has changed as well. We claim that this shows the anti-relaxation coating having been cleaned away from parts of the conical microhole, and from parts of the inside of the channel. Even though we cannot observe the coating distribution inside the minimal diameter section of the microhole, this claim is confirmed by two effects. Firstly, we observed an atomic signal from inside the channel after this process, speaking for an unclogged

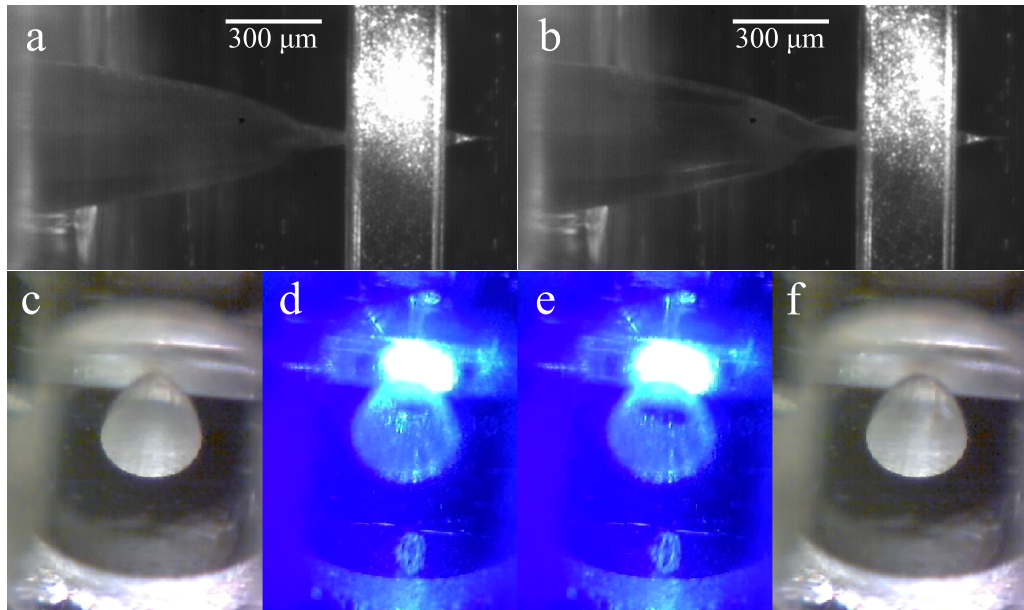


Figure 4.3: Unclogging the microhole by laser heating. Top row: side view with channel vertically and conical microhole connecting reservoir (left out of picture) to channel. a: before, b: after laser pulse. Bottom row: diagonal view through reservoir onto conical microhole and channel (horizontal). c: before, d: 0.4 s after start of, e: 0.9 s after start of, f: after laser pulse

microhole. Secondly, we measured short coherence times that could be significantly increased by recuring, that is heating the cell to higher temperature to homogenously distribute the coating. This confirms, that the coating distribution inside the channel was changed significantly by the violet laser pulse. We can also observe these changes in real time. The bottom row shows frames from a webcam video that was taken during the experiment. The view is from a different angle. This time we look through the reservoir chip into the wide opening of the conical microhole (frosted bell shape in the center). The channel is oriented horizontally behind the microhole. This camera view was mainly meant for alignment of the violet laser focus at reduced powers and makes it less obvious to see changes between before (c) and after (f) the laser pulse. A close look reveals a darker shade on microhole and channel after the pulse. It is however interesting that we can observe a change even during the laser pulse. After the automatic brightness adjustment of the camera we observe figure d) 0.4s after the start of the laser pulse. The bright spot is scattering of the violet laser from the channel. During the laser pulse this bright spot grows in size while the scattered light from the microhole reduces. This is shown in e), taken half a second after d). We chose a minimal laser pulse duration of 0.9 seconds simply because the violet laser was activated and deactivated with a mechanical push-button switch.

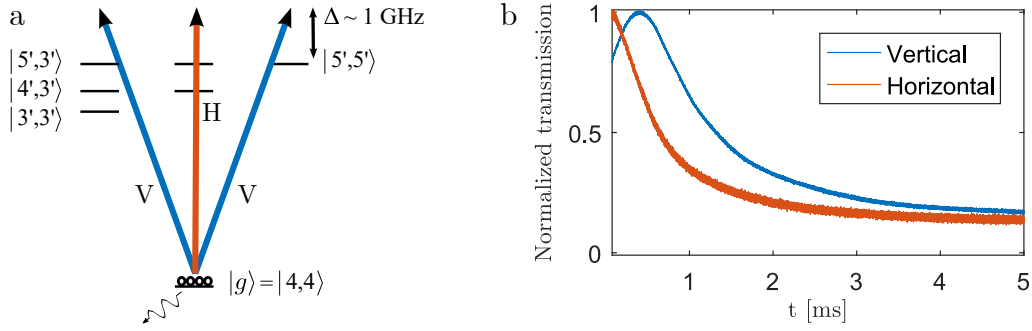


Figure 4.4: **a** Horizontal (red) and vertical (blue) polarization acting on atoms in the initial ground state. The coupling to different excited states with different detunings leads to birefringence. Decay of the ground state population causes time-dependent phase shift. **b** Cell cavity transmission measured for horizontally and vertically polarized light versus time after pumping has been turned off. Figure adapted from [Did17].

4.3.1 Conclusion

We have been able to confirm that atoms disappearing from the channel can be caused by a clogged channel and we have demonstrated a solution for the issue by cleaning with a laser pulse. We have strong indications that there is an intensity threshold for the cleaning process to be successful and we have been able to monitor the process in real time. A thorough investigation beyond the scope of this project, applying different pulse durations and powers while monitoring with better quality imaging, may reveal interesting effects and lead to new methods of locally treating the anti-relaxation coating.

4.4 Cell cavity drift due to atomic relaxation

The cell cavity resonance depends on the atomic state despite the large detuning of ≈ 1 GHz. We conclude this from the following observations. If the atoms are pumped, the resonances for horizontal and vertical polarization do not overlap. Furthermore we see that the resonance is shifted, depending on whether the atoms are pumped or unpumped. The observed birefringence is an atomic effect and not due to the cell windows, since it vanishes for very large detuning or for an unpumped ensemble. We also see that this birefringence and the resonance shift reduce when the atoms thermalize after the pumping has been turned off. This is shown in fig. 4.4. The phase shift depends on g^2/Δ , thus it depends on the number of atoms and the atomic coupling. Horizontal and vertical polarization couple to different excited states. Although for very large detuning the coupling of horizontal and vertical light to the atoms will be similar, it matters for detunings that are comparable to the excited state splitting, which is apparently the case for our detuning of ≈ 1 GHz. When the optical pumping stops, the atomic state starts to thermalize. Partly atoms decay into

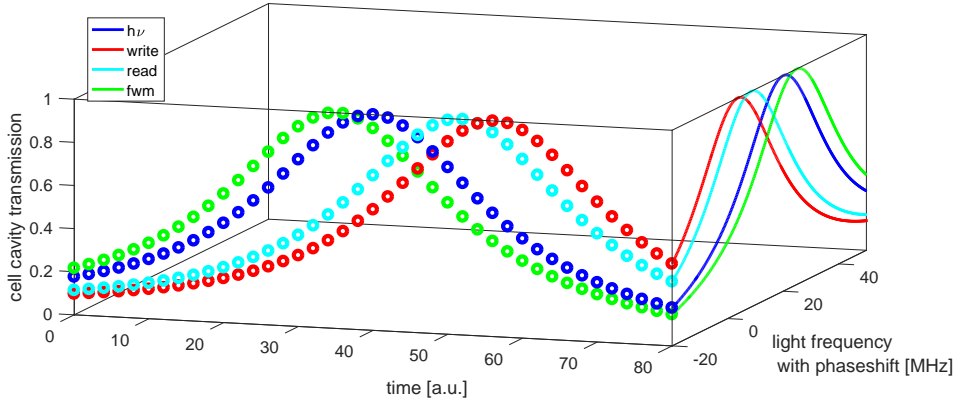


Figure 4.5: Expected cell cavity resonance for light at write (red) and read (cyan) frequency in y polarization and single photon (blue) and four-wave mixing (green) frequency polarized along π , shown for light detuned from the D2 line as in the experiment (frequency-axis shifted arbitrarily). y -polarized light is shifted relative to π by 14 MHz as typically observed in the experiment. Assuming linear change of phase shift over time, the cavity resonance shift for the respective frequencies is displayed (circles).

$F=3$ and are be much further detuned, and atoms redistributing in the Zeeman levels of $F=4$ will contribute with different couplings. When the ensemble has reached the thermal state, which reacts similar to any light polarization, the phase shift has vanished. What are the consequences that the phase shift will have on our pulsed experiments?

First of all we have to be careful when locking the cavity. The atomic phase shift on the lock light can depend on the power of pump and repump light. A drift in their power can then move the locked cavity resonance frequency. Furthermore, we have to choose where we want to lock the cell cavity. In the DLCZ-type experiment we consider four relevant frequencies. During the write process it will be the excitation and the scattering. The desired scattering during the read is at the same frequency as during the write. During the read we then also have the excitation and the undesired scattering due to four-wave mixing. The excitation beams will be polarized orthogonal to the scattered photons. In fig. 4.5, we have sketched the transmission of these four fields against frequency (including the birefringent effect) and against time. According to [NMT⁺17], the interaction strength of a Raman transition involving to transition frequencies A and B will in a cavity depend on $\sqrt{T_A T_B}$ where T_A and T_B are the cavity transmissions at the respective frequencies. We also need to consider, that the atomic phase shift changes on a time scale similar to our experimental timescale. Thus we need to choose a locking frequency for the cell cavity, where we have good interaction with the required frequencies at the relevant durations. We have chosen the conditions according to fig. 4.6. The

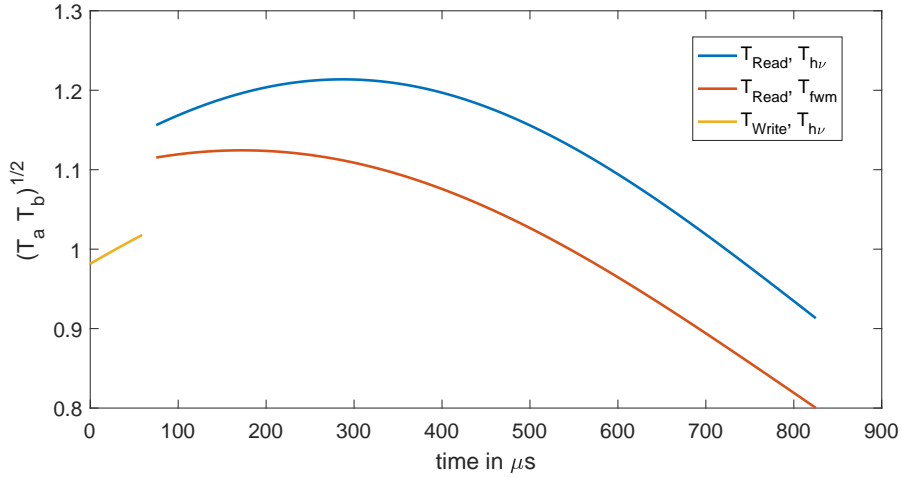


Figure 4.6: Square root of the product of the expected cell cavity transmission at excitation and scattering light frequencies, plotted versus time. The time-axis origin starts with the write pulse. The y-axis is normalized to mean value of one during the write pulse. Shown are the pairs: read excitation and desired photon (blue), read excitation and four-wave mixing scattering (red), write excitation and heralding photon (yellow).

plot was obtained by fitting a Lorentzian² to the transmission of the read excitation light. Then the transmission was inferred for the other frequencies and polarizations, while assuming constant birefringence.

4.5 Atomic decay and coherence times

4.5.1 Continuous MORS

The magneto-optical resonance spectroscopy (MORS) is our workhorse for determining the atomic properties of caesium inside the cells. The simplest way is the continuous MORS described in [JSSP04]. Here the atoms are polarized with a circularly polarized repump parallel to the magnetic field. The resulting collective spin can be excited by an RF coil to precess around the magnetic field, when the RF coil current is modulated at the Larmor frequency. Linearly polarized probe light, far-detuned from atomic resonance, passes through the atoms perpendicular to the magnetic field. The polarization modulation of this light due to the atoms is analysed with balanced polarimetry³. When the frequency of the RF excitation is slowly swept across the Larmor frequency, the polarimetry after lock-in detection yields the MORS signal (example shown in 4.9). The coherence time in the dark T_2 between magnetic sublevels can be determined from the peak width extrapolated to zero probe and RF power. The

²This is a linear approximation for the decay of the phase shift.

³The setup for continuous MORS is until here similar to the pulsed MORS setup in fig. 4.7.

name "continuous" comes from the fact that the light beams are all continuously on.

The continuous MORS allows to measure the coherence time T_2 with a simple experimental setup. One should note that the repump is on during this measurement, however the pump is turned off to avoid light-induced decoherence. Therefore the coherence time is only measured for a not so well polarized atomic ensemble. Nevertheless we typically use the continuous MORS to adjust pump and repump alignment and polarization by tuning the pump frequency to be resonant with the $F = 3$ manifold, thus acting similar to the repump. Furthermore the continuous MORS can be easily performed when the cell is residing inside a cavity, making it a handy tool for us.

MORS Theory We will briefly present the theoretical derivation of the MORS signal as shown in [JSSP04]. In subsection 4.5.3 we will then build upon this derivation for the pulsed MORS signal.

We consider atoms distributed among the Zeeman levels m_F of a single hyperfine manifold F , with the quantization axis defined by a bias magnetic field along the x -axis. The macroscopic spin \vec{J} will couple to the magnetic field via $H = g_F \mu_B \vec{J} \cdot \vec{B} + O(B^2)$ with the Bohr magneton μ_B and the hyperfine Landé factor g_F . We apply a magnetic radio frequency field $B_{rf} e^{-i\omega_{rf} t}$ with frequency ω_{rf} , amplitude $B_{rf} = |B_{rf}| e^{-i\phi}$ and phase ϕ . This contributes $g_F \mu_B J_y |B_{RF}| \cos(\omega t + \phi)$ to the interaction. With the definitions of J_y and J_z from section 2.7 this yields the Hamiltonian [JSSP04]

$$H = \sum_{m=-F}^F \hbar \omega_m \rho_{mm} + \frac{g_F \mu_B}{4} \sum_{m=-F}^{F-1} C(F, m) \rho_{m+1, m} B_{rf} e^{-i\omega_{rf} t} + C(F, m) \rho_{m, m+1} B_{rf}^* e^{i\omega_{rf} t} \quad (4.1)$$

where ω_m is the resonance frequency of the m -th level. The Heisenberg equation of motion for the atomic coherences then yields

$$\frac{\partial \rho_{m, m+1}}{\partial t} = \frac{1}{i\hbar} [\rho_{m, m+1}, H] - \frac{\Gamma}{2} \rho_{m, m+1} \quad (4.2)$$

where we have added a decay of the coherences. We introduce slowly varying operators with $\rho_{ij} = \tilde{\rho}_{ij} e^{-i\omega_{rf} t}$ and we neglect second order coherences $\rho_{m, m+2}$ and $\rho_{m-1, m+1}$, which is a valid approximation for small excitations. We can then write

$$\frac{\partial \tilde{\rho}_{m, m+1}}{\partial t} = (i(\omega_{rf} - \omega_{m+1, m}) - \Gamma/2) \tilde{\rho}_{m, m+1} + i \frac{g_F \mu_B}{4\hbar} C(F, m) B_{rf} [\rho_{m+1, m+1} - \rho_{mm}] \quad (4.3)$$

where $\omega_{m+1,m} = \omega_{m+1} - \omega_m$. The solution for this equation is

$$\begin{aligned} \tilde{\rho}_{m,m+1}(t) &= \tilde{\rho}_{m,m+1}(0)e^{(i\Delta-\Gamma/2)t} \\ &\quad - \frac{i\chi}{i\Delta - \Gamma/2} [\rho_{m+1,m+1}(t) - \rho_{m,m}(t)](1 - e^{(i\Delta-\Gamma/2)t}) \end{aligned} \quad (4.4)$$

where $\Delta = \omega_{rf} - \omega_{m+1,m}$ and $\chi = \frac{g_F \mu_B C(F,m) B_{rf}}{4\hbar}$.

In the continuous MORS case, where all laser beams and the RF excitation are continuously on, the oscillations dampen out and we reach the steady state solution

$$\rho_{m,m+1}(t) = \frac{-i\chi}{i\Delta - \Gamma/2} [\rho_{m+1,m+1} - \rho_{m,m}] e^{-i\omega_{rf}t} \quad (4.5)$$

which leads as explained in [JSSP04] to the MORS signal

$$\text{MORS}(\omega_{rf}) \propto \left| N \sum_{m=-F}^{F-1} \frac{C(F,m)}{i\Delta - \Gamma/2} [\rho_{m+1,m+1} - \rho_{m,m}] \right|^2 \quad (4.6)$$

4.5.2 Pulsed MORS - characterization of state initialization

The pulsed MORS measurement is performed in a very similar setup as the continuous MORS. For the pulsed MORS measurement we start out with a simultaneous repump and pump pulse, polarizing the atoms. After switching it off, we apply a short RF pulse at the Larmor frequency. The pulse is spectrally broad enough to address all Zeeman sub-levels. The Zeeman levels are at high Larmor frequencies resolved and separated by the quadratic Zeeman splitting. The RF pulse excites the collective spin that now starts precessing around the magnetic field. Linearly polarized probe light, far-detuned from atomic resonance passes through the atoms perpendicular to the magnetic field. The polarization modulation of this light due to the atoms is analysed with balanced polarimetry. The setup for pulsed MORS is shown in fig. 4.7, here for $t_{wait} = 0$. The decoherence of the collective spin precession leads to an output signal that is a damped oscillation. If the Zeeman levels are resolved by their quadratic splitting we observe a beating between the respective oscillations. Extrapolating to zero probe power allows us to measure the coherence time in the dark, T_2 . A pulsed MORS measurement method has already been described in [JSSP04]. However, in contrast to their method, we use a pulsed RF excitation. This seemingly small, but important difference renders the snapshot experiment, described below, possible.

We typically perform a pulsed MORS measurement to determine the atomic state achieved by the pump and repump procedure. For the microcells we can achieve an atomic polarization of about 98% (see [Fab14]). Pulsed MORS allows us to measure the coherence time of this very well polarized atomic state.

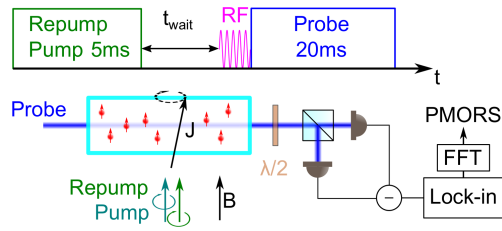


Figure 4.7: Pulse sequence and setup for pulsed MORS measurement.

This is different for the continuous MORS measurement, where we typically only use the repump to avoid pump-induced broadening. The coherence times measured by MORS and PMORS can differ if the coherence time depends on the atomic polarization, e.g. if atom-atom collisions are frequent.

The main disadvantage of the pulsed MORS measurement is the complicated behaviour when measuring an atomic ensemble inside a cavity. The beating signal from the pulsed MORS leads to revivals of the oscillation every time the oscillations rephase. At the same time the atomic decay changes the optical path length and therefore the resonance condition of the optical cavity. The resulting change of the transmission shifts the signal amplitude of the revival. Furthermore, the changing intracavity power can lead to varying light-induced decoherence. The interplay of these parameters can lead to interesting features as the line-broadening or narrowing depicted in fig. 4.8. Even though a thorough investigation of this feature might reveal some interesting physics, this is beyond the scope of this project. More importantly this feature is not hindering us from obtaining the relevant parameters.

Since we expect the coherence time not to be limited by spin exchange collisions, we can use continuous MORS to determine the coherence time. If required we could perform a simple pulsed MORS measurement by reflecting the probe light that has passed through the cell out of the cavity. For balanced polarimetry on this light we would not have to consider any cavity effects. For the snapshot experiment described below we have chosen a third alternative. We took the cell out of the cavity setup and measured it in a different experimental setup.

4.5.3 Pulsed MORS - snapshot of time evolution

In this section we present a novel experiment that allows to measure the atomic distribution among Zeeman and Hyperfine levels over time. With regard to the DLCZ-type experiment, the main motivation for us is to know the fraction of atoms that has decayed to the storage state until the collective excitation is read out. As [BZP⁺16] points out, this fraction contributes excess photons to the single photon read out. Setting a lower limit for the single photon fidelity then allows to give a maximum storage time for the collective excitation.

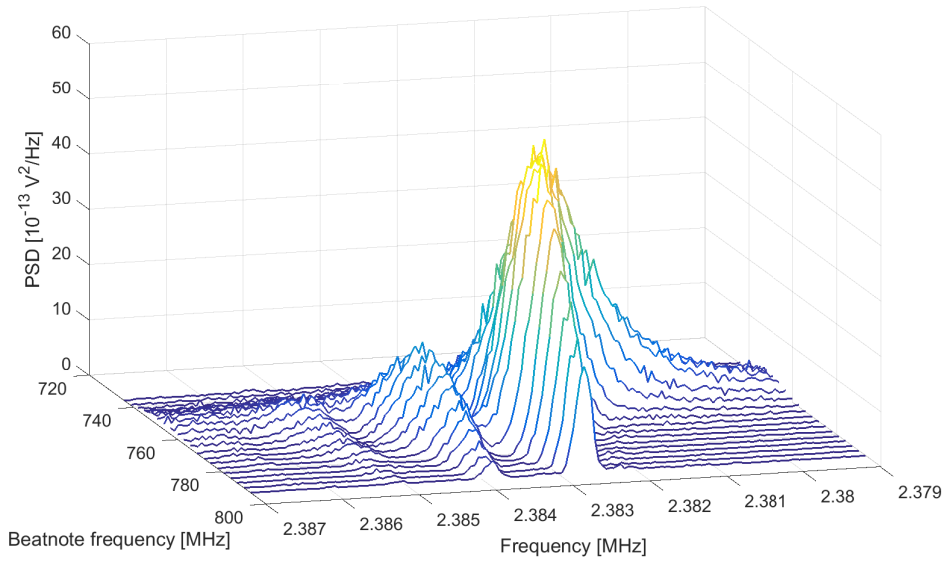


Figure 4.8: Pulsed MORS spectra from F=4 of cell inside cavity for different initial cavity resonance frequencies. The cavity is only locked during the pumping sequence using the "probe" laser, blue-detuned from F=4 by about 1.6 GHz. The pulsed MORS signal is measured using the "control" laser, which is tuned closer to the caesium line by the beatnote frequency. We observe several features of the atomic signal depending on the initial "control" laser detuning from the cavity: narrowing and broadening of the lines, change in height of the secondary peaks relative to the main peak and shift of the main peak center frequency.

The pulsed MORS experiment can be used to determine the atomic state distribution at the time of the RF excitation. The main idea of this experiment is to let the atomic state evolve for some variable time t_{wait} before applying the RF excitation. From a series of these snapshots of atomic distributions, we can determine the evolution of the atomic distribution.

Pulsed MORS Theory The pulsed MORS that we will focus on now, is different from the case considered in [JSSP04], where the RF excitation was continuously on. We consider an experimental sequence where we turn off pump and repump at t_0 . Then after a possible waiting time we turn on a short RF pulse from t_1 to t_2 , and then directly start measuring the polarization rotation with probe light.

The pumping procedure relies on spontaneous emission and destroys all coherences. We assume that during the following waiting time we do not have mechanisms creating any coherences, thus we have $\rho_{m,m+1}(t_1) = 0$. However, the level populations may have changed due to collisions. Using the correct

timings, equation 4.4 then yields after the RF excitation yields

$$\tilde{\rho}_{m,m+1}(t_2) \approx -\frac{i\chi}{i\Delta - \Gamma/2} [\rho_{m+1m+1}(t_1) - \rho_{mm}(t_1)] (1 - e^{(i\Delta - \Gamma/2)(t_2 - t_1)}) \quad (4.7)$$

where we have assumed that the RF pulse is so short and weak that we can neglect any population transfer during the pulse and therefore approximate $\rho_{mm}(t_2) \approx \rho_{mm}(t_1)$. The RF pulse is off during the following probing hence the coherence will simply show damped oscillations

$$\rho_{m,m+1}(t) = \tilde{\rho}_{m,m+1}(t_2) e^{(-i\omega_{m+1,m} - \Gamma/2)(t - t_2)} \quad (4.8)$$

Inserting⁴ this result into the collective spin J_z defined in equation 2.37 yields

$$J_z(t) = \sum_{m=-F}^{F-1} \text{Im}[r_{F,m} e^{(-i\omega_{m+1,m} - \Gamma/2)(t - t_2)}] \quad (4.9)$$

where we have collected all the prefactors into

$$r_{F,m} = -\frac{1}{2i} N_{F,m} C(F, m) \frac{i\chi}{i\Delta - \Gamma/2} [\rho_{m+1m+1}(t_1) - \rho_{mm}(t_1)] \quad (4.10)$$

with $N_{F,m}$ as the number of atoms in the respective level. We have thus transferred the difference of atomic populations at the moment of the RF pulse into the collective spin J_z , which we then read out. This resembles taking a snapshot of the atomic population difference at time t_1 . Now we only need to link the collective spin to the balanced polarimetry output. We have already introduced this connection in equation 2.43.

Analysis In the experiment we send the polarimetry signal to a lockin amplifier and record both quadratures. Therefore we multiply the balanced polarimetry expression S_y^{out} from equation 2.43 including the sum over both manifolds with a sine at the lockin frequency ω_{LI} yielding

$$X' \propto \sum_F a^{(F)} \sum_{m=-F}^{F-1} \text{Im}[r_{F,m} e^{(i\omega_{m+1,m} - \Gamma/2)(t - t_2)}] \sin(\omega_{LI} t) \quad (4.11)$$

and with a cosine giving P' accordingly. We neglect the fast oscillating terms and get expressions for the outputs X and P . For operational simplicity we do not fit these expressions directly to the time traces of the lockin output, but we

⁴We use here $\rho_{m+1,m}(t) = \rho_{m,m+1}^*(t)$, thus $\rho_{m+1,m}(t) - \rho_{m,m+1}(t) = -2 \text{Im}[\rho_{m,m+1}(t)]$

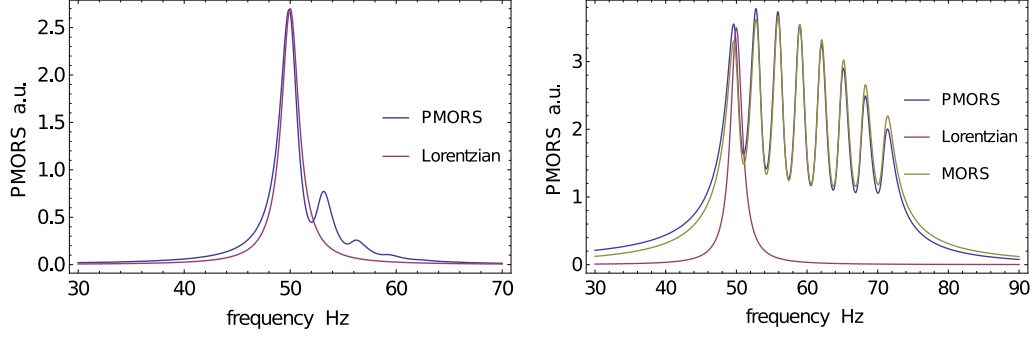


Figure 4.9: Comparison of PMORS, Lorentzian and MORS for high atomic polarization (left) and low atomic polarization (right)

calculate

$$|Ft(X + iP)(\omega)|^2 \propto \left| \sum_F a^{(F)} \sum_{m=-F}^{F-1} r_{F,m} \frac{\sqrt{2/\pi} (\Gamma + 2i\omega_{LI} - 2i\omega_{m+1,m})}{(\Gamma - 2i(\omega - \omega_{LI}) - 2i\omega_{m+1,m})(\Gamma + 2i(\omega + \omega_{LI}) - 2i\omega_{m+1,m})} \right|^2 \quad (4.12)$$

where Ft is the Fourier transform. We will call this expression the PMORS function in the following.

Comparing MORS, PMORS, Lorentz The description of the complicated spectrum can be simplified significantly by assuming a distribution of the populations as $\rho_{mm} \propto \epsilon^m$. This model has been applied successfully previously [JSSP04] and we will use it in the following. The parameter ϵ is directly related to the atomic polarization. We note that the PMORS function can be approximated by a Lorentzian of similar width in the case of high atomic polarization, as shown for $F=4$ in fig. 4.9 on the left. The agreement with the MORS function from equation 4.6 is even better. If they were both plotted they would overlap within the drawn line. On the right we observe that for very low atomic polarization the MORS and the PMORS function differ slightly, most notably in the tails.

The full resulting spectrum shows eight peaks for $F=4$ and six peaks for $F=3$. Each peak stems from two neighbouring Zeeman levels and is centred at the respective Larmor frequency ν_L . The separation between the peaks is given by the quadratic Zeeman splitting, $\nu_{QZ} = 2\nu_L^2/\nu_{hfs}$, where ν_{hfs} is the hyperfine splitting. The separation between the manifolds stems from the different Landé factors, $g_{F=3}$ being about 0.3% bigger than $g_{F=4}$ in amplitude, and having opposite sign. We typically work at Larmor frequencies where the quadratic splitting is bigger than the peak width, such that the lines are resolved.

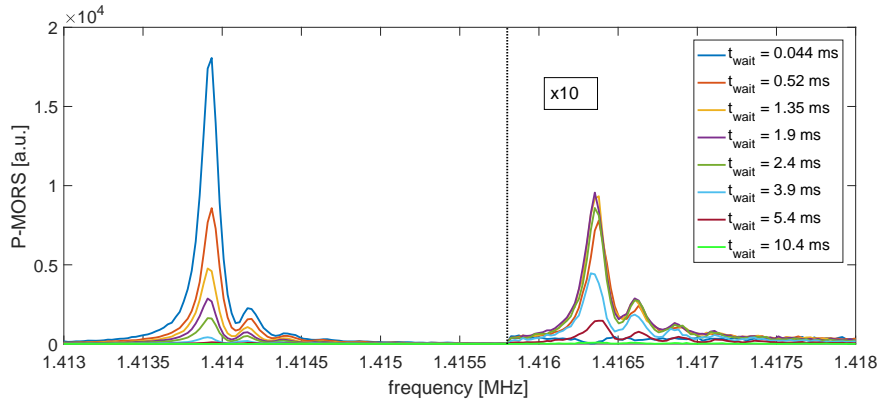


Figure 4.10: PMORS spectra for different waiting times before applying the RF excitation. The signal on the right of the dotted line has been multiplied by 10. The signal attributed to F=4 (F=3) is on the left (right). For longer waiting times the signal from F=4 decreases, the signal from F=3 first increases, then decreases.

Results We demonstrate the snapshot method with an experiment performed in the following way. We apply the pump and repump light with a power of $6 \mu\text{W}$ and $100 \mu\text{W}$ respectively for about 5 ms to initialize the atoms. After a variable delay t_{wait} a switch opens the RF excitation at around 1.4 MHz for $25 \mu\text{s}$. The short duration of the RF excitation ensures that its spectral width is much broader than the splitting of the Larmor frequencies at around 1.4 MHz. Then the probe light is sent and the polarimetry signal recorded for a duration of 20 ms. This experiment was conducted without a cavity around the cell to simplify the analysis. The probe power was low enough that probe-induced decoherence can be neglected, and the probe frequency was tuned to about 3 GHz red from the 3-3' transition. This detuning was chosen to have sufficient signal from both manifolds.

The resulting PMORS signal is shown in 4.10. The data points are connected by lines to guide the eye. The signal above 1.4158 MHz, that is right of the dotted line, has been multiplied by 10 for better visibility. The peaks on the left stem from the F=4, the peaks on the right from the F=3 manifold. For a minimal waiting time of $44 \mu\text{s}$, we see a strong signal from a well-polarized F=4 manifold, and no signal from population in F=3. As the waiting time is increased, the signal from F=4 reduces while the signal from F=3 first grows, before it also reduces.

We fit the datasets for each t_{wait} with the PMORS function including an added background offset. An example of dataset and fit is shown in fig 4.11. The data points are averaged from eight sets of data with 10000 averages each. The errorbars represent the standard deviation of the sample mean obtained from these 8 datasets. We note that the fit function does not completely agree with the data for the shape of the very small peaks. However, we expect these small peaks to represent a minor contribution to the atomic population which renders

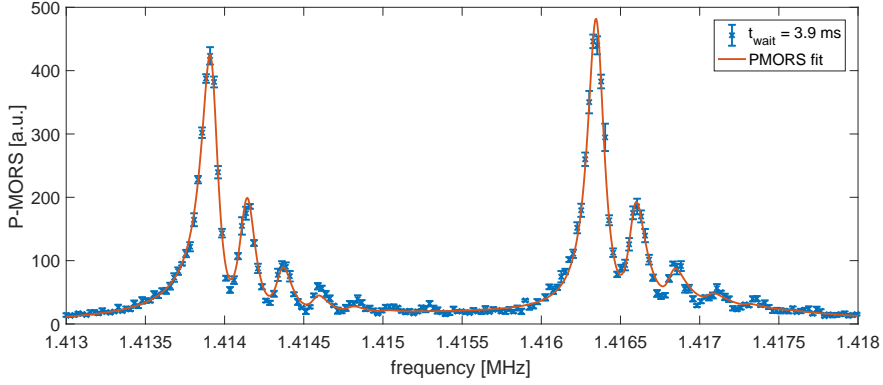


Figure 4.11: PMORS spectrum for 3.9ms waiting time. Respective fit of PMORS function with offset is shown

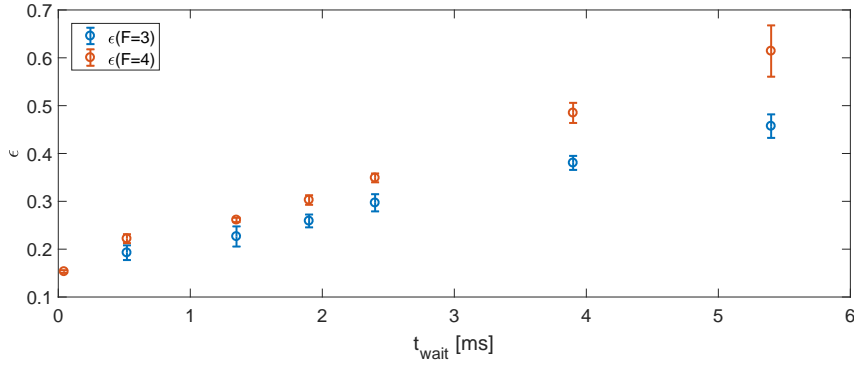


Figure 4.12: Fitted parameter ϵ for each manifold versus waiting time.

the disagreement negligible. Furthermore, we emphasize that we achieve this good agreement by only using a single parameter for each manifold to describe the relative peak heights. We observe that this parameter ϵ changes over time as shown in fig. 4.12.

We note that we obtain a linewidth of $\Gamma = 122 \pm 5$ Hz for minimal waiting time, corresponding to a coherence time $T_2 = 2.5$ ms. After a few ms waiting time and thus considerable spread of the atomic population we only have an insignificant increase to $\Gamma = 129 \pm 5$ Hz. This is a strong hint that spin exchange collisions are not the main limitation for the coherence time under the conditions of this experiment.

With the pulsed MORS we are able to measure the population differences of neighbouring Zeeman levels. In order to determine the population fraction in each level we need to make additional assumptions. We assume that the pumping works so well that we have a negligible population fraction for minimal waiting time in the depumped extreme states $|F, m_F\rangle = |4, -4\rangle$ and $|F, m_F\rangle = |3, -3\rangle$. This is strongly confirmed by the observed MORS signal.

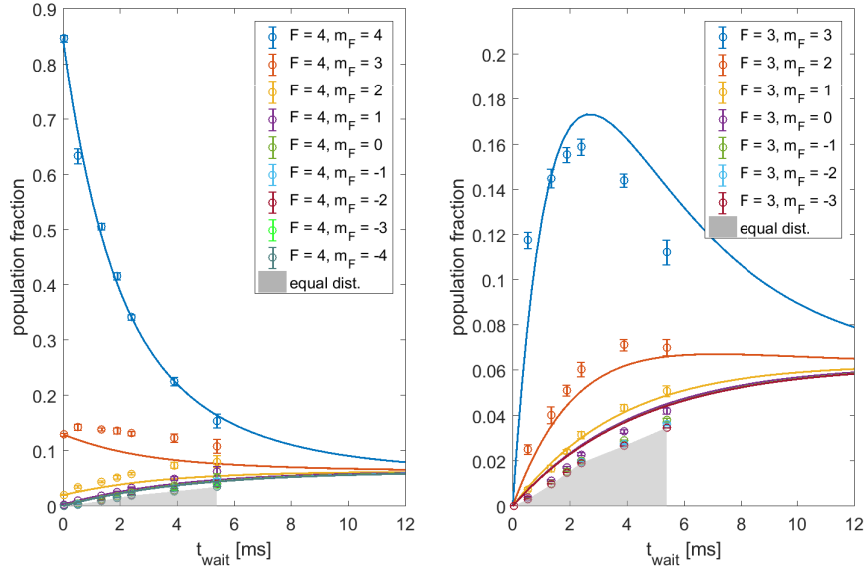


Figure 4.13: Atomic population fractions plotted versus waiting time for $F=4$ (left) and $F=3$ (right). The data points are fit results from the PMORS fits. The error bars represent the standard deviation from four to nine independent measurements, each with 10000 averages. The solid lines show the fitted model. The grey part is the expected equal distribution calculated from the data.

Since the populations are changing this assumption is not valid for longer waiting times. For increased waiting times we observe an overall decrease of the signal which can be explained by the build-up of atomic population distributed equally among the Zeeman levels of a hyperfine manifold. We assume that this is mainly an effect of complete randomization of the atomic state when colliding with the wall. The assumption of a complete randomization process has been applied successfully previously [GKR⁺05]. The assumption implies that the atoms are distributed equally among all Zeeman levels of both hyperfine manifolds.

We can then determine the fraction of population in each level. This is shown for different waiting times in fig. 4.13, on the left for $F=4$, on the right for $F=3$. The grey area is the fraction of equally distributed atoms calculated from signal reduction. As expected, we observe a decrease of population in $|4,4\rangle$, as the atoms distribute into the other levels. The level $|3,3\rangle$ shows a rapid increase in atomic population before decaying to the long-time level of equal distribution. We note that the population in $|3,3\rangle$ even outnumbers the population in $|4,3\rangle$ after a few ms. Furthermore, we see that we start out with about 85% of the atoms initialized in $|4,4\rangle$. This corresponds to an atomic polarization in $F=4$ of $p = \sum_{F=4,m} m\rho_{m,m}/4 = 0.955$. Further, tedious adjustment of the pumping light polarization probably would have increased this number to the typically achieved $p = 0.98$ if required.

Modelling We now present a simple rate equation model, including only two parameters, explaining the observed evolution of the atomic population. A model that bases only on complete randomization of the state after a certain number of wall bounces fails to explain the initial increase and then decay of e.g. $N_{3,3}$. Inspired by [GKR⁺05] we assume a model that has a rate for total randomization Γ_r , and a rate for electron flips Γ_e . We then use the rate equations to get a system of 16 differential equations. We have e.g.

$$\dot{N}_{4,3} = -\Gamma_e N_{4,3} - \Gamma_r N_{4,3} + \sum_{i \neq 4,3} \frac{1}{15} \Gamma_r N_i + \left(\frac{1}{8} \Gamma_e N_{4,4} + \frac{7}{32} \Gamma_e N_{4,2} + \frac{21}{32} \Gamma_e N_{3,2} \right) \quad (4.13)$$

where the prefactors of the term in brackets are the modulus square of the product of the two Clebsch-Gordans involved. These Clebsch-Gordans come from our model of electron spin randomization. We start in a level $|F, m_F\rangle$. This level can be written in the basis of spins of nucleus and electron with corresponding projections $|j_1, m_1, j_2, m_2\rangle$

$$|F, m_F, j_1, j_2\rangle = \sum_{m_1 m_2} |j_1, m_1, j_2, m_2\rangle \langle j_1, m_1, j_2, m_2 | F, m_F, j_1, j_2\rangle \quad (4.14)$$

$$= \sum_{m_1 m_2} |j_1, m_1, j_2, m_2\rangle C_{F, m_F}^{m_1, m_2} \quad (4.15)$$

In the case of caesium the nuclear spin is fixed to be $j_1 = 7/2$ and the electron spin is $j_2 = 1/2$. We have included it here for completeness. We can think of the electron randomization process as an operator that randomizes the orientation of the electron spin, i.e. m_2 . In our case of $j_2 = 1/2$ this operator can only flip m_2 or not flip m_2 . We define an operator O_{esflip} that will flip the spin $m_2 \rightarrow -m_2$. Finally, we have to write the new state in the $|F, m_F\rangle$ basis. In total we have

$$O_{esflip} |F, m_F\rangle = \sum_{m_1, m_2} C_{F, m_F}^{m_1, m_2} \sum_{F', m'_F} C_{F', m'_F}^{m_1, -m_2} |F', m'_F, j_1, j_2\rangle \quad (4.16)$$

If we are interested in the probability w to transfer from one state to the other we have

$$w(|F, m_F\rangle \rightarrow |F', m'_F\rangle) = |\langle F, m_F | O_{esflip} | F', m'_F \rangle|^2 \quad (4.17)$$

which leads to the fact that we need the modulus squared of the product of the Clebsch-Gordans involved.

We fit the resulting system of coupled differential equations to the population fractions. This yields the best fit parameters $\Gamma_e = 240 \pm 10$ Hz and $\Gamma_r = 214 \pm 8$ Hz, which gives the solid lines in fig. 4.13. Comparing the fitted model to the data, we observe that there is very good agreement with the decay of the population in $|4, 4\rangle$. The model also captures well the overall shape of the initial increase and later decrease of the population evolution in $|3, 3\rangle$. We note

however, that the decay of the population in $|3,3\rangle$ appears faster in the measured data than in the model, and the population evolution of $|4,3\rangle$ is not well captured by the model. We have used a few assumptions to calculate the population. The assumption that the fraction of equal population is not only equally distributed within one hyperfine manifold, but at all times between all sixteen levels, may have distorted our population distribution. However, it is not obvious, how a shift of the equal distributions, that is the grey areas in fig. 4.13, will improve the agreement between the data and the model. It is possible, that a small contribution from spin-exchange collisions has already significant impact on the details of the population evolution. One could, similar to [GKR⁺05], use a measurement of the decay of the Faraday angle to derive the rates of electron-randomization, complete randomization and spin-exchange collisions, and compare these results with the presented data. Even though this will be helpful to support our claims, we refrain from continuing this investigation here.

Conclusion of snapshot pulsed MORS We have in this section demonstrated a novel method that allows to easily access and track atomic distributions of an initially pumped atomic ensemble over time. We have presented a simple model explaining the evolution of atomic distribution.

For us with respect to the DLCZ-type experiment, we note that storing in $|3,3\rangle$ will lead to much more extra scattering. In the ideal case of perfect initial pumping we can use the prediction of the model to estimate the atomic population. This is shown in fig. 4.14. We note that already after 1.2 ms, which is in this case similar to half the coherence time T_2 , we have about 15% of the atoms in the state $|3,3\rangle$. Assuming similar filtering, the reasoning of [BZP⁺16] leads to a probability to read out a photon from an asymmetric collective excitation equal to the fraction of population in the storage state. This clearly favours choosing $|4,3\rangle$ as a storage state over $|3,3\rangle$.

4.6 Microwave spectroscopy

In this section we present the results of a preparatory experiment, characterizing the coherence time on the hyperfine transition. The storage time of a collective excitation is closely connected to the coherence time of the respective atomic transition. In order to estimate the performance of this storage we used a microwave spectroscopy measurement as shown in fig. 4.15, similar to [BHK⁺05]. Probe light on-resonant with the D₂ line is sent through the cell. The cell is in a magnetic field that splits the Zeeman levels. A microwave is sent on the cell and drives hyperfine transitions. The microwave frequency is scanned across all Zeeman transitions, while the probe transmission is detected with a photodiode. The Doppler broadening for the probe (> 200 MHz) leaves the excited state hyperfine splitting unresolved, while for the microwave the

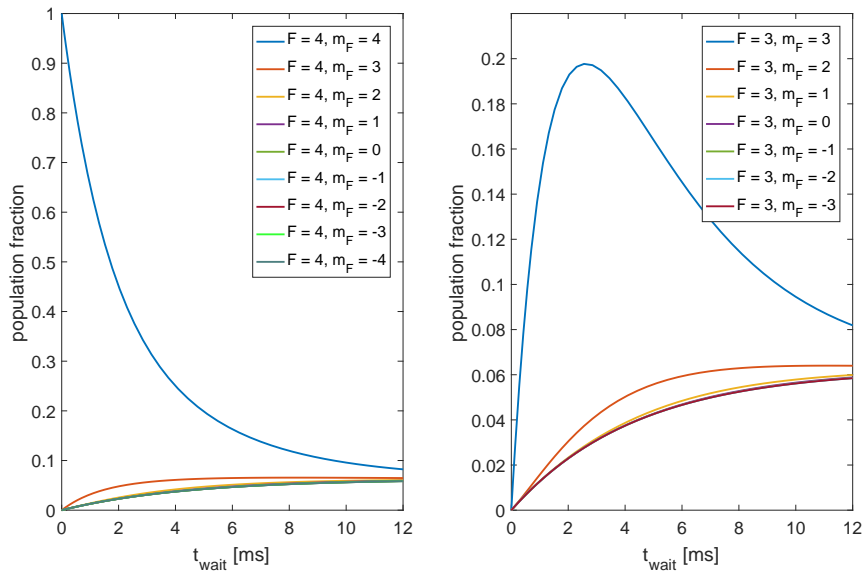


Figure 4.14: Atomic population fractions plotted versus waiting time for $F=4$ (left) and $F=3$ (right). The solid lines show the model predictions for perfect state initialization.

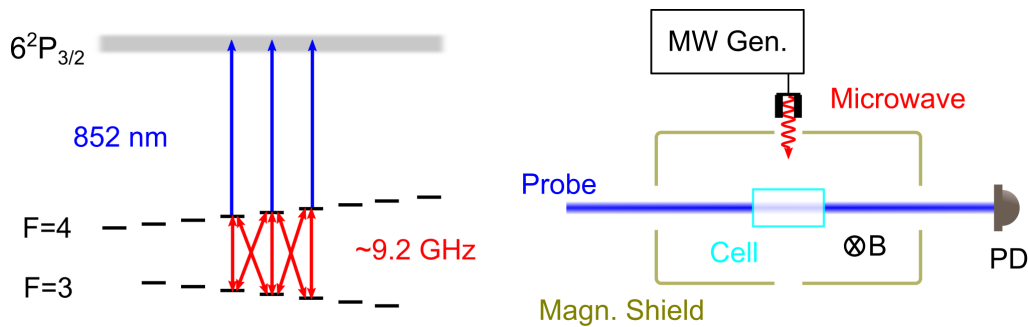


Figure 4.15: Microwave spectroscopy level scheme (left) and set-up (right). Shown are all ground state Zeeman sub-levels, the unresolved excited states are indicated by the grey box. The microwave transitions (red) and the probe light (blue), are only shown coupling a few Zeeman states as example. The microwave from a microwave generator (MW Gen.) is sent through a microwave antenna on the cell residing in a magnetic field (B) inside a magnetic shield. The probe transmission is detected with a photodiode (PD).

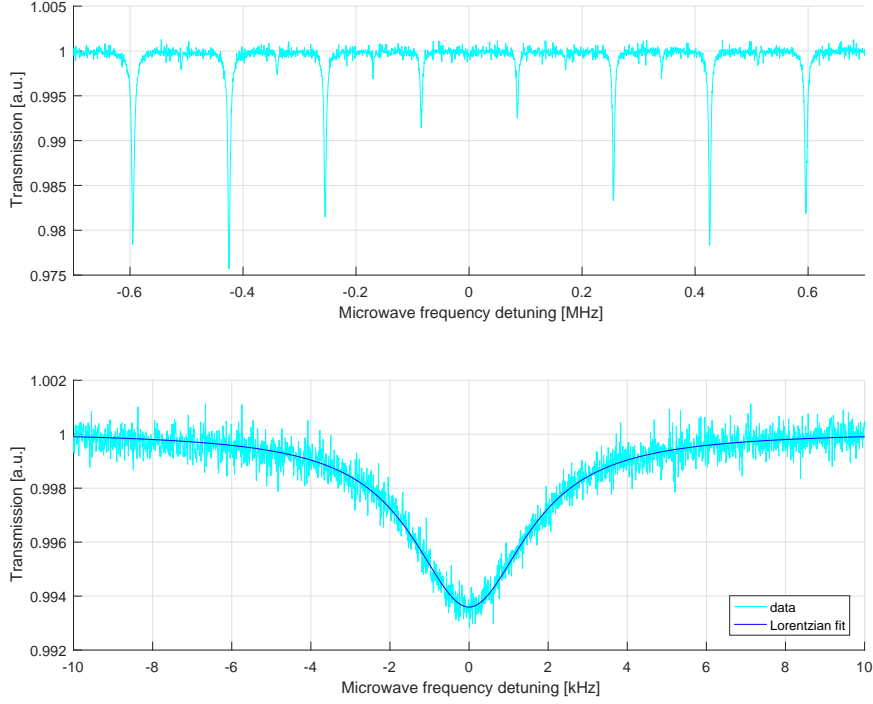


Figure 4.16: Microwave spectroscopy. Top: spectroscopy signal of all ground states, 110 averages with 20 seconds sweep duration, bottom: spectroscopy of 0-1 transition, 50 averages with 2 seconds sweep duration. In top and bottom the zero reference of the frequency-axis was centred on the 0-0 and 0-1 resonance respectively, the probe power was $4 \mu\text{W}$ and the microwave power -4 dBm .

Doppler broadening is only around 10 kHz, much less than the typical Zeeman splitting. We performed spectroscopy measurements on four different cells. We were of course mostly interested in the micro-cell performance, however we also measured on bigger cells with longer coherence times to exclude limitations due to technical issues like microwave frequency noise, inhomogeneous magnetic fields etc. In total, we measured one standard micro-cell (length 10mm, cross section 0.3 mm x 0.3 mm), two 5 mm-sized cubic cells and one even bigger cylindrical cell (length 20 mm, diameter 12.7 mm). Although microwave antenna positioning, magnetic fields and data acquisition were different, the measurement procedure was similar. As a typical example we show the results from the cubic cell cA2 in the following figures of this section. In fig. 4.16 we show the microwave absorption spectrum. In the upper part we observe 8 main dips, corresponding to the sigma transitions between the ground states. The Larmor frequency of 86 kHz leads to a quadratic Zeeman splitting that is much smaller than the linewidth, thus the transitions $|3, m_F\rangle - |4, m_F + 1\rangle$ and $|3, m_F + 1\rangle - |4, m_F\rangle$ are unresolved and will be referred to as $m_F - m_F + 1$. Due to the microwave polarization the dips from the π transitions are only barely

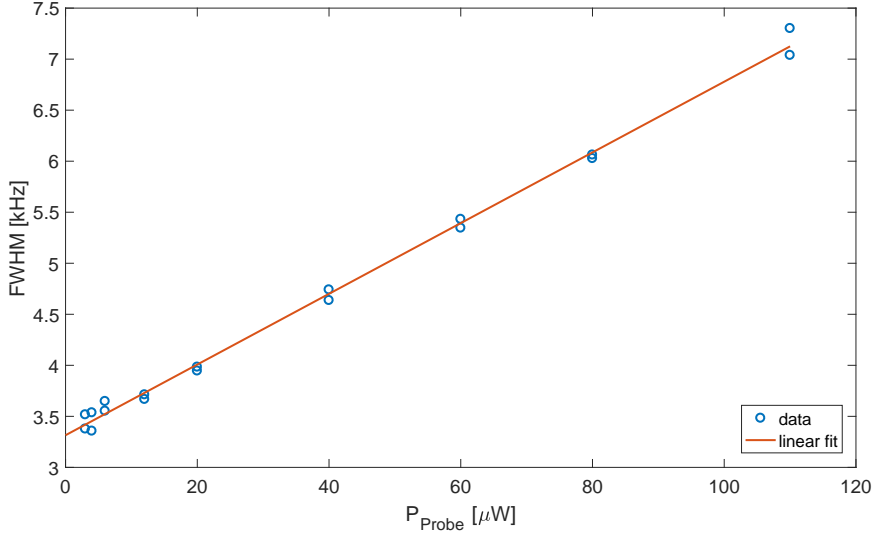


Figure 4.17: FWHM from the fit result of the microwave spectroscopy of the 0-1 transition measured for different probe powers. Linear fit with extrapolation to zero probe power. The microwave power was -4 dBm.

visible above the noise in the middle between the main dips. The bottom part shows a sweep across the 0-1 transition and the according fit with a Lorentzian subtracted from an offset. From the fit result for the width we can calculate the coherence time T_2 of the respective hyperfine transition. We measure the width for different probe powers and microwave powers and extrapolate the results to zero power. The probe power scan in figure 4.17 can be well approximated linearly. We then performed a microwave power scan shown in figure 4.18. Here the microwave power $P_{\text{microwave}}$ is the output power of the microwave generator. Although the power dependence of the width appears to be nonlinear for high powers, it allows a linear approximation for low powers. The extrapolation to zero microwave power and zero probe power yields a FWHM of $\Delta\nu_{hf,cA2} = 2.2(1)$ kHz.

The results of the spectroscopy measurements are listed in the following table:

cell	shape	coating	$\Delta\nu_{hf}$ [kHz]	$T_{2,hf}$ [ms]	$T_{2,Zm}$ [ms]	trans	shield
L1	cyl.	Alkene	0.8(1)	0.40(5)	53	0-0	no
cA3	cubic	Paraffin	3.4(1)	0.094(3)	15	0-0	no
cA2	cubic	Paraffin	2.2(2)	0.14(1)	9	0-0	no
			2.2(1)	0.14(1)		0-1	yes
H2	micro	Paraffin	15(2)	0.021(3)	2	3-4	yes

where we use the abbreviations $\Delta\nu_{hf}$ for the FWHM of the microwave spectroscopy signal extrapolated to zero power, $T_{2,hf}$ for the corresponding coherence time in ms, and $T_{2,Zm}$ for the coherence time of the Zeeman transition

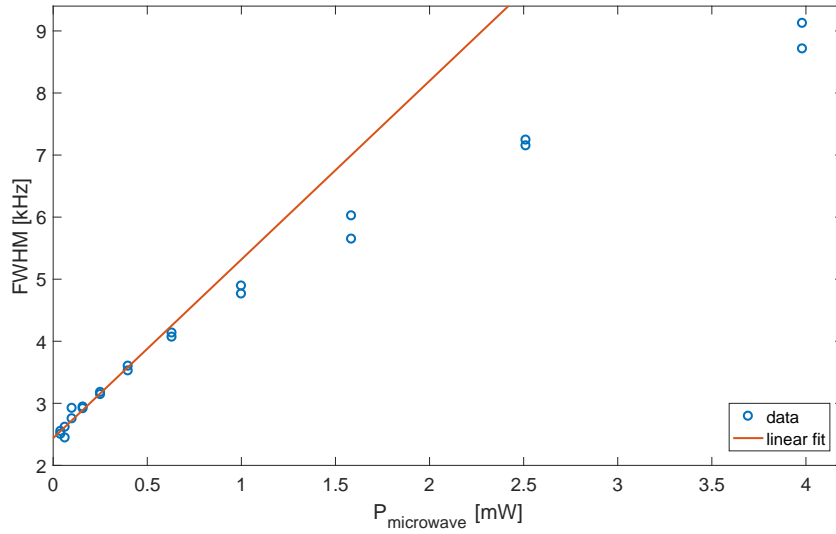


Figure 4.18: FWHM from the fit result of the microwave spectroscopy of the 0-1 transition measured for different microwave powers. Linear fit to the values below $P_{\text{microwave}} < 0.5$ mW with extrapolation to zero microwave power. The probe power was $4 \mu\text{W}$.

in ms. The column called trans specifies the microwave transition $m-m+1$ and the last column lists whether magnetic shielding was used or not for the microwave absorption measurements. The Zeeman T_2 times were determined from continuous MORS measurements using magnetic shielding.

We should briefly explain why we measured on different microwave transitions. We were obviously most interested in the coherence time of the 3-4 transition since this is the transition used in the DLCZ-type experiment. However we did not see a significant difference in linewidth for the different transitions. As shown in figure 4.16 the microwave antenna setup with the magnetic shield led to good absorption signals on the sigma transitions. Without the shield we set the microwave polarization such that we got a good signal to noise ratio on the magnetically insensitive 0-0 transition to minimize the influence of possible magnetic field inhomogeneities.

4.6.1 Discussion of microwave spectroscopy results

We have observed hyperfine coherence times well below 1 ms. Apart from the question, if such a cell will be suitable for a DLCZ-type experiment, we can also ask for the reason of these low coherence times. As we have seen in section 4.2, the coherence time on the Zeeman transition may vary a lot from cell to cell. We thus expect similar behaviour for the hyperfine coherence times. However, if the anti-relaxation coating determines both coherence times, we might assume a constant ratio.

If the coherence time is dominated by electron spin randomization during wall collisions, we expect up to seven times shorter coherence time on the hyperfine transition (see also eq. 4.13). For complete spin randomization dominating the ratio should be one. Previous results from other groups have reported up to one order of magnitude larger coherence times on the Zeeman transition, confirming that the electron spin randomization dominates. [BHK⁺05] [CKBB13]

We measure however a much larger ratio of about 60 . . . 160 between the Zeeman and the hyperfine coherence time.

As presented above, we have taken different measurements with different cells. We can use these to check various possible contributions to the decoherence rate and we will discuss these qualitatively in the following.

One expects that the hyperfine transition is more sensitive to magnetic field fluctuations than the Zeeman transition by a factor $7 \cdot \nu_Z$ for the 3-4 hyperfine transition. On the other hand, the 0-0 transition should be insensitive to magnetic field fluctuations. We have measured similar widths for both of them.

Technical limitations as frequency noise from the microwave or electronic noise in the detection are excluded for the microcell and the cubic cell by the measurement of even narrower linewidths for the bigger cylindrical cell.

Magnetic field inhomogeneities that do not average out completely due to slow diffusion of the atoms should have bigger linewidth contribution for bigger cells. Probe, microwave and RF power broadening are excluded by extrapolation to zero power.

If atoms at different positions in the cell are subject to different microwave and RF phase, then atomic motion washes out this phase and can lead to broadening. [FVC83] This plays a role when the wavelength is comparable to the cell size. For the Zeeman transition the wavelength is more than hundreds of meters, for the hyperfine transition it is only 3 cm. If the phase has any influence, we should get more sensitive to such inhomogeneity for bigger cells. Furthermore we have measured with and without shield which might act as a microwave cavity, and with different microwave antenna placements. Thus it is unlikely that this effect is leading to the increased hyperfine to Zeeman ratio we observe.

The reservoir effect, that is atoms leaving the cell into the stem where they can rapidly decohere by collisions with solid caesium droplets on the cell walls, should have similar contributions to Zeeman and hyperfine decoherence.

4.6.2 Conclusion of microwave spectroscopy

In our current setup, the coherence time on the hyperfine transition is about 100 times shorter than on the Zeeman transition. This leaves us with a coherence time that is only slightly bigger than the time required for motional averaging

in the DLCZ-type experiment. Thus, hyperfine storage does not provide a practical solution for us.

We do not know the reason for the short hyperfine coherence time and further investigation will be necessary. We emphasize however, that even if we reach the factor of one order of magnitude between Zeeman and hyperfine coherence time, reported by other groups, we will reach a hyperfine coherence time of about 1 ms for the currently top-performing micro-cells. This will severely limit the maximum storage time in the DLCZ-type experiment.

DLCZ-type experiment

We present in this section an experiment where we create and read-out a collective atomic excitation, detecting the scattered photons. This is very similar to the fundamental step of the original idea presented in the DLCZ paper [DLCZ01]. The results presented here were measured mainly in two experimental runs. The first run focussed on measuring for minimal write-read delay with good statistics. The second run focussed on measuring for different write-read delays. This experiment was a collaborative work together with Boris Albrecht and Karsten Dideriksen. The results from this section have been partly published in [ZDS⁺18] and have also been partly presented in Karsten Dideriksen's thesis [Did17]. The analysis is divided in different parts, starting with power scaling and a spectral analysis. We then investigate the photon statistics via correlations and demonstrate a long lifetime of the collective excitation. Finally, we study the time dependency of the read photon.

During the experiment, the counts detected by the single photon counter are acquired with timestamps and can be plotted in a histogram. As an example, a typical set of data including 2400 sequences is shown in fig. 5.1. For better signal-to-noise ratio we have already folded all 56 repetitions of write, read and background detection windows, present in each sequence, onto each other. We observe a significant number of counts during the write and the read detection windows, whereas the background counts appear to be negligible. As an important test we perform an experiment with the same experimental parameters, however without sending any excitation light during the write window. This leads to less counts during the read (shown in gray). We conclude that only the difference of counts during the read between "with write" and "no write" can be attributed to excitations during the write.

In the following sections we will investigate in detail the various contributions to both write and read detection events. In fig. 5.1 we also show the beginning of the "check pulse". This is a 500 μs long, very weak pulse of light, resonant with the filter cavity and linearly polarized orthogonally to the excitation light.

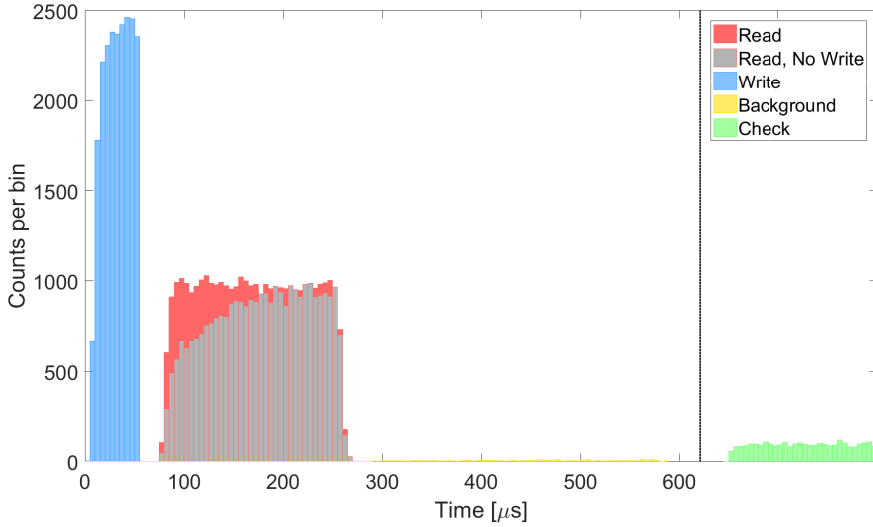


Figure 5.1: Histogram of counts during detection windows. Counts are shown for "with write", and during read window also for "no write" experiments. The experiments include about 2400 sequences with $P_{read} = 21 \mu\text{W}$ and "with write" $P_{write} = 32.2 \mu\text{W}$. For write, read and background all 56 repetitions are folded together. The beginning of the non-folded check pulse is shown for comparison on the right of the dotted line.

It is sent at the end of each sequence and allows us to determine the detection efficiency for each experiment individually.

5.1 Scaling with power

For characterization purposes we conducted the DLCZ experiment with different optical powers of the write and read pulses. We focus on the difference in read countrates with and without write pulse since this is the contribution attributed to the actual write process, and it is insensitive to common noise counts. We fit a simple exponential decay $f_i(t) = c_i \exp(-t/\tau)$ to the difference. We will motivate this procedure with equation 2.34 further below. The result is shown in fig. 5.2 where we plot against the first $100 \mu\text{s}$ of the read out pulse, which appears to be the time window that captures the complete read-out for the read power chosen for this plot. The data for different write powers, shown in different colors, is fitted simultaneously with common decay time, yielding $\tau = 25 \pm 4 \mu\text{s}$. The parameters c_i are plotted in the right plot versus the total write pulse energy¹ with respective colors. The plotted error bars are the 95% confidence intervals from the fit. The good agreement with a linear fit confirms that we are within a linear regime. From the spectral analysis, that will be presented in the next section, we can infer that we create about 0.6 symmetric collective excitations per pulse per nJ of write energy. Therefore, the

¹Write pulse energy and write and read powers are defined in front of the cell cavity.

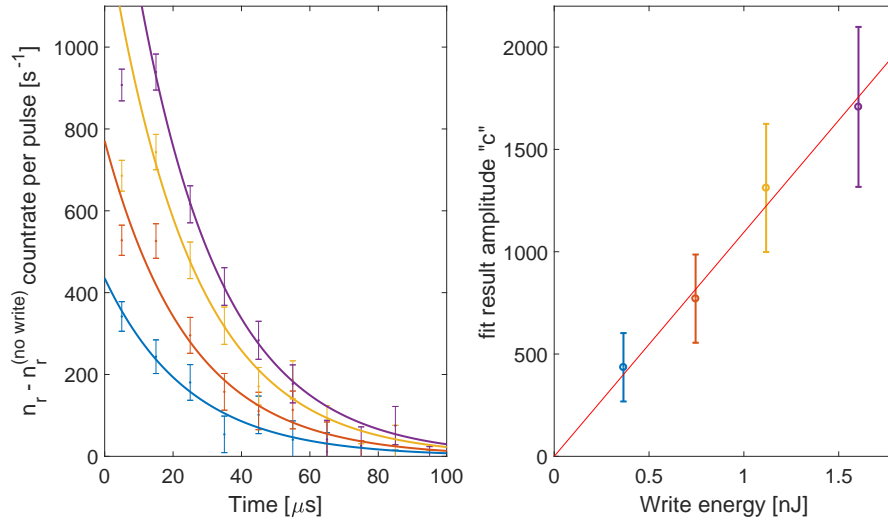


Figure 5.2: Left: Difference in count rate with and without write versus readout time. Plotted is the data (markers blue; red; yellow; purple corresponding to write pulse energy 0.4;0.7;1.1;1.6 nJ respectively) together with exponential fits (solid lines). The range of time for fitting only started after $20 \mu\text{s}$ to avoid the turn-on transient of the excitation pulse. The cell cavity input power during the read process was $39.5 \mu\text{W}$. Right: Fit parameter c versus energy of write pulse with corresponding colors and linear fit (solid line). Error bars show 95% confidence intervals.

data presented in fig. 5.2 includes up to about one stored symmetric collective excitation.

We repeat the same experiment with a similar analysis, but for various read excitation powers. For simplicity, we define the read power as the input power to the cell cavity. We plot the readout rate $r_{\text{read}} = 1/\tau$ in fig. 5.3 versus read power. The uncertainties on the readout rates are too large to faithfully extrapolate the decay rate in the dark. However, we expect that the decay rate in the dark is at least as high as the decay rate of the atomic population in the initial ground state. We therefore fit a line with fixed offset $1/T_1$ to the data. The agreement strongly hints at a linear scaling of the readout rate with read power in the range of interest. The data point from RF excited read out was added for reference and will be covered in section 6.1.

Although we phenomenologically chose a simple exponential decay function to describe the observed rates, we note that the exponential decay function used here can be derived from the four-wave mixing model function (eq. 2.34). We pull out the Rabi frequency Ω of the excitation field from the coupling and introduce the primed couplings via $\zeta = \zeta'\Omega$ and $\chi = \chi'\Omega$. Then a comparison shows that the observed linear dependence between readout power and

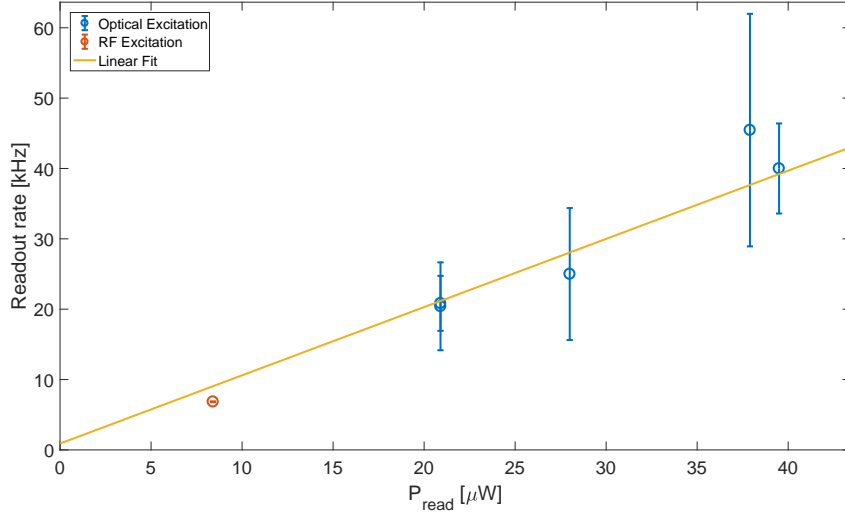


Figure 5.3: Readout rate versus read power. The blue (red) data was measured with optical (RF) write excitation. P_{read} is the read excitation input power to the cell cavity. The error bars represent 95% confidence levels. A line with fixed offset $1/T_1$ was fitted on the optical excitation data.

readout rate is predicted by this model via

$$\frac{1}{\tau} = -(\xi'^2 - \chi'^2)\Omega^2 \quad (5.1)$$

since the read out power is proportional to the square of the Rabi frequency Ω . An extra offset $1/T_1$ comes from approximating the atomic decay with $\chi^2 \propto N(t) \propto e^{-t/T_1}$. The amplitude of the exponential decay function can be identified in the model as

$$c_i = \eta\chi'^2\Omega^2 n_{ce}^{(i)} \quad (5.2)$$

where we have combined intrinsic readout, escape and detection efficiency in η . The model confirms the observed linear dependence between amplitude c and read out power. Furthermore, we expect the amplitude to be proportional to the number of collective excitations n_{ce} .

The results of this section allow us to scale the write excitation power according to an average number of desired collective excitations. Furthermore we can (in principle at least) choose the read power high enough to have efficient readout after a specific duration.

5.2 Spectrum of write and read fields

The necessity of narrow spectral filtering of the scattered photons (section 2.5) also gives the opportunity to spectrally analyse these using the filter cavities. The linewidth of the filter cavities is by design broader than the photons scat-

tered from the collective excitation. However, measuring the photons that are coupled out from the cell cavity at different filter cavity detunings allows us to identify the various contributions to these photons. By tuning the frequency of the lock light for the filter cavities we can detune the filter cavities from the write and read frequencies. Choosing a detuning close² to the write excitation frequency leads to a substantial write leakage, that is transmission of write excitation light through the spectral filters. This allows us to adjust the waveplates after the cell cavity to optimize polarization filtering for the write step. As explained in the method section, the polarization filtering cannot be optimized for the write and the read step simultaneously due to birefringence from the atoms. Since this birefringence depends on the optical pumping and the temperature, it turns out to be necessary to readjust the waveplates for polarization filtering on a daily basis. We optimized the polarization filtering for the write excitation instead of the read excitation since we then observed higher cross correlation $g_{w,r}^{(2)}$. This is expected (see section 2.8.1), since we detect higher additional noise contributions from other sources during the read process.

Fig. 5.4(a) shows the detected counts per pulse during the write process measured for different frequencies of the filter cavities. Here $\Delta_{FC} = 0$ corresponds to the filter cavities' resonance being one Larmor frequency above the write excitation frequency. Centered at this detuning, we observe a narrow contribution n_{ws} from the symmetric collective excitations above a broad background n_{wa} from asymmetric excitations. The leakage contribution n_{wl} is here negligible and the background counts n_{wb} (magenta circles), measured independently by not sending a write pulse, only give a minor, spectrally flat contribution. We fit the spectrum with a sum of these four contributions.

$$n_w(\Delta_{FC}) = \mathcal{L}_{FX}(\Delta_{FC}) + \mathcal{L}_{wa}(\Delta_{FC}) + \mathcal{L}_{FX}(\Delta_{FC} + \nu_L) + n_{wb} \quad (5.3)$$

We assume that the width of the scattered photon from the symmetric excitation follows the laser linewidth. The filter cavity is shaking relative to the laser (see section 3.4), resulting on average in an approximated Lorentzian \mathcal{L}' with 40% broader linewidth. We model the contribution from the symmetric excitations as $\mathcal{L}_{FX} = \mathcal{L}'\mathcal{L}_{XCav}$, where \mathcal{L}_{XCav} is the extra cavity Lorentzian with about 10 times broader linewidth. The broad contribution from asymmetric spinwaves is in equation 5.3 described by the second term \mathcal{L}_{wa} , a Lorentzian with an expected width 1.5 MHz according to 2.5. Even though it has negligible contribution we have included the third term $\mathcal{L}_{FX}(\Delta_{FC} + \nu_L)$, expressing the leakage contribution, here for completeness. It is shifted in frequency to be centred at the write excitation detuning. The amplitudes of the first three terms are the three free fit parameters. The resulting fit together with the individual

²The chosen detuning should allow for a compromise between reducing contributions other than leakage, and risking to overexpose the single photon counter with leakage, in our case about 1 MHz count rate.

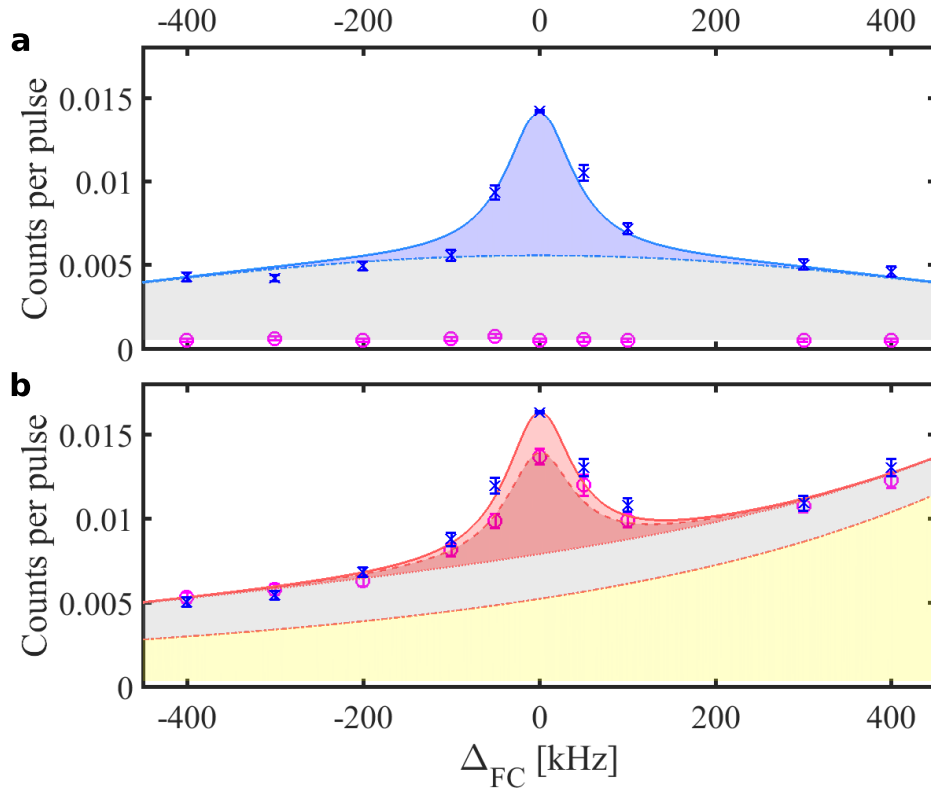


Figure 5.4: Detected counts per pulse versus detuning of the spectral filter resonance. Zero detuning is one Zeeman splitting above (below) the write (read) excitation frequency. Each point represents around 1000 experiments with 55 repetitions each. The points on resonance with the write pulse include 60 times as many experiments. **a** Heralding photon detection. **b** Photon detection in the readout, considering only the first $40 \mu\text{s}$. Blue crosses show data with write pulse present, magenta circles with write pulse off. The solid (dashed) lines show a fit with (without) write, containing scattered photons (blue, red), contribution from asymmetric excitations (grey), leakage (yellow) and background (unfilled), figure and caption published in [ZDS⁺18]

contributions is shown in fig. 5.4 (a).

Together with the cell cavity outcoupling efficiency of 62% and the detection efficiency of 9.6%, we can calculate the mean number of scattered photons $n_{ce} = 0.23$ per pulse. From the ratio of detected counts from symmetric collective excitations to the total detected counts from scattered photons we can deduce the write efficiency of $(63 \pm 1)\%$ at $\Delta_{FC} = 0$.

In fig. 5.4 (b) we show the corresponding spectrum for the detected counts during the first $40 \mu\text{s}$ of the read step. We will explain why we limit ourselves to this length of detection window in section 5.3. The narrow peak centred at zero detuning is expected to be related to symmetric collective excitations. Besides the broad feature from asymmetric collective excitations, we also observe a significant leakage contribution from the read excitation. This shows up asymmetrically in the figure since we only see the tail of the Lorentzian centred at $\Delta_{FC} = +\nu_L$. However, running the experiment without a write pulse, we still observe the narrow peak (magenta circles). We attribute this noise partly to a four-wave mixing process, where the read excitation simultaneously acts as a write pulse. Furthermore, excess scattering into the readout mode from imperfectly pumped atoms can contribute here. This will be discussed in section 5.5. The counts connected to the read out of the stored symmetric collective excitation are then the difference between the counts of the experiment with write pulse and the counts of the experiment without write pulse. The fit function for the read process is similar to the write process. However, the leakage Lorentzian is centred at $\Delta_{FC} = +\nu_L$. Here, we fit the data with write pulse and the data without write pulse with common fit parameters except for the peak height of the narrow contribution.

Estimating the linewidth of the narrowband scattered photons during write and read steps is not straightforward, since here we cannot distinguish the linewidth contributions from filter cavity shaking and from the photons themselves. However, from the broadening of the filter cavity linewidth we can give an upper bound of 26 kHz.

The write excitation also addresses the storage state and thus simultaneously reads out the created excitation. This four-wave mixing process causes the number of stored collective excitations at the end of the write pulse to be lower than the number of created photons. We can apply the four-wave mixing model to estimate the correct value

$$n_{ce} = \int_0^{t_{write}} \langle a_{RS}^+ a_{RS} \rangle dt - \int_0^{t_{write}} \langle a_{RA}^+ a_{RA} \rangle dt. \quad (5.4)$$

The first term is the number of photons created in the heralding mode, while the photons corresponding to the second term are the read out photons that are not detected since they are filtered out by the filter cavities. We can estimate the required coupling strength by setting the number of heralding photons

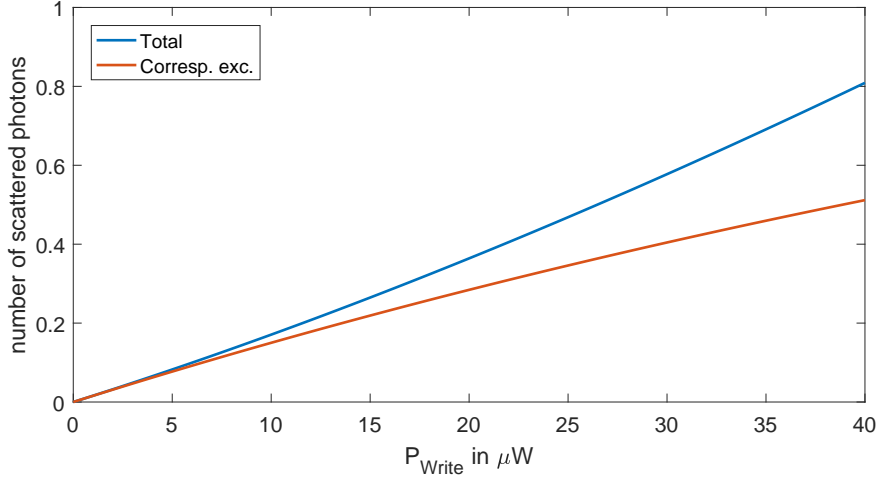


Figure 5.5: Expected power dependence of the total number of forward-scattered photons from symmetric collective excitations (blue) and number of stored symmetric collective excitations (red) after a $34 \mu\text{s}$ write pulse of constant power, using the four-wave mixing model.

obtained from the spectral analysis above equal to the first term. We further assume a fixed ratio of the coupling strengths $\chi_W/\zeta_W = 1.36 \cdot 0.96$ given by the Clebsch-Gordan coefficients and the respective cell cavity transmission. This yields in our case a coupling strength of $\zeta_W = 0.0216 \mu\text{s}^{-1/2} \cdot \sqrt{P[\mu\text{W}]}$. With this coupling strength we can calculate the corrected value of the number of collective excitations n_{ce} which is shown in fig. 5.5 for different write powers. For high write powers, there is a substantial relative difference between scattered photons and stored excitations. For the write power used for the filter cavity scan shown in fig. 5.4, the correction factor is 0.9, yielding 0.13 stored symmetric collective excitations. We note that the corrected number of excitations can be well approximated linearly, which is confirmed by the previous power scan in fig. 5.2.

5.3 Violation of Cauchy-Schwarz inequality

From fig. 5.4 we can see, that the typical count rates in our experiment are on the order of $0.02/40 \mu\text{s}$. Since this is several orders of magnitude lower than the maximum count rate of the single photon detector with a dead time of below 50 ns , we can well assume number-resolving detection. This allows us to investigate the auto-correlations and cross-correlation of the detected photons during write and read process. These correlation functions are calculated from the numbers of counts by $g_{ij}^{(2)} = \langle n_i(n_j - \delta_{ij}) \rangle / (\langle n_i \rangle \langle n_j \rangle)$ with $i, j \in w, r$ where n_w (n_r) is the number of detector counts during the write (read) process and we average over the experimental repetitions. From the correlation functions we

can in turn calculate the Cauchy-Schwarz parameter $R = (g_{w,r}^{(2)})^2 / (g_{w,w}^{(2)}g_{r,r}^{(2)})$.

We define the retrieval efficiency η_R as the difference between the average number of detected counts during the read conditioned on the detection of a write count in the same trial, and the unconditioned average number of detected counts during the read $\eta_R = \langle n_{r|w} \rangle - \langle n_r \rangle$.

In the experiment we send read excitation pulses with a duration of about $200 \mu\text{s}$. For the analysis of correlations, it can be advantageous to shorten the read detection window. During the read process, the stored collective excitation is read out, thus its contribution to the total output field decreases over time. However, the four-wave mixing contribution grows over time (see fig. 2.9 or section 5.5). Thus, we expect a better read-out to noise ratio at the beginning of the read pulse, which leads to better correlations between write and read detection events. We can in particular expect stronger violations of the Cauchy-Schwarz inequality at the beginning of the pulse. On the other hand the retrieval efficiency and the number of detected scattered photons grows when we increase the read duration. This leads to a lower relative uncertainty on the Cauchy-Schwarz parameter for a longer read detection window. To choose a good detection window, we plot both the retrieval efficiency η_R and the Cauchy-Schwarz parameter R in fig. 5.6 (a). For a length of the read detection window of $\tau_R = 40 \mu\text{s}$, we observe the best Cauchy-Schwarz parameter in terms of number of standard deviations above the non-classical boundary of 1. We therefore choose this detection window for the remainder of this and the next section. The corresponding retrieval efficiency of $\eta_R = (1.55 \pm 0.08)\%$ leads to an intrinsic retrieval efficiency of $\eta_R^i = (16.1 \pm 0.9)\%$ at the cell cavity output when accounting for the detection efficiency of $\eta_d = 9.6\%$. The resulting values for the Cauchy-Schwarz parameter and the correlation functions are

$$\begin{aligned} R &= 1.4 \pm 0.1 & (1.33) & \quad g_{w,r}^{(2)} = 1.97 \pm 0.05 & (1.77) \\ g_{w,w}^{(2)} &= 1.86 \pm 0.07 & (1.93) & \quad g_{r,r}^{(2)} = 1.45 \pm 0.05 & (1.23) \end{aligned} \quad (5.5)$$

where the numbers in parentheses are the outcomes of the model introduced in section 2.8.1. The main experimental conclusion is that we have $g_{w,r}^{(2)} < 2$, albeit we are within one standard deviation. We can thus not infer non-classical correlations between the output fields of write and read from this alone. However, using the auto-correlations, we can calculate the Cauchy-Schwarz parameter which is above 1 by four standard deviations. This allows us to claim non-classically correlated write and read output fields.

The write autocorrelation fits well with the model, assuming a thermal state with a small Poissonian contribution from background counts. The read autocorrelation is much lower than for a single thermal state. Modelling the read counts as presented previously in section 2.8.1, that is readout of the stored collective excitation plus noise terms as following: a Poissonian state for leak-

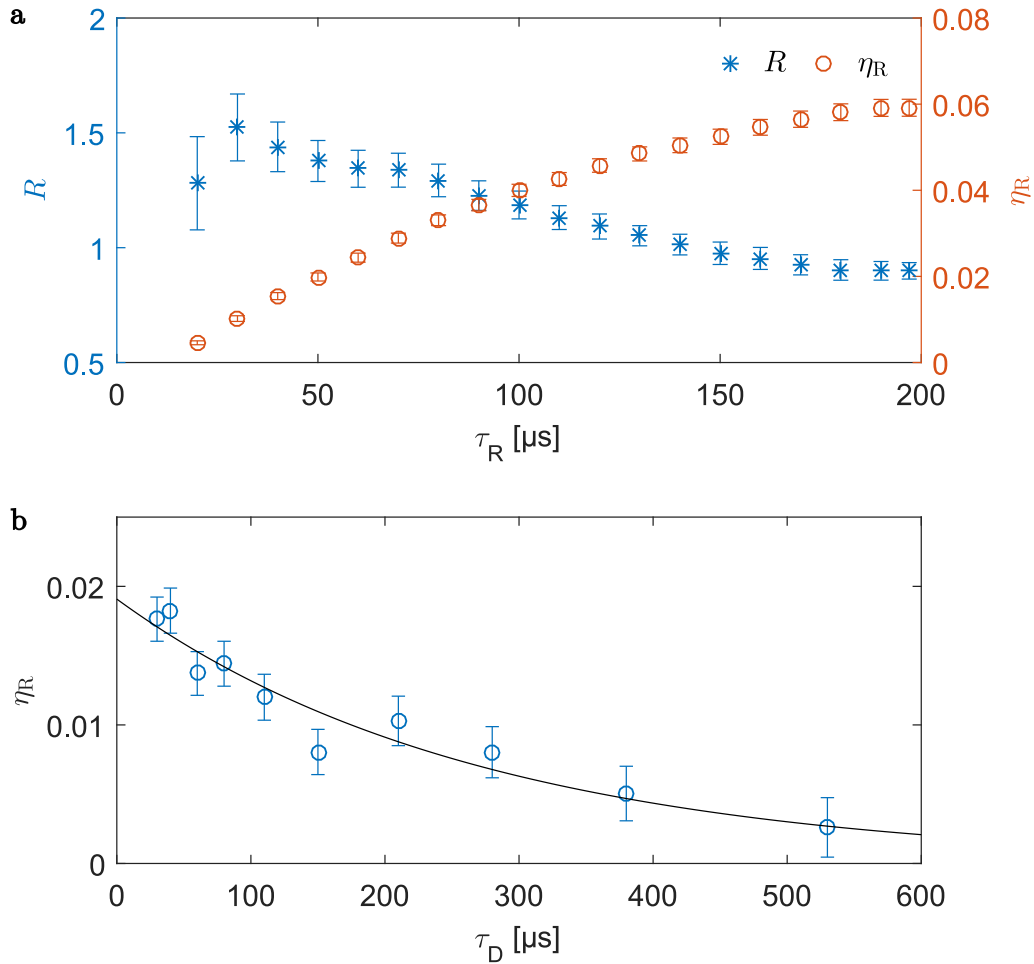


Figure 5.6: **a** Cauchy-Schwarz parameter (blue asterisks, left axis) and retrieval efficiency (red circles, right axis) versus the read detection window duration τ_R . The write-read delay time was $\tau_D = 30 \mu\text{s}$. **b** Retrieval efficiency (blue circles) versus delay time τ_D between write and read pulse. The exponential fit (black solid line) yields a characteristic decay time of $\tau = (0.27 \pm 0.04) \text{ms}$. The read detection window was chosen to be $\tau_R = 40 \mu\text{s}$. The two subfigures are from different datasets, hence the points at $\tau_D = 30 \mu\text{s}$ and $\tau_R = 40 \mu\text{s}$ do not overlap. The top graph dataset corresponds to $\Delta_{FC} = 0$ in fig. 5.4. This Figure has been published in [ZDS⁺18].

age and background, a thermal state for the four-wave mixing contribution and another uncorrelated thermal state for the broad- and narrow-band noise (the contribution of narrowband noise will be determined in section 5.5). This underestimates the autocorrelation $g_{r,r}^{(2)}$ which suggests that it might be incorrect to add these processes as uncorrelated contributions, similar to the findings of [MCS⁺15]. The same reason might lead to the observed underestimation of the cross-correlation by the model. Since we underestimate the read autocorrelation and the cross-correlation by approximately the same fraction, the modelled Cauchy-Schwarz parameter agrees with the observed value to within one standard deviation. For completeness we also state the expected value for the ideal, noise-free model of equation 2.51. Here we would expect³ a cross-correlation of $g_{w,r}^{(2)} = 1 + 1/p_0 \approx 6$.

It should be noted, that we cannot claim that we have a single photon state in the read process. The read autocorrelation conditioned on a write click is $g_{rr|w}^{(2)} = 1.3 \pm 0.2$. This is not below one, as for a non-classical state. On the contrary we see bunching of the photons. We attribute this to the big fraction of excess noise, that appears to follow thermal distributions.

We note, that we observe an increased cross-correlation of $g_{w,r}^{(2)} = 2.08 \pm 0.07 > 2$ by choosing only the last $20 \mu\text{s}$ of the write pulse for the write detection window. The reduced statistics does however not allow us to apply this analysis to all our data. The increased cross-correlation value could simply come from the shorter average delay time between the heralding event and the readout. We will investigate this delay time dependency in the next section.

5.3.1 Error estimation on correlation values

We apply a bootstrapping technique to estimate the uncertainty on the correlation function values and the Cauchy-Schwarz parameter. From the original set of n_e experimental trials we sample and replace random trials until we have a new set of n_e trials. We calculate the correlation function values and the Cauchy-Schwarz parameter on this random subset. We repeat this procedure at least 1000 times, sampling every time from the original set. This yields normally-distributed values. We quote the standard deviation of these values as the error estimate on the correlation function values and the Cauchy-Schwarz parameter.

5.4 Spinwave decay

In this section we present the results of an experimental run where we changed the delay time τ_D between the write and the read process. We show the values

³Here we take the average number of created collective excitations of $\bar{n} = 0.23$ which yields $p_0 = \bar{n}/(\bar{n} + 1) \approx 0.19$.

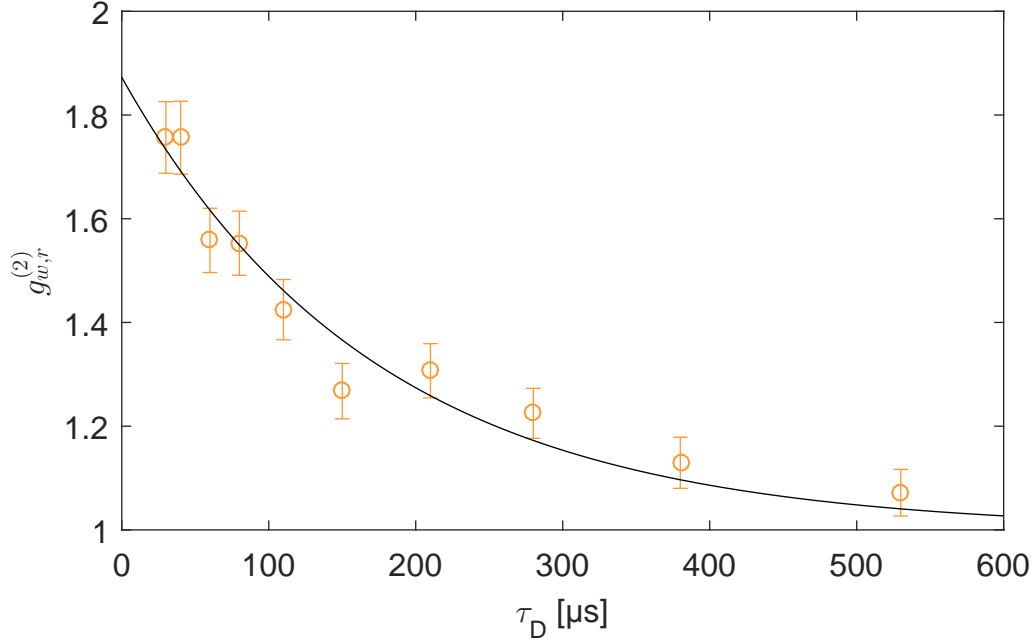


Figure 5.7: Cross-correlation between write and read detection events versus delay time. The solid line is a fit with the function $g_{WR}^{(2)} = 1 + Ce^{-\tau_D/\tau_g}$ which yields the decay constant $\tau_g = (0.17 \pm 0.02)$ ms. This figure has been published in [ZDS⁺18]

of the cross-correlation $g_{WR}^{(2)}$ versus τ_D in fig.5.7. We observe a decay of the cross-correlation which is in good agreement with a fit of an exponential decay which for long delay times goes to $g_{WR}^{(2)} \rightarrow 1$. This asymptotic behaviour is expected since after a very long waiting time the stored collective excitation will have decohered and the read counts will be independent of the write counts. The fitted decay time is $\tau_g = (0.17 \pm 0.02)$ ms.

We can also observe a decay over delay time in the Cauchy-Schwarz parameter shown in fig.5.8. In the ideal case we expect the Cauchy-Schwarz parameter to decay twice as fast as the cross-correlation, since $R \propto (g_{WR}^{(2)})^2$. However, we refrain from fitting an exponential here, since the asymptotic value, which depends on the auto-correlations of the write and read fields, is not obvious in fig.5.8. We note however, that we measure a non-classical Cauchy-Schwarz parameter until $\tau_D \approx 80 \mu\text{s}$.

The decay time of the cross correlation or the Cauchy-Schwarz parameter could be used as an estimate for the lifetime of the collective excitation. However, these values are influenced by τ_D -dependent noise. We have seen in section 4.4 that the leakage contribution depends on the time that has passed since the pumping has stopped. Thus, the leakage contribution will change with τ_D .

A better indicator for the decay time of the collective excitation is the decay of the retrieval efficiency which we defined above as the difference between the number of average read counts conditioned on a write click and the uncondi-

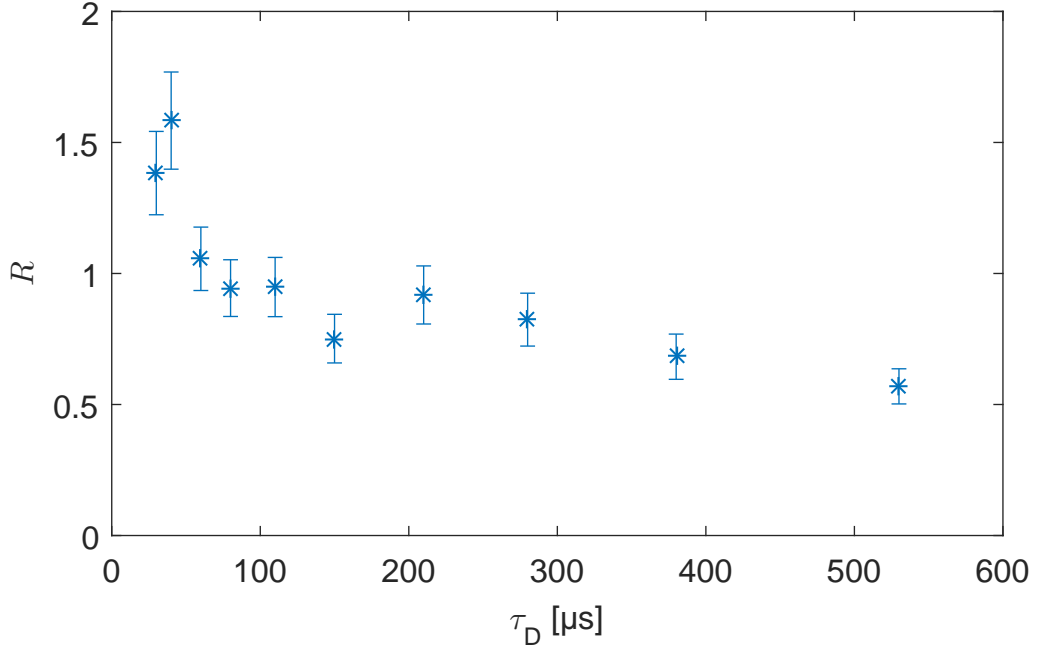


Figure 5.8: Cauchy-Schwarz parameter versus write-read delay. The read detection window duration was $\tau_R = 40 \mu\text{s}$. This figure has been published in [ZDS⁺18]

tional average number of read clicks $\eta_R = \langle n_{r|w} \rangle - \langle n_r \rangle$. It is a better indicator, since it does not depend on uncorrelated noise that changes with τ_D , e.g. leakage noise. In fig. 5.6(b) we plot the retrieval efficiency versus the delay time τ_D . We observe good agreement when fitting with an exponential decay and we extract the $1/e$ collective excitation lifetime $\tau_{CE} = (0.27 \pm 0.04)$.

5.5 Time evolution of pulses

In order to identify the contributions to the read-out photons we investigate the temporal shape of the counts detected during the read process. In the first section we have mainly focused on the difference between read counts when there was a write compared to when there was no write. Now we will consider the total number of detected read counts. Two examples, one for similar powers as for the previous sections, and one for high write and read power are shown in fig. 5.9 on the left and right, respectively. The red bars show the counts with write, the unfilled bars show the counts without write. First, we perform the spectral analysis presented in section 5.2 on the corresponding filter cavity scans for different time slices during the read pulse, excluding the regions where the pulse is switched on and off. From the resulting fits we can extract the leakage and the broad contribution. The leakage contribution changes linearly over the read time, while the broad background stays approximately constant. The extrapolated contributions are shown as overlay areas in fig. 5.9. The contribution for the high power example is smaller relative to the

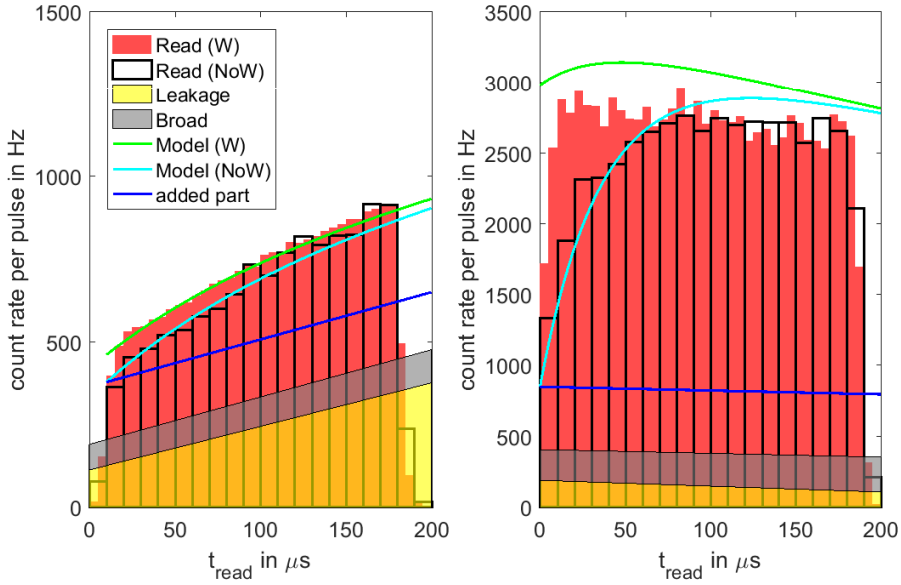


Figure 5.9: Photon shapes versus time. Left (right) for low (high) write and read power. Red bars show counts when the write pulse had been present, unfilled bars when not. The yellow and gray overlay are respectively leakage and broad contributions, estimated from corresponding filter cavity scans. Green (cyan) line shows the model with (without) previous write above an added part (blue) that is constant over time. Write power $7.1 \mu\text{W}$ ($32 \mu\text{W}$), read power $8.6 \mu\text{W}$ ($39 \mu\text{W}$) on the left (right).

total counts, since here the polarization filtering had been optimized for the read pulse.

We now use the four-wave mixing model together with the previously estimated coupling strength and the number of collective excitations derived from the filter cavity scans. We assume constant read power during the pulse and account for the different average cell cavity detuning for each light field, for atomic state decay and for outcoupling and detection efficiencies. The resulting model underestimates the count rate significantly. This suggests that there is an extra contribution that we have to consider. We choose this extra contribution (shown as the blue line) constant over time, such that for the low power case the cyan and the green lines, representing the model contributions for readout and four-wave mixing respectively, agree well with the data. As starting time for the model we choose the half-rise time of the respective read excitation pulse. We note, that for the high power case a similar ratio of extra part and broad contribution seems to be a good choice, leading to good agreement of the model and the data without write - at least for the first part of the pulse. For the data with write, the read out appears less efficient as the model prediction. For later times during the pulse, the model also overestimates the counts. We emphasize, that the extra contribution is at this point only a guess based on these two datasets. We note however, that the ratio between extra

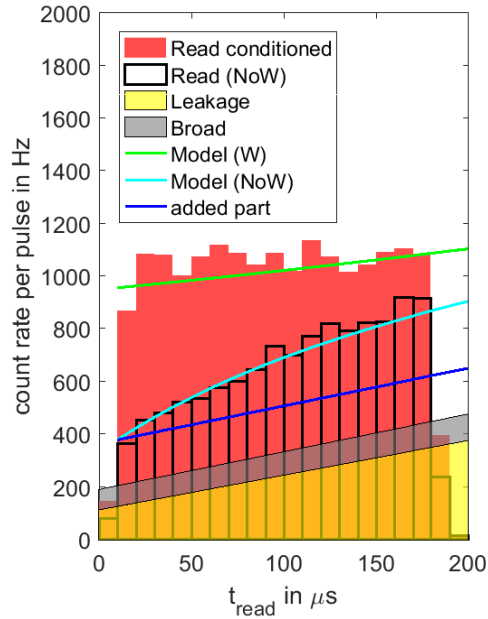


Figure 5.10: Conditional read count rate versus time. The measurement is the same as for the unconditioned data shown in fig. 5.9, left. Red bars show counts when the write pulse had been present, conditioned on at least one count during the write pulse. To guide the eye, the unconditional data without write is displayed again as unfilled bars. The yellow and gray overlay are respectively leakage and broad contributions, estimated from corresponding filter cavity scans. Green (cyan) line shows the model with (without) previous write above an added part (blue) that is constant over time. For the conditional model, we have assumed on average 0.92 symmetric collective excitations.

part and broad contribution is approximately similar to the ratio of narrow and broad peak during the write.

One might be disappointed by the very small fractional area of the pulse, that is actually attributed to good readout of the collective excitation. However, we have to keep in mind that the aim is to have good performance when conditioning on the detection of a heralding photon. When we condition the same low power data on the detection of at least one count during the write, this yields the red bars shown in fig. 5.10. Here, the fraction of good readout counts has increased because we disregarded the pulses without detection during write, thus reducing the number of experimental trials from 3 248 135 to 45 774. We have plotted the unconditional counts for the no write case as unfilled bars to guide the eye. Leakage, broad and model contributions are kept similar to the unconditional case, except for the good readout. Here we observe good agreement of data and model having assumed on average 0.92 stored collective excitations when conditioning on at least one detection during the write pulse.

We conclude that the four-wave mixing model can approximate the dynam-

ics of the read out counts when adding leakage, broad and extra contribution. While the leakage, the readout and the four-wave mixing are straightforward to understand, it is still unclear where the other contributions originate from. The added parts could come from atoms that are imperfectly pumped and initially residing in magnetic sublevels other than $m_F = 4$. Similar to the write process, the read pulse could then scatter photons into the detection mode, causing the extra and the broad contributions. Comparing the write and read powers and coupling strengths we expect for a population fraction of 6% in $|4, 3\rangle$ (corresponding to an atomic polarization of about 98.5%) a contribution which is roughly 1/3 of the observed contribution. Scattering from atoms residing in $F=3$ is even weaker due to the large detuning, that is about 10 times larger than for the $F=4$ manifold. For future experiments, it will be interesting to check the dependency of the added contributions on the quality of initial optical pumping.

We note that the cell cavity was not explicitly included in the model. More importantly we emphasize that the model does not include decay of the collective excitation. Since the duration of the read pulse is a substantial fraction of the previously determined decay time of 0.27 ms, we expect that this decay is significant. Furthermore, the model does not take into account the broad background from the four-wave mixing that leads to asymmetric collective excitations with even shorter coherence time.

How do we continue from here? We need to test our different hypotheses about the origin of the broad and the extra contribution. Other than that, one way to continue would be to improve the model to explain our findings. We had started out based on the motional averaging theory of [BZP⁺16]. Since it does not include four-wave mixing, we then switched almost exclusively to the model by [DCW14]. It might be useful to implement the four-wave mixing into the motional averaging theory. This would probably explain our results more accurately. However, it also seems to be a major undertaking to recalculate the motional averaging theory including four-wave mixing. A different approach would be to experimentally eliminate the four-wave mixing contribution. This will make it easier to explain the results with theory, and at the same time we will reduce a noise source which might lead to better correlations or even single photons. Furthermore, reducing the four-wave mixing contribution might also make it easier to investigate and identify the origin of the broad and the extra contribution. To us as experimentalists, the latter approach seems much more appealing.⁴

⁴It may seem confusing that we first set out to reduce four-wave mixing before we identified the source of broad and extra contribution, since the latter seem to contribute a larger fraction. This is mainly due to chronological reasons. We first attributed all the narrowband noise to four-wave mixing and changed our setup to suppress four-wave mixing. Only then did we realize through careful analysis, that there appears to be another narrowband contribution.

Suppression of four-wave mixing

6.1 Readout of RF-excitations

In the previous sections we have used optical Raman scattering to create collective excitations that we could then read out. Instead of optical excitation we can also use an RF pulse at the Larmor frequency to transfer atoms from $|4, 4\rangle$ to $|4, 3\rangle$. The RF coil used for excitation produces a very homogeneous field across the cell. Thus, we expect that the RF excitation has much better overlap with the symmetric collective excitation compared to the optical excitation. However, there is no heralding photon emitted during the RF excitation. Therefore this method cannot be used to read out single photon states, that require conditioning on heralding detection. Nevertheless, the RF excitation method is a very valuable tool, because we can extract many setup parameters while at the same time the method is simpler, more robust and allows us to reach higher excitation powers.

We performed an experiment, measuring the readout counts for different RF powers. The resulting count rates during the readout detection window are shown in fig. 6.1, where we have subtracted the data obtained without sending any excitation pulse. We follow the same procedure as the one used in the power scaling analysis in section 5.1. The subtraction makes it easier to compare across different sets of measurements that may include different leakage contributions. Excluding the transient edges of the the pulses, we fit the data with a simple exponential decay function $f_i(t) = c_i \exp(-t/\tau)$, with i indexing the respective RF power. We combine all RF power datasets in a single fit with a common decay time given by $\tau = (146 \pm 1)\mu\text{s}$. From the fact that all RF powers agree well with a common decay time, we can infer that the readout rate is constant for the range of powers that was used. This is a promising result since measuring at higher excitation powers leads to higher countrates and

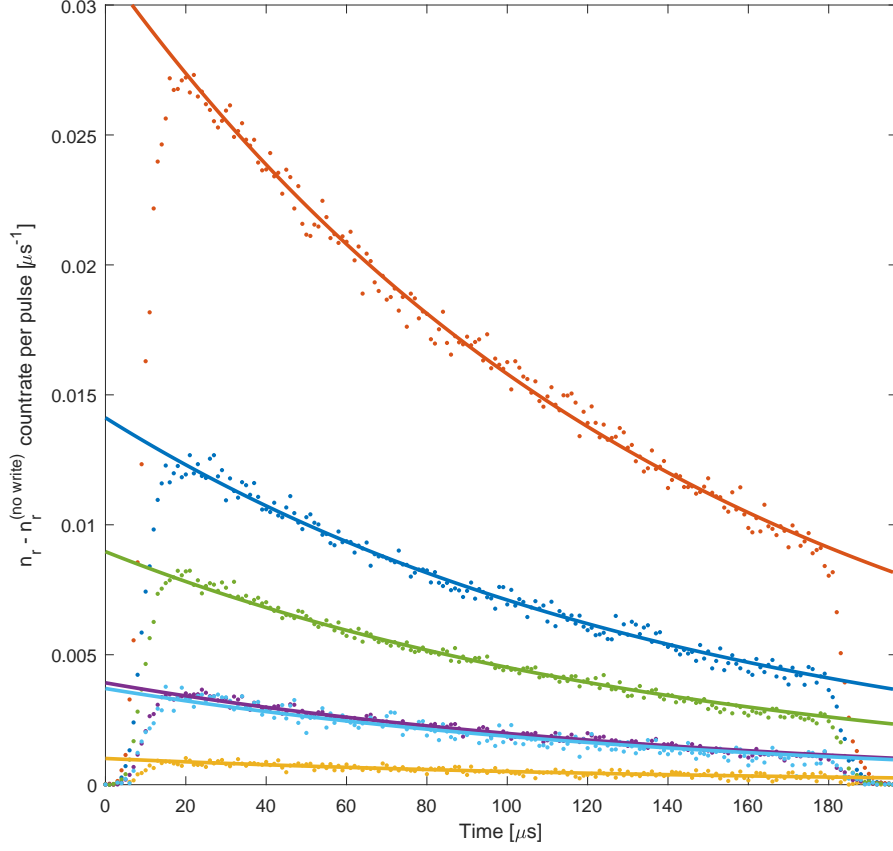


Figure 6.1: Readout countrate of RF excitations. The points show the difference in countrates during the readout between with and without RF excitation. The different colors represent different RF powers (same color coding as in fig 6.2). The respective solid lines are fits given by exponential decays $f_i(t) = c_i \exp(-t/\tau)$ with common decay time. The time axis starts with the read detection window.

thus allows shorter measurement durations for similar signal-to-noise ratios. We note that the exponential decay function used here is a simplification of the model used in eq. 2.34 similar to section 5.1. Assuming time independence of the Rabi frequency Ω_R and of $\alpha = \xi/\chi$ together with the approximation the atomic decay, we have

$$\frac{1}{\tau} = -(\xi_r^2 - \chi_r^2)\Omega_R^2 + \frac{1}{T_1} \quad (6.1)$$

This allows us to identify the apparent readout rate $(\chi_r^2 - \xi_r^2)\Omega_R^2 = 5.9$ kHz. For α only given by the ratio of Clebsch-Gordan coefficients, thus neglecting cavity detuning effects, we achieve an intrinsic readout rate of the collective excitation (i.e. in absence of four-wave mixing contribution) of $\Gamma_{read}^{(int)} = \chi_r^2\Omega_R^2 = 8.6$ kHz.

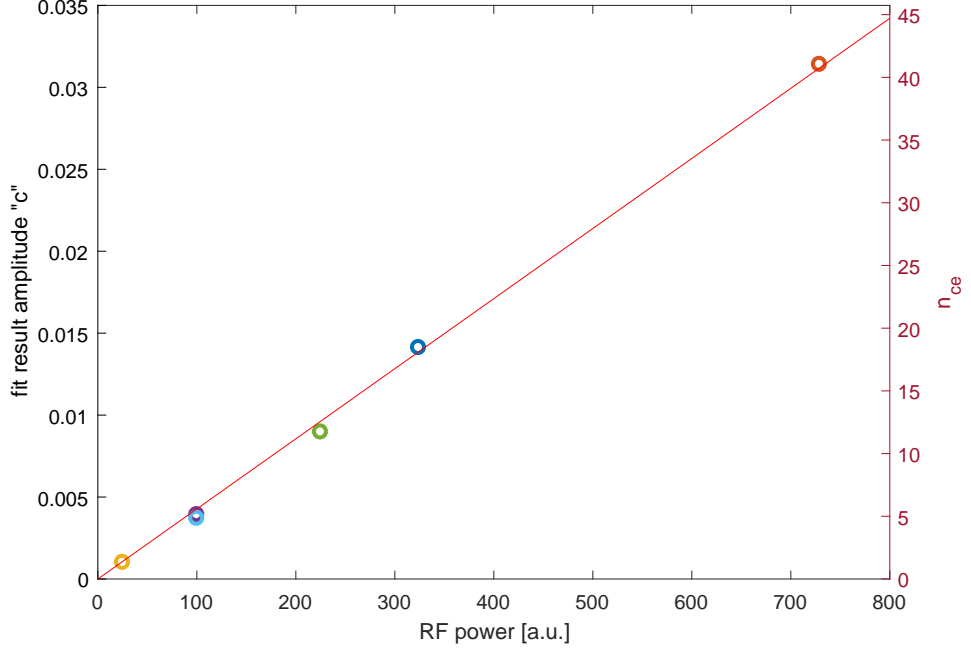


Figure 6.2: Readout amplitude versus RF power.

We note that this rate is of course dependent on the power during the readout pulse. During this experiment we used $8.4 \mu\text{W}$ input power to the cell cavity.

The amplitude c of the exponential fit is plotted against the RF power in fig. 6.2. We include a linear fit confirming a proportional dependency. Using the same approximation as above we can from eq. 2.34 derive

$$c_i = \eta \chi_r^2 \Omega_R^2 n_{ce}^{(i)} \quad (6.2)$$

where we have combined intrinsic readout, escape and detection efficiency in η . Thus, the fit amplitude c should be directly proportional to the average number of collective excitations n_{ce} . To determine the proportionality constant we take a small detour via the optical excitation experiments presented in previous sections. When exciting optically, the number of collective excitations can be well determined from the spectrum and the escape and detection efficiency. We use an optical excitation dataset and a RF excitation dataset with equal read power. We perform the above-mentioned exponential fit for each of them. The fit amplitudes c_i can then be used to determine the proportionality constant to translate the RF fit amplitudes to average numbers of symmetric collective excitations. This yields the y-axis on the right side of fig. 6.2. We note that we have spanned a range of n_{ce} of on average only 1 up to on average 40 excitations.

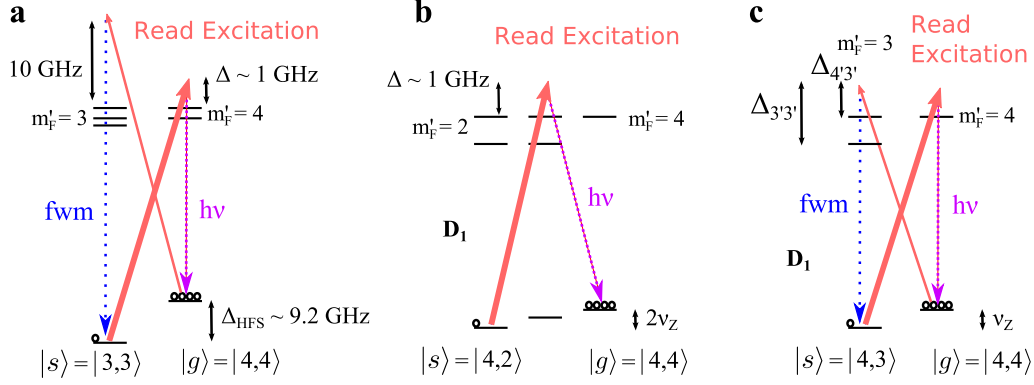


Figure 6.3: Four-wave mixing suppression schemes. **a** Hyperfine storage on D_2 line. **b** Polarization selection on D_1 line. **c** Magic detuning on D_1 line. The read excitation light in red is drawn thinner for reduced Raman coupling transitions. $h\nu$ (purple) and fwm (blue) signify the desired read-out and the undesired four-wave mixing scattering respectively. Only relevant caesium levels are shown.

6.2 Options to suppress four-wave mixing

In chapter 5 we have seen that four-wave mixing is one of the main sources contributing noise to the readout. The way to suppress four-wave mixing is to reduce the undesired coupling ζ while having a strong desired coupling χ . We will discuss in the following different options that we can choose to achieve this.

6.2.1 Hyperfine storage

We can increase the splitting between ground and storage state to make it comparable or bigger than the detuning. Then the undesired coupling will be reduced due to the larger detuning. This can be achieved by storing the collective excitation on the hyperfine transition as shown in fig. 6.3(a), where the detuning for the undesired coupling (≈ 10 GHz) will be about 10 times larger compared to the desired coupling (≈ 1 GHz). The hyperfine transition storage has been used in many experiments. One of the main advantages besides four-wave mixing suppression is also the simplification of leakage suppression, since the scattered photon will be much further detuned from the excitation light frequency. The hyperfine transition storage is the design that has been studied in [BZP⁺16]. We are therefore confident that it can be successfully set up. However, there are technical reasons that make this experiment more challenging. The cell cavity requires to be double-resonant on the excitation light and the scattered photon. The atomic phase shift will probably be different for the two frequencies, and it might show different time-evolution while the atomic state decays. Using only a single filter cavity seems to be very challenging, since this requires to carefully match all cavity resonances, detunings and the atomic phase shift. Thus it will most likely require a second filtering setup.

Beyond these purely technical reasons, there is also a much more fundamental reason. The expected coherence time on the hyperfine transition is for vapour in anti-relaxation coated cells one order of magnitude shorter than for Zeeman transitions. We measured in section 4.6 even shorter coherence times. This is the main reason why we had decided not to continue on the hyperfine storage in the first place.

6.2.2 Cavity suppression

The undesired coupling can be suppressed by having the frequency of the corresponding scattered photon off-resonant in the cell cavity. This has been experimentally used to suppress four-wave mixing by [SMC⁺16], [NMT⁺17]. The challenge is, that the undesired scattering frequency is different from the desired frequency by twice the Zeeman splitting (≈ 5 MHz). For efficient suppression, the spectral width of the cell cavity has to be narrower than this. Increasing the Zeeman splitting will require a new, possibly more massive coil system to produce the magnetic field, and might reduce the coherence time due to magnetic field inhomogeneities. Increasing the length of the cell cavity on the other hand will reduce its stability.

6.2.3 Four-wave mixing detection

During the read-out, one could filter and detect both the desired and the undesired scattered photon on separate detectors. If we then stop the read-out process as soon as the first undesired scattered photon has been detected, we will be able to observe a nearly four-wave mixing free read-out. The downside is of course, that we will only be able to read-out a small fraction until the first four-wave mixing photon is generated. This will reduce the read-out efficiency significantly. Furthermore, imperfect detection efficiency will still lead to a four-wave mixing contribution. These disadvantages render this concept not very useful.

6.2.4 Polarization selection rules

By using $|4,4\rangle$ as the initial ground state and $|4,2\rangle$ as the storage state, and by using σ_+ polarization for the excitation light and σ_- polarization scattered light during the read process (polarizations vice versa during the write process), we can suppress four-wave mixing [WEA⁺07]. The corresponding level scheme is shown in fig. 6.3(b). In our current setup, the magnetic field perpendicular to the excitation light propagation makes it impossible to drive σ_+ and σ_- polarization independently. We will need to change the geometry, such that magnetic field, pumping and excitation light are collinear. However, a major issue is that for far-detuned excitation the coupling via σ_+, σ_- transition vanishes [VB13]. This is due to the Clebsch-Gordan coefficients that interfere

destructively. One solution is to use the D₁ line of caesium. Here the excited state hyperfine splitting (≈ 1.2 GHz) is comparable to the detuning (≈ 1 GHz), thus the contributions from the different hyperfine states do not interfere completely. This four-wave mixing suppression scheme requires very clean light polarizations. Further disadvantages of the scheme are the reduced interaction strength and the need for major rearrangement of the setup, including changing the wavelength.

6.2.5 Magic detuning

The coupling suppression because of destructive interference of several excited states was nuisance in the previous subsection. However, we can also use it to our advantage and suppress only the undesired coupling.

In a multilevel atom Raman scattering can be driven via different excited states i . The respective Raman-Rabi frequency that couples the ground states $\{1, 2\}$ is given by [Ste15] (see also section 2.2)

$$\Omega_{RR} = \sum_i \frac{\Omega_{1i}\Omega_{2i}}{2(\Delta - \delta_i)} \quad (6.3)$$

where the common detuning Δ is adjusted by the detuning of the light field to each state i to $\Delta - \delta_i$. Each Rabi frequency Ω_{ji} with $j \in \{1, 2\}$ is proportional to the respective dipole matrix element d . This in turn can be expressed by a multiplication of the reduced dipole matrix element with the Clebsch-Gordan coefficient C as

$$d_{F, m_F, F', m'_F} = \langle J || er || J' \rangle C \quad (6.4)$$

where the reduced dipole matrix element $\langle J || er || J' \rangle$ is $3.8 \cdot 10^{-29}$ Cm for the D₂ line, and $2.9 \cdot 10^{-29}$ Cm for the D₁ line [Ste10]. The transitions via the different excited states can thus add constructively to the Raman-Rabi frequency, or interfere destructively, depending on the signs of the contributing Clebsch-Gordan coefficients. Whenever Clebsch-Gordan coefficients of two or more transitions have different signs, there will be at least one "magic detuning" where the resulting coupling strength is vanishing. However, since we work with atoms at room temperature, we need to consider atomic motion. We recall from chapter 2 that this leads to a Faddeeva function of the detuning. The resulting coupling is shown for the D₁ line in fig. 6.4. This figure is analog to the previously shown fig. 2.8 for the D₂ line. For us it is important to work at a large detuning compared to the Doppler width therefore we require a magic detuning outside of the Doppler width. For the D₂ line of caesium, the excited state splitting is too small to achieve this condition. However, for the D₁ line, as indicated in fig. 6.3(c), the transitions from $|4, 4\rangle$ to $|3, 3\rangle$ via $|4', 3'\rangle$ and $|3', 3'\rangle$ cancel at a detuning of ≈ 924 MHz blue from $|4', 4'\rangle$.

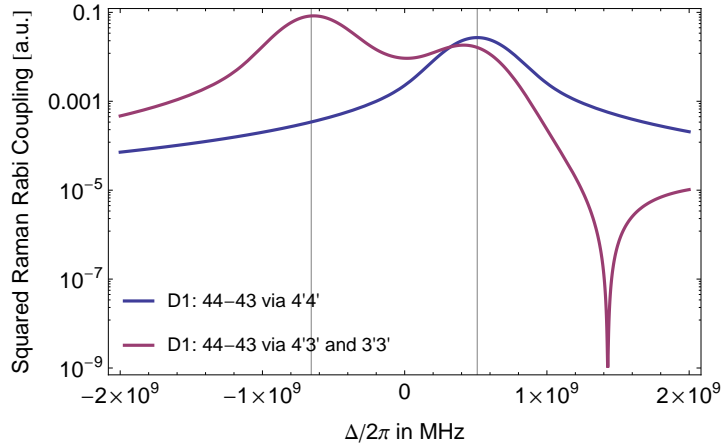


Figure 6.4: Squared Raman Rabi Coupling $|\sum_m g_m \Omega_m w[\frac{\Delta_m + i\gamma/2}{\Gamma_D}] / \Gamma_D|^2$ for the transition $|4, 3\rangle \leftrightarrow |4, 4\rangle$ via the D_1 line versus light detuning. Zero detuning corresponds to the D_1 line without hyperfine splitting. The black vertical lines show the caesium hyperfine resonances of $|F' = 3\rangle$ on the left and $|F' = 4\rangle$ on the right. For the readout we have χ^2 in blue and ζ^2 in red.

6.3 Read-out on D1 line

We note that currently the optical write excitation is driven via the transitions corresponding to the coupling ζ . Thus by suppressing ζ we also suppress the write excitation. Changing the polarization of the excitation light such that the write excitation also couples to the atoms via χ seems an obvious choice, but comes along with technical complications. We would either have no polarization filtering or it requires a second detection setup or polarization switching. However, for a proof-of-principle experiment about four-wave mixing reduction we can apply the technique presented in the section 6.1. We excite the collective excitation via an RF pulse and then read out optically.

6.3.1 Setup at 895 nm

The optical setup was not initially designed to be compatible with both D_1 and D_2 . First of all we had to replace the laser. Using a Ti:Sapph laser fiber-coupled from a different lab seemed the easiest solution, but the long fiber (≈ 40 m) turned out to contribute too high polarization noise. We therefore replaced the previously used ECDL by a home-built ECDL set up for a wavelength of 895 nm. The ECDL output was coupled into the previously used forward and backward fibers - and the optical feedback setup worked straight-away. We could obviously not use the same reference laser for absolute stabilization via a beatnote signal. We therefore switched to using the pump laser as a reference laser. Previously, the reference laser, which was the so-called probe laser, was also used to lock the cell cavity. Since the pump laser is resonant with the atoms, it is not suitable for locking. Thus, we continued using the far-detuned

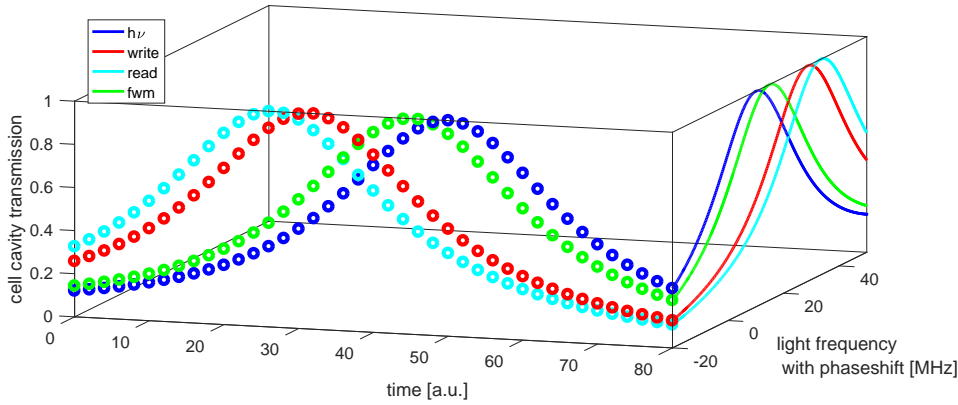


Figure 6.5: Expected cell cavity resonance for light at write (red) and read (cyan) frequency in y polarization and single photon (blue) and four-wave mixing (green) frequency polarized along π , shown for light detuned from the D1 line as in the experiment (frequency-axis shifted arbitrarily). y -polarized light is shifted relative to π by 21 MHz. Assuming linear change of phase shift over time, the cavity resonance shift for the respective frequencies is displayed (circles).

probe laser for locking the cell cavity. Changing the length of a resonant cavity by half a wavelength only changes the longitudinal modenumber, the light frequency is still on resonance with the cavity. In our case the wavelength of the light used for locking and the light for the experiment are different by 5%. Changing the longitudinal modenumber by one thus shifts the cavity from double-resonant to single-resonant. Therefore care has to be taken to keep the cell cavity locked on the same mode. Nearly all of the standard optical components could be still used with the new wavelength since they had broadband antireflection coatings. We tested the cavities that fortunately performed similarly well at 895 nm, except the extra cavity that exhibited worse transmission due to the reduced reflectivity of the high-reflective curved mirror (see specifications in Appendix B). Together with the lower quantum efficiency of the single photon detector, as specified for longer wavelength, we measured an overall detection efficiency of 1.5%. We briefly note, that we observed a different phase shift and a different time-evolution of the phase shift for light on the D₁ line (shown in fig. 6.5) compared to the D₂ line (shown in fig. 4.5).

The conclusion of this subsection is, that with manageable amount of changes we could in reasonable time change the complete setup to run preliminary tests at a different wavelength.

6.3.2 Comparison of D₁ and D₂: Filter cavity scan

First, we performed a filter cavity scan, similar to the experiment presented in section 5.2, but with RF write excitation instead of optical write excitation. The resulting spectrum is shown in fig. 6.6. The data is shown in red for the

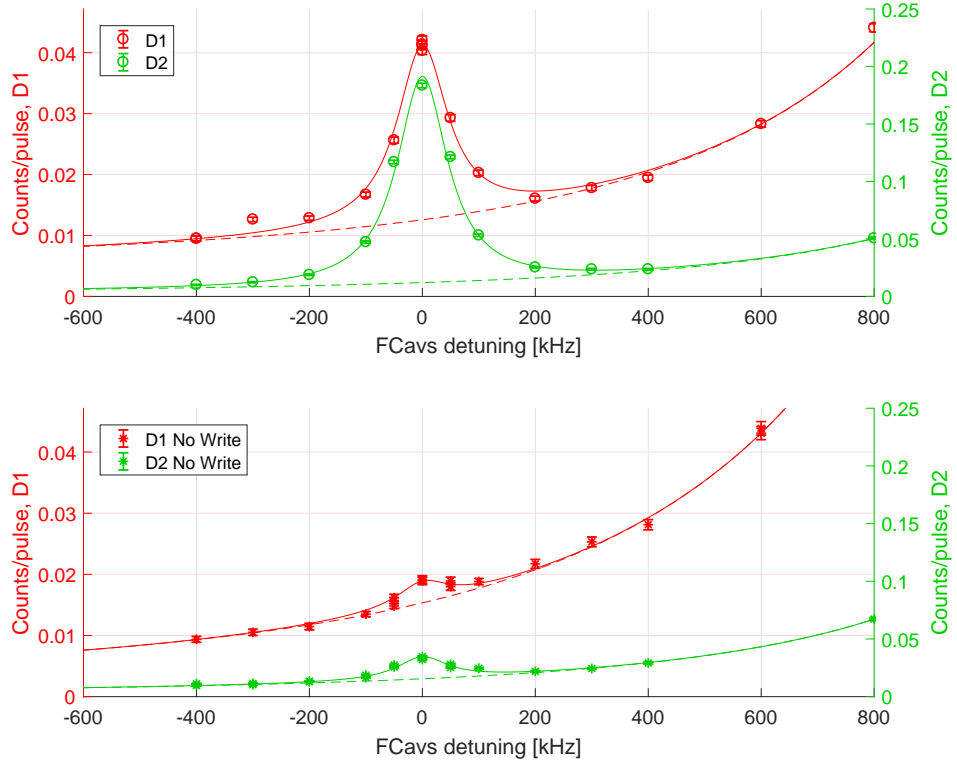


Figure 6.6: Read counts during $60 \mu\text{s}$ window for different detunings of the filter cavities. For fixed non-zero (top) and zero (bottom) RF excitation power the read counts using D1 (red) or D2 (green) line are shown. The solid lines are fits with the contribution of leakage and broad background shown as dashed lines.

D₁ line and in green for the D₂ line. The upper figure shows the filter cavity scan when the RF write pulse was present, the bottom figure shows the result without RF write pulse. The RF write excitation powers were similar for the D₁ and D₂ experiments. The read excitation power for the D₂ experiments was the same as for the RF measurement in the previous section. We had about 1.65 higher intracavity read excitation power for the D₁ experiment than for the D₂ experiment. The considered detection window of the read pulse was $60 \mu\text{s}$ long. The y-axes in the figure are scaled to each other by the respective detection efficiencies. In the top graph, for both wavelengths we observe the narrow peak from the desired readout above the background attributed to broad and leakage contribution. Accounting for the different detection efficiencies, we observe similar peak heights from the desired readout and infer that the strength of the atomic response is about the same order of magnitude.

We observe a leakage contribution which is about four times higher for the D₁ than for the D₂ experiment, probably mostly due to worse polarization filtering. The leakage contribution was also drifting during the course of the experiment.

This is obvious when comparing the leakage with write and without write. Chronologically the data points were taken for D_1 from high to low detunings with write and then from low to high detunings without write. The relative change in leakage from the start of the experiment to its end was more than 50%. We can also see a drift of the leakage in the D_2 experiment, where the data with write and without write was taken with about half an hour of separation. The relative change was less, but still about 40%.

In the case where we did not have a write excitation pulse (fig. 6.6 bottom), for both wavelengths we observe a narrow peak at zero detuning. The ratio between the counts attributed to the narrow peak without write and with write is similar for both wavelengths. However, concluding from this, that there is no four-wave mixing suppression for D_1 , is not correct. As we have observed in section 5.5, there is an extra narrow linewidth contribution. For further investigation, we therefore take the same strategy as for the D_2 line. We fit the filter cavity scans for different time slices of the read window, extract the leakage and broad contributions and then focus in the following on the evolution of the readout count rate at zero detuning over time.

6.3.3 Comparison of D_1 and D_2 : Read-out pulse shape

We investigate the time evolution of the readout pulse for the D_1 experiment and the D_2 experiment for similar RF write excitation power. The detected count rates are shown in fig. 6.7, where the filled red bars show the data when there was a write excitation present, and the black unfilled bars show the data when there was no write excitation. Both for the D_2 data on the left and the D_1 data on the right, we have shown the leakage and the broad contribution in yellow and grey respectively. These are extracted from the filter cavity scan and linearly approximated. On top of these contributions we then apply the four-wave mixing model as discussed previously in section 5.5. As input parameters we choose the number of symmetric collective excitations $n_{ce} = 5.7$, extracted from fig.6.2. For D_2 , we furthermore use the same couplings χ , and ζ as in the previous readout pulse shape analysis and we add an extra constant offset which is, as previously, a factor 1.8 higher than the broad contribution. For the D_1 line we scale the coupling χ with three terms: with the reduced dipole matrix element $|\langle J||er||J' \rangle|^2$, the Clebsch-Gordans for the respective transitions weighed by the detuning $|\sum_m g_m \Omega_m / \Delta_m|$ and the cell cavity transmission of the different light fields at different detunings. We have assumed that ζ is about 14 times smaller than χ . This is a conservative estimate. According to fig.6.4 we should expect a much bigger suppression. We reduce the added constant contribution for D_1 to only 1.2 times the broad contribution, otherwise we would overestimate the case without write. The resulting contributions from the model are shown in green and cyan for with and without write, respectively. The blue line shows the added constant contribution.

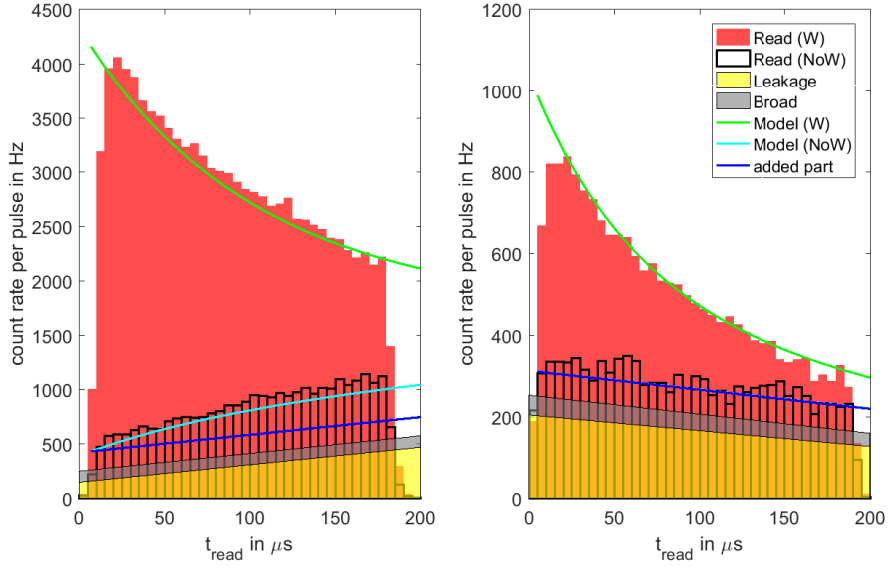


Figure 6.7: Photon shapes versus time. Left (right) for D2 (D1) with similar RF power for write excitation. Red bars show counts when the write RF pulse had been present, unfilled bars when not. The yellow and gray overlay are respectively leakage and broad contributions, estimated from corresponding filter cavity scans. Green (cyan) line shows the model with (without) previous write above an added part (blue) that is constant over time.

For both wavelengths we observe good agreement with the model. Both the count rate and the shape over time of the readout collective excitations are as expected from the model. The "no write" case is slightly underestimated for the D₂ experiment. This could easily come from the drift of the leakage during the experiment. Most importantly, we can clearly identify a significant four-wave mixing contribution in the D₂ case. Contrarily, in the D₁ case not only the model predicts negligible four-wave mixing (the cyan line is not visible due to the overlapping blue line), but also in the data we see a constant evolution over time. The absence of a rising contribution, which would be the signature of four-wave mixing, confirms that we have suppressed four-wave mixing. This is a promising conclusion regarding future creation and verification of single photons.

With the current data, it is not possible to give a experimental number for the ratio between χ and ζ . This could be achieved with a much bigger dataset, thus reduced fluctuations in the countrate. However we expect a suppression of the four-wave mixing by more than two orders of magnitude compared to the desired readout. Even after a possible increase of the detection efficiency to a value similar to the D₂ experiment, confirming this would require a measurement over several hours. An alternative option would be to measure the four-wave mixing contribution for different detunings, where the ratio is not as

favourable, then compare with the theoretical expectations and extrapolate to the chosen detuning.

Discussion

We have presented here the first implementation of the readout of a heralded excitation in an anti-relaxation coated vapour cell based on motional averaging with efficient heralding and readout. The concept of motional averaging has allowed us to achieve a life-time of the collective excitation of 0.27 ± 0.04 ms. This is two orders of magnitude longer than the previous record with room temperature experiments using atomic vapours with buffer gas by [DYD⁺17] and [BFV12]. We have verified the non-classicality between heralding and readout fields by a significant violation of the classical bound of the Cauchy-Schwarz parameter with $R = (1.4 \pm 0.1) > 1$.

The observed spectrum of the scattered photons during the write process consists of a narrow and a broad contribution corresponding to the symmetric and the asymmetric collective excitations, and is in accordance with the theory developed in [BZP⁺16]. This allows us to determine the write efficiency of $(63 \pm 1)\%$. This experimental value agrees with the theoretical expectation. It lies in between the value from the analytical expression (eq. 2.29) of 73% and the simulated value for excitation into $|3, 3\rangle$ of around 60% (see fig. 2.4). For a time-window of the readout of $40\mu\text{s}$, we have determined the retrieval efficiency of $\eta_R^i = (16.1 \pm 0.9)\%$, which has been corrected for the detection efficiency. Increasing the time-window to $200\mu\text{s}$ leads to a three-fold increase of the retrieval efficiency, at the cost of higher noise contributions, thus lower single photon fidelity. We can infer the number of symmetric collective excitations from the spectrum and the detection efficiency. The number of classical photons at the cell cavity output per symmetric collective excitation agrees within 10% with the estimate given in section 2.5 of $1.2 \cdot 10^8$ classical photons per quantum photon. We have partly succeeded in the challenge of filtering the classical photons. Their leakage has been suppressed during the write process. However, birefringence and atomic decay have led to a significant leakage contribution during the the read process.

We have to acknowledge that we have not succeeded in creating a single pho-

ton source. Even though we have verified the non-classicality of the correlations between write and read fields, we have not been able to demonstrate non-classicality of the heralded readout. The measured read autocorrelation conditioned on a write click is $g_{RR|W}^{(2)} = 1.3 \pm 0.2$ which is higher than the classical bound of one. We attribute this to the big fraction of excess noise, that appears to follow thermal distributions.

We have investigated the noise contributions via spectral and temporal analysis. We could identify the leakage contribution, furthermore a broadband and a narrowband contribution. The narrowband contribution consists of two different parts, one constant and the other increasing over time. The latter one can be well described by a model of [DCW14] and has been identified as four-wave mixing noise. The four-wave mixing noise is intrinsic to our excitation scheme. We have presented different strategies to eliminate four-wave mixing noise.

We have shown that we can read out collective excitations created by a RF pulse and we have used this for a proof-of-principle experiment that has confirmed the suppression of four-wave mixing.

7.1 Quantum repeater compatibility

We have initially motivated this work with the need for scalable room temperature quantum repeaters. Using atomic vapour cells at around 40°C, we have indeed presented a room temperature system. In terms of scalability we have to consider the total setup. The narrowband laser is in this experiment a bulky prototype which leaves room for optimization and commercial solutions with comparable linewidth and better reliability are available. Careful engineering will also lead to more robust and miniaturized filter cavities.

Apart from these technical details there are relevant intrinsic parameters. We have reported a significant increase in storage time compared to buffer gas systems. However, a photon will only travel over a distance of 81 km during the storage duration of 0.27 ms that we have measured. For the initial DLCZ scheme [SSdRG11] calculate the crossover point where the quantum repeater performance will beat the direct transmission¹ to be at 630 km requiring an entanglement distribution time of 340 s. For other protocols considered in [SSdRG11], the crossover requires shorter storage times on the order of seconds. This suggests, that our storage duration is still more than three orders of magnitude too low to reach the crossover.

The time bandwidth product of our system is currently limited by the read pulse duration. If we take into account the initialization duration of 350 μ s before each write-read sequence and the write pulse duration of 33 μ s, the effec-

¹[SSdRG11] make a few assumptions here, e.g. 90% efficiency for detection efficiency and memory efficiency, 10 GHz repetition rate of the single photon source, 4 repeater link segments.

tive time-bandwidth product drops for our system even below one. According to theoretical derivation of [BZP⁺16] (see also fig.2.4) a readout duration of 100 μ s should yield a read efficiency close to 90%. Assuming negligible initialization duration this gives for our storage duration a time-bandwidth product on the order of 2. This is significantly lower than the time-bandwidth product reported for buffer gas cells, that have reached more than 1000 [RML⁺11].

In our experiment we use the D₂ line of caesium at around 852 nm, the last section uses the D₁ line. These wavelengths are not in the telecom bands above 1260 nm which are used for communication via optical fiber due to low transmission loss. However, the connection of quantum interfaces with frequency-converted photons has been demonstrated [RDZ⁺10], [AFFG⁺14], although leading to reduced efficiency. Furthermore, the caesium wavelengths are suitable for free-space quantum communication [FUH⁺09].

Motional averaging eliminates the readout of the asymmetric modes. On the one hand this allows for efficient readout, on the other hand this also eliminates spatial multi-mode capability [CW12] or temporal multiplexing [Alb15]. Due to the given atomic level structure, the spectral multiplexing capabilities of our system are very limited. A huge advantage of our source is the technological simplicity that allows spatial multiplexing operating many sources in parallel. We acknowledge, that engineering challenges, as the mass-production of cells and filter cavities, need to be overcome.

7.2 Limitations and improvements

Our spectral and temporal analysis has shown, that there is a significant contribution of noise to the output field during the readout. We can divide the noise sources into intrinsic and extrinsic sources. As extrinsic, we count the contributions that are not connected to atomic scattering, in our case background and leakage. Background counts have a negligible contribution to both write and read output fields thanks to a state of the art avalanche photo diode. Further reduction of the background counts would require super-conducting photo detectors which introduce technical complexity. The leakage of excitation light is reduced by our filtering. We can only eliminate the leakage contribution either during the write or the read process due to birefringent effects. We typically eliminate it during the write which leads to a leakage contribution of about 1/3 to the total readout field (see fig.5.4). We expect that a narrower spectral filter will greatly reduce this leakage. An obvious step for the future of this experiment is the replacement of the extra cavity that has shown suboptimal transmission on the D₁ line by a more narrowband version. The following intrinsic noise sources are typically more difficult to eliminate. Four-wave mixing noise has been observed in our DLCZ-type experiment. It is increasing over time and has contributed nearly up to one half of the intrinsic noise at the end of the

read pulse, averaged over the read pulse roughly one quarter (see fig. 5.9). We have presented a variety of possible solutions to eliminate four-wave mixing noise in section 6.2 and we have performed a proof-of-principle experiment in section 6.3 that experimentally confirms the suppression of four-wave mixing. This leaves two noise contributions, the broadband and the narrowband "extra" part. The origins of both of them are still unclear, however the constant ratio may indicate that they have a common origin. One hypothesis is scattering from the initial population in $|4,3\rangle$. However, given a typical atomic polarization of 98.5%, we estimate a contribution that is only about 1/3 of the actually observed experimental value. Further experimental investigation is needed to determine the origin. We propose a test experiment with a microwave pulse after the state initialization that transfers population from $|4,3\rangle$ to $|3,2\rangle$. Since the microwave allows to specifically address individual Zeeman sublevels, this should yield a convenient way to analyse the influence of population. Another possibility is to change the pumping duration or power to measure for different populations in $|4,3\rangle$.

Another noise contribution is the scattering from asymmetric collective excitations during the write. These false heralding events during the write will lead to a higher noise fraction in the conditional readout field. The write efficiency can be improved by increasing the waist inside the cell ². However, the trade-off between increased clipping losses and better efficiency has not been thoroughly investigated, yet.

The optical depth can be further increased by increasing the cell temperature. This will lead to less excitation photons that need to be filtered, and thus less leakage noise. On the other hand it will also lead to more phase shift by the atoms, increasing the cavity drift with atomic decay. Furthermore, there are technical obstacles as e.g. the possibility for disappearance of the atoms from the cell (see section 4.3).

We can use the model from section 2.8.1 to predict the correlation values for the improved parameters. If we improve the leakage reduction during the read by a factor of 10 and assume reduction of four-wave mixing noise by a factor of 100, the model predicts a non-classical conditional read autocorrelation of $g_{RR|W}^{(2)} < 0.9$. If we further assume a reduction of the broadband and narrowband noise by a factor 4, the model predicts $g_{WR}^{(2)} \approx 4.3$, $R > 7$ and $g_{RR|W}^{(2)} < 0.5$ which indicates a strong contribution of a single photon state [Ste13]. We emphasize again that the model presents a simplification and its predictions should be taken with care (see section 2.8.1).

²As an example, an increase from 55 μm to 60 μm will increase the write efficiency by 4%

7.2.1 Increasing the storage time

One of the main results of our experiment is the lifetime of the stored excitation. We have estimated in section 2.8.2 that the lifetime is limited by half of the coherence time T_2 . In fig. 4.2 we can see that there are other cell candidates with close to an order of magnitude longer coherence time and similar coating (e.g. F1). It will be straightforward to replace the cell and test if the storage performance is improved. Other cells with alkene coatings have shown even longer coherence times, however their performance at around 40° has to be verified. We expect that such a change of the cell will lead to an improvement of the storage time by about one order of magnitude.

Conclusion and outlook

In this thesis we have studied the heralding and readout of collective excitations in a room temperature vapour cell with anti-relaxation coating. We have characterized the performance of vapour cells and concluded that the Zeeman transitions are most promising in our setup for the storage of collective excitations. This is due to slower population transfer into the storage state by collisions and due to order of magnitudes longer coherence time. We have then demonstrated efficient heralding and readout of collective excitations on the single photon level by successfully utilizing the concept of motional averaging. The non-classicality of the correlations between the write and read output fields has been shown by violation of the Cauchy-Schwarz inequality. We have achieved a lifetime of the collective excitation of 0.27 ± 0.04 ms which is two orders of magnitude longer than previous DLCZ-type experiments with room-temperature vapour cells. We have analysed the contributions to the readout field both spectrally and temporally to identify the contributing noise sources. One of these sources, the leakage of excitation light, can be eliminated straightforwardly by improving the filtering stage, e.g. by adding another cavity. The intrinsic four-wave mixing noise also contributes to the readout field. We have discussed possible solutions and we have demonstrated in a proof-of-principle experiment the successful suppression of the four-wave mixing noise. Further investigation will be necessary to identify the origin of the remaining noise. One main part of this noise is probably due to imperfect atomic state initialization.

We expect that combining the demonstrated four-wave mixing suppression scheme with the heralded creation of collective excitations and improved filtering will bring us a huge step forward towards the generation of non-classical photon states. Identifying the remaining noise will allow us to judge its possible reduction paving the way towards a single photon source. The most interesting future of this experiment lies in the connection to other experiments. This could be a similar setup that would allow us to investigate the fidelity of

the single photon output or maybe to continue along the lines of the DLCZ-proposal to entangle two cells. A setup including several cells could also be used to demonstrate multi-photon experiments. Another idea is the connection to a different system, e.g. a mechanical oscillator, to demonstrate a hybrid experiment where a single excitation is distributed between an atomic system and an opto-mechanical system.

Part III

Appendix

Write process for Zeeman transition

We extend the calculation from [BZP⁺16] to include several excited states. We focus on the usage of Zeeman states for storing the collective excitation. We do not include any four-wave mixing. This makes sense for the hyperfine transition but does not hold true for the Zeeman transition. However at least for the write process in the limit of low excitations it should be a valid approximation.

A.1 From Hamiltonian to light-atom coupling θ

We start with the Hamiltonian as in equation (1) of [BZP⁺16] adding the relevant levels

$$\hat{H} = \sum_{j=1}^N \sum_m -\Delta_m \hat{\sigma}_{e_m e_m}^{(j)} - \left(\frac{\Omega_j^{(m)}(t)}{2} \hat{\sigma}_{e_m 0}^{(j)} + g_j^{(m)}(t) \hat{a}_{cell} \hat{\sigma}_{e_m 1}^{(j)} + H.c. \right) \quad (\text{A.1})$$

where we sum over N atoms and include each excited level e_m . (In our current D₂ scheme $m \in \{1, 2, 3\}$). The quantum field inside the cell cavity is described by \hat{a}_{cell} . From this Hamiltonian we obtain the equations of motion

$$\frac{d\hat{a}_{cell}}{dt} = -\frac{\kappa_1}{2} \hat{a}_{cell} + i \sum_{j=1}^N \sum_m g_j^{(m)*}(t) \hat{\sigma}_{1e_m}^{(j)} + \hat{F}_{\kappa_1} \quad (\text{A.2})$$

$$\frac{d\hat{\sigma}_{1e_m}^{(j)}}{dt} = -\left(\frac{\gamma_m}{2} - i\Delta_m \right) \hat{\sigma}_{1e_m}^{(j)} - i g_j^{(m)}(t) \hat{a}_{cell} (\hat{\sigma}_{e_m e_m}^{(j)} - \hat{\sigma}_{11}^{(j)}) + i \frac{\Omega_j^{(m)}(t)}{2} \hat{\sigma}_{10}^{(j)} + \hat{F}_{1e_m}^{(j)} \quad (\text{A.3})$$

$$\frac{d\hat{\sigma}_{10}^{(j)}}{dt} = \sum_m (-i g_j^{(m)}(t) \hat{a}_{cell} \hat{\sigma}_{e_m 0}^{(j)} + i \frac{\Omega_j^{(m)*}(t)}{2} \hat{\sigma}_{1e_m}^{(j)}) \quad (\text{A.4})$$

We assume a small perturbation thus $\hat{\sigma}_{e_m e_m}^{(j)} \approx \hat{\sigma}_{11}^{(j)} \approx 0$ for all m and we assume that the decay rates of the m excited levels are similar: $\gamma_m \approx \gamma$ for all m . We neglect the noise operators \hat{F} since they will not lead to clicks in the detector. With these approximations we formally integrate the first two equations of motion.

$$\hat{a}_{cell}(t) = \hat{a}_{cell}(0)e^{-\frac{\kappa_1}{2}t} + \int_0^t dt' e^{-\frac{\kappa_1}{2}(t-t')} [i \sum_{j=1}^N \sum_m g_j^{(m)}(t') \hat{\sigma}_{1e_m}^{(j)}] \quad (\text{A.5})$$

$$\hat{\sigma}_{1e_m}^{(j)}(t) = \hat{\sigma}_{1e_m}^{(j)}(0)e^{-(\frac{\gamma}{2}-i\Delta_m)t} + \int_0^t dt' e^{-(\frac{\gamma}{2}-i\Delta_m)(t-t')} [i \frac{\Omega_j^{(m)}(t')}{2} \hat{\sigma}_{10}^{(j)}] \quad (\text{A.6})$$

We insert the second equation into the first and use that $\hat{a}_{cell}(0) = 0$ and $\hat{\sigma}_{1e_m}^{(j)}(0) = 0$. This yields

$$\hat{a}_{cell}(t) = -\frac{1}{2} \sum_{j=1}^N \int_0^t dt' \int_0^{t'} dt'' e^{-\frac{\kappa_1}{2}(t-t')} [\sum_m e^{-(\frac{\gamma}{2}-i\Delta_m)(t'-t'')} g_j^{(m)}(t') \Omega_j^{(m)}(t'') \hat{\sigma}_{10}^{(j)}] \quad (\text{A.7})$$

When we are working on the D_2 line we can simplify the expression by assuming the same detuning from each excited state since we have $\Delta_1 \approx 750$ MHz, $\Delta_2 \approx 1$ GHz and $\Delta_3 \approx 1.2$ GHz. However, for the D_1 transition the excited level hyperfine splitting is about 1.2 GHz and thus comparable to our typical detuning. To find the field at the detector we need to propagate the field through the filter cavity which has a decay rate κ_2 . The input-output relation for the filter cavity are

$$\frac{d\hat{a}_{filter}}{dt} = -\frac{\kappa_2}{2} \hat{a}_{filter} + \sqrt{\kappa_2 \kappa_1 / 2} \hat{a}_{cell} \quad (\text{A.8})$$

$$\hat{a} = \sqrt{\kappa_2 / 2} \hat{a}_{filter} \quad (\text{A.9})$$

where \hat{a}_{filter} describes the field inside the filter cavity, and \hat{a} is the field after the filter cavity, i.e. at the detector. Formal integration then yields

$$\hat{a} = -\frac{\kappa_2 \sqrt{\kappa_1}}{4} \sum_{j=1}^N \theta_j(t) \hat{\sigma}_{10}^{(j)} \quad (\text{A.10})$$

where

$$\theta_j(t) = \int_0^t dt' \int_0^{t'} dt'' \int_0^{t''} dt''' e^{-\frac{\kappa_2}{2}(t-t')} e^{-\frac{\kappa_1}{2}(t'-t'')} \sum_m e^{-(\frac{\gamma}{2}-i\Delta_m)(t''-t''')} g_j^{(m)}(t'') \Omega_j^{(m)}(t''') \quad (\text{A.11})$$

To calculate the expression for $\langle \theta_j(t) \rangle_e$, we assume that The z-component of the couplings g and Ω are given by the standing wave in the cavity and thus

approximated by

$$\Omega_j^{(m)}(t''') = \Omega_{xy}^{(j,m)}(t'') \sin(k_c(z_j(0) + v_z^{(j)}(0)t''')) \quad (\text{A.12})$$

$$g_j^{(m)}(t'') = g_{xy}^{(j,m)}(t'') \sin(k_q z_j(t'')) \quad (\text{A.13})$$

where k_c, k_q are the wavenumbers of the classical and quantum field respectively, $g_{xy}^{(j,m)}(t), \Omega_{xy}^{(j,m)}(t)$ are the radial dependency of the couplings. The time scale of the t''' integral is given by $1/\Delta$. The radial dependency of the coupling, given by the beam waist, is assumed constant over this timescale. This is not the case for the z-component that changes over the length scale of the standing wave. We assume that the velocity of the atoms does not change during this timescale and therefore $z_j(t'') = z_j(0) + v_z^{(j)}(0)t''$. We can then perform the integral over t''' yielding

$$\theta_j(t) = -\frac{1}{4} \int_0^t dt' \int_0^{t'} dt'' e^{-\frac{\kappa_2}{2}(t-t')} e^{-\frac{\kappa_1}{2}(t'-t'')} \sum_m g_{xy}^{(j,m)}(t'') \Omega_{xy}^{(j,m)}(t'') \quad (\text{A.14})$$

$$\cdot \left[\frac{e^{-i(k_c-k_q)z_j(t'')} - e^{-i(k_c+k_q)z_j(t'')}}{-\gamma/2 + i(\Delta_m + k_c v_z^{(j)}(t''))} + \frac{e^{i(k_c-k_q)z_j(t'')} - e^{i(k_c+k_q)z_j(t'')}}{-\gamma/2 + i(\Delta_m - k_c v_z^{(j)}(t''))} \right] \quad (\text{A.15})$$

where we have adiabatically eliminated the atomic decay since we are far detuned. We now calculate $\langle \theta_j(t) \rangle_e$, taking the ensemble average. We assume that the atoms are spatially equally distributed over the cell of dimensions $L_x L_x L_z$ and the velocities follow the Maxwell-Boltzmann distribution. The x, y dependence is only in the couplings that are assumed to follow a Gaussian beam profile with waist w . This yields for the ensemble average of this part

$$\frac{1}{L^2} \int_{-L/2}^{L/2} dx \int_{-L/2}^{L/2} dy \sum_m g_m e^{-\frac{-x_j(t'')^2 - y_j(t'')^2}{w^2}} \Omega_m e^{-\frac{-x_j(t'')^2 - y_j(t'')^2}{w^2}} \quad (\text{A.16})$$

$$= \sum_m g_m \Omega_m \frac{\pi w^2}{2 L^2} \text{Erf} \left(\frac{L}{w\sqrt{2}} \right)^2 \approx \sum_m g_m \Omega_m \frac{\pi w^2}{2 L^2} \quad (\text{A.17})$$

where we have in the last approximation ignored any small portion of the beam outside of the cell. We assume that $k_c \approx k_q = k$, and we assume that $kL_z \gg 1$. For the average over z the ensemble average of the relevant part $\langle e^{\pm 2ikz} \rangle \approx 0$ vanishes. For the remaining velocity average we have

$$\frac{-1}{\sqrt{\pi}} \int_{-\infty}^{+\infty} \sqrt{\frac{m}{2k_B T}} e^{-\frac{mv^2}{2k_B T}} \left[\frac{1}{\gamma/2 + i(kv - \Delta_m)} + \frac{1}{\gamma/2 + i(kv - \Delta_m)} \right] dv \quad (\text{A.18})$$

$$= -\frac{\sqrt{\pi}}{\Gamma_D} \left[\frac{i}{\pi} \int_{-\infty}^{+\infty} \frac{e^{-t^2}}{\frac{\Delta_m + i\gamma/2}{\Gamma_D} - t} dt - \frac{i}{\pi} \int_{-\infty}^{+\infty} \frac{e^{-t^2}}{-\frac{\Delta_m + i\gamma/2}{\Gamma_D} - t} dt \right] \quad (\text{A.19})$$

$$= \frac{2\sqrt{\pi}}{\Gamma_D} \left(w \left[\frac{\Delta_m + i\gamma/2}{\Gamma_D} \right] - e^{-\left(\frac{\Delta_m + i\gamma/2}{\Gamma_D}\right)^2} \right) \quad (\text{A.20})$$

where $w[z] = \frac{i}{\pi} \int_{-\infty}^{+\infty} \frac{e^{-t^2}}{z-t} dt$ is the Faddeeva function. We have introduced $\Gamma_D = k\sqrt{2k_B T/m}$ and we have used the variable change $t = v\sqrt{m/(2k_B T)}$ in the calculation. Combining all the parts together we can now express

$$\langle \theta_j(t) \rangle_e = \frac{1}{\kappa_1 \kappa_2} \pi^{3/2} \frac{w^2}{L^2} \frac{1}{\Gamma_D} \sum_m g_m \Omega_m w \left[\frac{\Delta_m + i\gamma/2}{\Gamma_D} \right] \cdot \left(\frac{1}{4} \right) \quad (\text{A.21})$$

where we have assumed $e^{-t\kappa_1/2} \approx e^{-t\kappa_2/2} = 0$. We note that the Faddeeva function for large detuning $\Delta \gg \gamma, \Gamma_D$ can be approximated $w \left[\frac{\Delta_m + i\gamma/2}{\Gamma_D} \right] \approx \frac{i\Gamma_D}{\Delta_m \sqrt{\pi}}$. From this we can calculate for large detuning

$$|\langle \theta_j(t) \rangle|^2 \approx \frac{1}{\kappa_1^2 \kappa_2^2} \pi^2 \frac{w^4}{L^4} \sum_m \frac{g_m \Omega_m}{\Delta_m} \sum_n \frac{g_n \Omega_n}{\Delta_n} \cdot \left(\frac{1}{16} \right) \quad (\text{A.22})$$

The second expression required for the write efficiency and for the number of classical photons is $\langle |\theta_j(t)|^2 \rangle$. Similar to [BZP⁺16] we can write

$$\begin{aligned} \langle |\theta_j(t)|^2 \rangle &= \left(\frac{1}{16} \right) \int_0^t dt'_1 \int_0^{t'_1} dt''_1 \int_0^t dt'_2 \int_0^{t'_2} dt''_2 e^{-\frac{\kappa_2}{2}(t-t'_1)} e^{-\frac{\kappa_1}{2}(t'_1-t''_1)} e^{-\frac{\kappa_2}{2}(t-t'_2)} e^{-\frac{\kappa_1}{2}(t'_2-t''_2)} \\ &\quad \cdot \left\langle \sum_m \sum_n XY_{j,m}^*(t''_1) XY_{j,n}(t''_2) Z_{j,m}^*(t'_1) Z_{j,m}(t'_2) \right\rangle_e \end{aligned} \quad (\text{A.23})$$

where we have defined

$$XY_{j,m}(t) = g_{xy}^{(j,m)}(t) \Omega_{xy}^{(j,m)}(t) \quad (\text{A.24})$$

$$Z_{j,m}(t) = \frac{1 - e^{-2ikz_j(t)}}{-\gamma/2 + i(\Delta_m + k_c v_z^{(j)}(t))} + \frac{1 - e^{2ikz_j(t)}}{-\gamma/2 + i(\Delta_m - k_c v_z^{(j)}(t))} \quad (\text{A.25})$$

We can pull out the sums from the ensemble average. Then we can have again the same expression as [BZP⁺16] and can apply the same strategy, separating into large average parts and small time-dependent perturbations and assuming exponential decay of the correlations with rate Γ .

We note that the decay rate of the correlations in our cell geometry had been found with numerical simulation to be $\Gamma = 1.3v_{thermal}/w$, where $v_{thermal}$ is the average thermal velocity of the atoms.

A.2 Number of classical photons

We follow the calculation from [BZP⁺16] starting from equation (S23)

$$N_{quant} = \langle a^+ a t_{int} \rangle = \frac{1}{16} \kappa_2^2 \kappa_1 N \langle |\theta_j|^2 \rangle_e t_{int} \quad (\text{A.26})$$

where the second equality sign follows from equation (2) of [BZP⁺16]. According to Johannes we still have

$$|\Omega^{(i)}|^2 \cdot t_{int} = N_{clas} \frac{|\tilde{g}_i|^2 4}{\kappa_1} \quad (\text{A.27})$$

Where we have expressed $\Omega^{(i)}$ on a fixed driven transition i as proportional to the number of photons times the single photon Rabi frequency \tilde{g}_i on the transition. (The reference transition for both Ω_i and \tilde{g}_i is e.g. $|4, 4\rangle \rightarrow |5'3'\rangle$) The division with κ_1 comes from the input output relations of the cavity or in other words, we have to take the cavity decay rate into account since the faster this is, the weaker the effective interaction described by Ω_i is. The factor of 4 comes from input/output relations and relation between intensity/amplitude decay rates. We define $\beta' = \frac{|\tilde{g}_i|^2}{|g^{(i)}|^2} = \frac{|\mu_{\tilde{g}_i}|^2}{2|\mu_{g^{(i)}}|^2}$ where μ_k is the Clebsch-Gordan coefficient of transition k and the factor two comes from the fact that the input light is linearly polarized, thus only coupling with half the strength to the σ transition expressed by \tilde{g}_i . This yields

$$N_{clas} = |\Omega^{(i)}|^2 t_{int} \frac{\kappa_1}{4\beta'|g^{(i)}|^2} \quad (\text{A.28})$$

Note that now $g^{(i)}$ is the reference transition $|4, 3\rangle \rightarrow |5'3'\rangle$. We insert eq. A.26, eliminating t_{int} , and get

$$N_{clas} = |\Omega^{(i)}|^2 \frac{16N_{quant}}{\kappa_2^2 \kappa_1 N \langle |\theta_j|^2 \rangle_e} \frac{\kappa_1}{4\beta'|g^{(i)}|^2} \quad (\text{A.29})$$

We set $N_{quant} = 1$, approximate $\langle |\theta_j|^2 \rangle_e = |\langle \theta_j \rangle|^2$ and use its approximation for large detuning.

$$N_{clas} = \frac{64 L^4 \kappa_1^2}{\pi^2 N w^4} \frac{1}{\beta'|g^{(i)}|^4} \frac{1}{\left| \sum_m \frac{g^{(m)} \Omega^{(m)}}{g^{(i)} \Omega^{(i)}} \frac{1}{\Delta_m} \right|^2} \quad (\text{A.30})$$

This can also be written in terms of the cell cavity Finesse F and round trip time τ with $\kappa_1 = 2\pi/(\tau F)$

$$N_{clas} = \frac{256 L^4}{N w^4 \tau^2 F^2} \frac{1}{\beta'|g^{(i)}|^4} \frac{1}{\left| \sum_m \frac{g^{(m)} \Omega^{(m)}}{g^{(i)} \Omega^{(i)}} \frac{1}{\Delta_m} \right|^2} \quad (\text{A.31})$$

A.3 N_{clas} in terms of optical depth

Expressing N_{clas} in terms of the optical depth requires on (S18) and (S19) of [BZP⁺16]. Where do those two equations come from and how do they need to be changed? We usually measure the optical depth with π -polarized light, therefore the derivation of (S18) in the paper should still hold true. We will have a close look on how to get from (S18) to (S19). We start from (S18)

$$d = \frac{N\tau}{\gamma} \frac{\pi w^2}{8L^2} (|\tilde{g}_1^{(d)}|^2 + |\tilde{g}_2^{(d)}|^2) \quad (\text{A.32})$$

where $\tau = 2L_{cav}/c$. We have added the index d to distinguish that these coupling coefficients are for the π -polarized transitions used for the optical depth measurement. ($|4, 4\rangle \rightarrow |5', 4'\rangle$ and $|4, 4\rangle \rightarrow |4', 4'\rangle$) We use the definition of the atom-single mode coupling [TSLSS⁺11]

$$|\tilde{g}_n^{(d)}|^2 = d_{g,e_n}^2 \frac{\omega}{2\hbar\epsilon_0 V} \quad (\text{A.33})$$

where V is the cavity mode volume. According to [TSLSS⁺11] this can be written as

$$V = \int \exp(-2\rho^2/w^2) \sin^2(k_0 z) 2\pi\rho d\rho dz = \frac{\pi w^2}{4} L_{cav} \quad (\text{A.34})$$

Furthermore we have the reduced dipole matrix element

$$d_{g,e_n}^2 = \frac{3\pi\epsilon_0 \hbar c^3}{\omega^3} \gamma_{0,n}^{(d)} \quad (\text{A.35})$$

Combining the three above equations yields

$$|\tilde{g}_n^{(d)}|^2 = \frac{6c^3}{\omega^2} \gamma_{0,n}^{(d)} \frac{1}{w^2 L_{cav}} \quad (\text{A.36})$$

Inserting this into the first equation of this subsection gives

$$d = \frac{6\pi c^2}{(2L)^2 \omega^2} \frac{1}{\gamma} \sum_n \gamma_{0,n}^{(d)} = \frac{6\pi \tilde{\lambda}^2}{(2L)^2} \frac{1}{\gamma} \sum_n \gamma_{0,n}^{(d)} \quad (\text{A.37})$$

where we have reached (S19) by using the rescaled wavelength $\tilde{\lambda} = \lambda/(2\pi)$.

We can use (S18) to relate optical depth and number of atoms via the coupling strength. Now we would like to solve the equation for the coupling strength. We define

$$\beta'_2 = \frac{|\tilde{g}_1^{(d)}|^2 + |\tilde{g}_2^{(d)}|^2}{|g^{(i)}|^2} \quad (\text{A.38})$$

and can then rewrite (S18) as

$$|g^{(i)}|^2 = \frac{\sum_n |\tilde{g}_n^{(d)}|^2}{\beta_2'^2} = \frac{8L^2\gamma d}{N\tau\pi\omega^2\beta_2'^2} \quad (\text{A.39})$$

From this we can calculate $|g^{(i)}|^4$ and insert it into the previous equation for N_{clas} yielding

$$N_{clas} = \frac{64N\pi^2}{\gamma^2 d^2 F^2} \frac{\beta_2'^2}{\beta'} \frac{1}{\left| \sum_m \frac{g^{(m)}\Omega^{(m)}}{g^{(i)}\Omega^{(i)}} \frac{1}{\Delta_m} \right|^2} \quad (\text{A.40})$$

This now depends on the number of atoms N and the optical depth d . Both of them can be inferred from the measured Faraday angle.

Tables of cavity specifications

We list the following cavity specifications: L_{RT} Roundtrip length, L length, FSR free spectral range, FWHM full width at half maximum, R reflectivity, ROC radius of curvature, $t(I_0/e)$ intensity decay time, T_{res} transmission on resonance, $T(2.382\text{ MHz})$ transmission at 2.382 MHz detuning.

Cavity	Parameter	Value	Comment
FCav	L_{RT}	1.49201 m	designed
	FSR	200.93 MHz	from L_{RT}
	R_{flat}	99.91%	Manufact. specs for s-pol. [M85]
	R_{curved}	99.995%	Manufact. specs for 0° AOI [M86]
	ROC	1 m	Manufacturer specs [M86]
	$t(I_0/e)$	$(2.4 \pm 0.04) \mu\text{s}$	Ringdown [9-3-2017]
	FWHM	66 kHz	From ringdown
	T_{res}	66%	[31-1-2017]
	$T(2.382\text{ MHz})$	$1.92 \cdot 10^{-4} T_{res}$	Theory
XCav	L_{RT}	198 mm	drawing (ext. vers.) [10-1-2017]
	FSR	1514 MHz	from L_{RT}
	R_{flat}	99.91%	Manufact. specs for s-pol. [M85]
	R_{curved}	99.996%	Manufact. specs for 0° AOI [M84]
	ROC	5 m	Manufact. specs [M84]
	FWHM	894 kHz	spectrum w. sidebands [10-1-2017]
	T_{res}	90%	[31-1-2017]
		$T(2.382\text{ MHz})$	$3.52 \cdot 10^{-2} T_{res}$

Table B.1: Specifications of all the filter cavity (FCav) and extra cavity (XCav). Comments for internal use.

Cavity	Parameter	Value	Comment
CCav	L	0.218 m	measured
	FSR	688 MHz	from L
	R_{in}	0.997	Manufacturer specs [M83]
	$R_{in,895}$	0.992	Manufacturer specs [M83]
	R_{out}	0.8	Manufacturer specs [M83]
	$R_{out,895}$	0.77	Manufacturer specs [M83]
	ROC_{in}	110 mm	Manufacturer specs
	ROC_{out}	110 mm	Manufacturer specs
	Finesse	≈ 18	From full spectrum [05-09-2017]
	FWHM	38 MHz	From L and finesse
	T_{res}	1.4%	[31-1-2017]
LCav	L_{RT}	1.49405 m	designed
	FSR	200.658 MHz	from L_{RT}
	R_{flat}	99.91%	Manufact. specs for s-pol. [M85]
	R_{curved}	99.996%	Manufact. specs for 0° AOI [M84]
	ROC	5 m	Manufact. specs [M84]
	FWHM	72 ± 5 kHz	From ringdown [Karsten's thesis]

Table B.2: Specifications of the cell cavity (CCav) and the lock cavity (LCav). Comments for internal use.

Bibliography

- [ADR82] Alain Aspect, Jean Dalibard, and Gérard Roger. Experimental Test of Bell’s Inequalities Using Time-Varying Analyzers. *Phys. Rev. Lett.*, 49(25):1804–1807, dec 1982.
- [AFFG⁺14] Boris Albrecht, Pau Farrera, Xavier Fernandez-Gonzalvo, Matteo Cristiani, and Hugues de Riedmatten. A waveguide frequency converter connecting rubidium-based quantum memories to the telecom C-band. *Nature Communications*, 5:3376, feb 2014.
- [Alb15] Boris Albrecht. *Quantum control of single spin excitations in cold atomic quantum memories*. PhD thesis, Universitat Politècnica de Catalunya, 2015.
- [BB84] C H Bennett and G Brassard. Quantum cryptography: Public key distribution and coin tossing. *Proceedings of the IEEE International Conference on Computers, Systems and Signal Processing, Bangalore, India*, 1:175–179, 1984.
- [BBC⁺93] Charles H Bennett, Gilles Brassard, Claude Crépeau, Richard Jozsa, Asher Peres, and William K Wootters. Teleporting an unknown quantum state via dual classical and Einstein-Podolsky-Rosen channels. *Phys. Rev. Lett.*, 70(13):1895–1899, mar 1993.
- [BBV⁺14] Erwan Bimbard, Rajiv Boddeda, Nicolas Vitrant, Andrey Grankin, Valentina Parigi, Jovica Stanojevic, Alexei Ourjoumtsev, and Philippe Grangier. Homodyne Tomography of a Single Photon Retrieved on Demand from a Cavity-Enhanced Cold Atom Memory. *Physical Review Letters*, 112(3):33601, jan 2014.
- [BDCZ98] H.-J. Briegel, W Dür, J I Cirac, and P Zoller. Quantum Repeaters: The Role of Imperfect Local Operations in Quantum Communication. *Physical Review Letters*, 81(26):5932–5935, 1998.

- [Bel64] J S Bell. On the Einstein-Podolsky-Rosen paradox. *Physics*, 1:195–200, 1964.
- [BFMP13] J C Bienfang, J Fan, A Migdall, and S V Polyakov. Chapter 1 - Introduction. In Alan Migdall, Sergey V Polyakov, Jingyun Fan, and Joshua C B T Experimental Methods in the Physical Sciences Bienfang, editors, *Single-Photon Generation and Detection*, volume 45, pages 1–24. Academic Press, 2013.
- [BFV12] Mark Bashkansky, Fredrik K Fatemi, and Igor Vurgaftman. Quantum memory in warm rubidium vapor with buffer gas. *Optics Letters*, 37(2):142, jan 2012.
- [BHK⁺05] D Budker, L Hollberg, D F Kimball, J Kitching, S Pustelny, and V V Yashchuk. Microwave transitions and nonlinear magneto-optical rotation in anti-relaxation-coated cells. *Phys. Rev. A*, 71(1):12903, jan 2005.
- [BKK⁺15] J Borregaard, P Kómár, E M Kessler, M D Lukin, and A S Sørensen. Long-distance entanglement distribution using individual atoms in optical cavities. *Phys. Rev. A*, 92(1):12307, jul 2015.
- [BKLB10] M V Balabas, T Karaulanov, M P Ledbetter, and D Budker. Polarized Alkali-Metal Vapor with Minute-Long Transverse Spin-Relaxation Time. *Physical Review Letters*, 105(7):70801, aug 2010.
- [BPM⁺97] Dik Bouwmeester, Jian-Wei Pan, Klaus Mattle, Manfred Eibl, Harald Weinfurter, and Anton Zeilinger. Experimental quantum teleportation. *Nature*, 390:575, dec 1997.
- [BR07] Dmitry Budker and Michael Romalis. Optical magnetometry. *Nature Physics*, 3:227, apr 2007.
- [BT56] R Hanbury Brown and R Q Twiss. Correlation between Photons in two Coherent Beams of Light. *Nature*, 177:27, jan 1956.
- [BZP⁺16] J Borregaard, M Zugenmaier, J M Petersen, H Shen, G Vasilakis, K Jensen, E S Polzik, and A S Sørensen. Scalable photonic network architecture based on motional averaging in room temperature gas. *Nature Communications*, 7:11356, apr 2016.
- [CBB⁺14] S L Christensen, J.-B. Béguin, E Bookjans, H L Sørensen, J H Müller, J Appel, and E S Polzik. Quantum interference of a single spin excitation with a macroscopic atomic ensemble. *Phys. Rev. A*, 89(3):33801, mar 2014.

- [CdRF⁺05] C W Chou, H de Riedmatten, D Felinto, S V Polyakov, S J van Enk, and H J Kimble. Measurement-induced entanglement for excitation stored in remote atomic ensembles. *Nature*, 438:828, dec 2005.
- [Chr14] Stefan Lund Christensen. *Generation of exotic quantum states of a cold atomic ensemble*. PhD thesis, University of Copenhagen, 2014.
- [CHSH69] John F Clauser, Michael A Horne, Abner Shimony, and Richard A Holt. Proposed Experiment to Test Local Hidden-Variable Theories. *Phys. Rev. Lett.*, 23(15):880–884, 1969.
- [CKBB13] Eric P. Corsini, Todor Karaulanov, Mikhail Balabas, and Dmitry Budker. Hyperfine frequency shift and Zeeman relaxation in alkali-metal-vapor cells with antirelaxation alkene coating. *Physical Review A*, 87(2):022901, 2013.
- [CL01] J Calsamiglia and N Lütkenhaus. Maximum efficiency of a linear-optical Bell-state analyzer. *Applied Physics B*, 72(1):67–71, 2001.
- [Cla74] John F Clauser. Experimental distinction between the quantum and classical field-theoretic predictions for the photoelectric effect. *Physical Review D*, 9(4):853–860, feb 1974.
- [CLD⁺07] C.-W. Chou, L Laurat, H Deng, K S Choi, H de Riedmatten, D Felinto, and H J Kimble. Functional Quantum Nodes for Entanglement Distribution over Scalable Quantum Networks. *Science*, 316:1316–1320, 2007.
- [CUB⁺11] Christoph Clausen, Imam Usmani, Félix Bussi eres, Nicolas Sangouard, Mikael Afzelius, Hugues de Riedmatten, and Nicolas Gisin. Quantum storage of photonic entanglement in a crystal. *Nature*, 469:508, jan 2011.
- [CW12] Radosław Chrapkiewicz and Wojciech Wasilewski. Generation and delayed retrieval of spatially multimode Raman scattering in warm rubidium vapors. *Optics Express*, 20(28):29540–29552, 2012.
- [DCW14] Michal Dabrowski, Radoslaw Chrapkiewicz, and Wojciech Wasilewski. Hamiltonian design in readout from room-temperature Raman atomic memory. *Optics Express*, 22(21):26076, 2014.
- [Dic54] R H Dicke. Coherence in Spontaneous Radiation Processes. *Physical Review*, 93(1):99–110, jan 1954.

- [Did14a] Karsten Bjerrum Dideriksen. *A Laser System for a Deterministic Single Photon Source*. Bachelor's thesis, University of Copenhagen, 2014.
- [Did14b] Karsten Bjerrum Dideriksen. *Linewidth Measurement of Near-Infrared Laser Systems*. Technical report, University of Copenhagen, 2014.
- [Did17] Karsten Bjerrum Dideriksen. *Development of a Single-Photon Source with Room-Temperature Atomic Ensembles*. Master's thesis, University of Copenhagen, 2017.
- [DKL⁺14] R Daschner, H Kübler, R Löw, H Baur, N Frühauf, and T Pfau. Triple stack glass-to-glass anodic bonding for optogalvanic spectroscopy cells with electrical feedthroughs. *Applied Physics Letters*, 105(4):41107, jul 2014.
- [DLCZ01] L.-M. Duan, M D Lukin, J I Cirac, and P Zoller. Long-distance quantum communication with atomic ensembles and linear optics. *Nature*, 414:413–418, 2001.
- [DM03] Jonathan P Dowling and Gerard J Milburn. Quantum Technology: The Second Quantum Revolution. *Philosophical Transactions: Mathematical, Physical and Engineering Sciences*, 361(1809):1655–1674, 2003.
- [DYD⁺17] Jian-Peng Dou, Ai-lin Yang, Mu-Yan Du, Di Lao, Jun Gao, Lu-Feng Qiao, Hang Li, Xiao-Ling Pang, Zhen Feng, Hao Tang, and Xian-Min Jin. A Broadband DLCZ Quantum Memory in Room-Temperature Atoms, apr 2017.
- [EAM⁺05] M D Eisaman, A André, F Massou, M Fleischhauer, A S Zibrov, and M D Lukin. Electromagnetically induced transparency with tunable single-photon pulses. *Nature*, 438(7069):837–841, 2005.
- [ED16] Merlin Enault-Dautheribes. *Optically Narrowed Laser Towards the Implementation of a Single-Photon Source on the D1 Line of Caesium*. Master's thesis, University of Copenhagen, 2016.
- [EPR35] A Einstein, B Podolsky, and N Rosen. Can Quantum-Mechanical Description of Physical Reality Be Considered Complete? *Phys. Rev.*, 47(10):777–780, 1935.
- [Fab14] Anne Fabricant. *Quantum-limited optical magnetometry with cesium microcells*. Master's thesis, University of Copenhagen, 2014.
- [Fox06] Mark Fox. *Quantum Optics, An Introduction*. Oxford University Press, Oxford, 2006.

- [FUH⁺09] Alessandro Fedrizzi, Rupert Ursin, Thomas Herbst, Matteo Nespoli, Robert Prevedel, Thomas Scheidl, Felix Tiefenbacher, Thomas Jennewein, and Anton Zeilinger. High-fidelity transmission of entanglement over a high-loss free-space channel. *Nature Physics*, 5:389, may 2009.
- [FVC83] R. P. Frueholz, C. H. Volk, and J. C. Camparo. Use of wall coated cells in atomic frequency standards. *Journal of Applied Physics*, 54(1983):5613–5617, 1983.
- [GALS07a] Alexey V Gorshkov, Axel André, Mikhail D Lukin, and Anders S Sørensen. Photon storage in Λ -type optically dense atomic media. I. Cavity model. *Phys. Rev. A*, 76:33804, 2007.
- [GALS07b] Alexey V Gorshkov, Axel André, Mikhail D Lukin, and Anders S Sørensen. Photon storage in Λ -type optically dense atomic media. III. Effects of inhomogeneous broadening. *Phys. Rev. A*, 76(3):33806, sep 2007.
- [GK05] Christopher Gerry and Peter Knight. *Introductory Quantum Optics*. Cambridge University Press, 2005.
- [GKR⁺05] M T Graf, D F Kimball, S M Rochester, K Kerner, C Wong, D Budker, E B Alexandrov, M V Balabas, and V V Yashchuk. Relaxation of atomic polarization in paraffin-coated cesium vapor cells. *Phys. Rev. A*, 72(2):23401, aug 2005.
- [Gla63] Roy J Glauber. Coherent and Incoherent States of the Radiation Field. *Phys. Rev.*, 131(6):2766–2788, sep 1963.
- [GRA86] P Grangier, G Roger, and A Aspect. Experimental Evidence for a Photon Anticorrelation Effect on a Beam Splitter: A New Light on Single-Photon Interferences. *EPL (Europhysics Letters)*, 1(4):173, 1986.
- [Hay11] Kazuhiro Hayasaka. Modulation-free optical locking of an external-cavity diode laser to a filter cavity. *Optics Letters*, 36(12):2188–2190, 2011.
- [HB10] David Höckel and Oliver Benson. Electromagnetically Induced Transparency in Cesium Vapor with Probe Pulses on the Single-Photon Level. *Physical Review Letters*, 105(15):153605, 2010.
- [HBD⁺15] B Hensen, H Bernien, A E Dréau, A Reiserer, N Kalb, M S Blok, J Ruitenber, R F L Vermeulen, R N Schouten, C Abellán, W Amaya, V Pruneri, M W Mitchell, M Markham, D J Twitchen,

- D Elkouss, S Wehner, T H Taminiau, and R Hanson. Loophole-free Bell inequality violation using electron spins separated by 1.3 kilometres. *Nature*, 526:682, oct 2015.
- [HC80] T W Hänsch and B Couillaud. Laser frequency stabilization by polarization spectroscopy of a reflecting reference cavity. *Optics Communications*, 35(3):441–444, 1980.
- [HCS⁺11] M Hosseini, G Campbell, B M Sparkes, P K Lam, and B C Buchler. Unconditional room-temperature quantum memory. *Nature Physics*, 7(10):794–798, jun 2011.
- [HHH⁺10] Yang Han, Bing He, Khabat Heshami, Cheng-Zu Li, and Christoph Simon. Quantum repeaters based on Rydberg-blockade-coupled atomic ensembles. *Phys. Rev. A*, 81(5):52311, 2010.
- [HK02] D Hirschausen and D M Kane. Laser removal of paraffin wax from glass surfaces. *Journal of Applied Physics*, 92(8):4201–4208, oct 2002.
- [HM86] C K Hong and L Mandel. Experimental realization of a localized one-photon state. *Phys. Rev. Lett.*, 56(1):58–60, jan 1986.
- [HNB12] M Horstjann, V Nenakhov, and J P Burrows. Frequency stabilization of blue extended cavity diode lasers by external cavity optical feedback. *Applied Physics B*, 106:261–266, 2012.
- [HOM87] C K Hong, Z Y Ou, and L Mandel. Measurement of subpicosecond time intervals between two photons by interference. *Phys. Rev. Lett.*, 59(18):2044–2046, nov 1987.
- [HSP10] Klemens Hammerer, Anders S Sørensen, and E S Polzik. Quantum interface between light and atomic ensembles. *Reviews of Modern Physics*, 82(2):1041–1093, apr 2010.
- [Hua09] Bo Huang. *Linewidth Reduction of a Diode Laser by Optical Feedback for Strontium BEC Applications*. PhD thesis, University of Innsbruck, 2009.
- [JBT⁺16] Kasper Jensen, Rima Budvytyte, Rodrigo A Thomas, Tian Wang, Annette M Fuchs, Mikhail V Balabas, Georgios Vasilakis, Lars D Mosgaard, Hans C Stärkind, Jörg H Müller, Thomas Heimburg, Søren-Peter Olesen, and Eugene S Polzik. Non-invasive detection of animal nerve impulses with an atomic magnetometer operating near quantum limited sensitivity. *Scientific Reports*, 6:29638, jul 2016.

- [Jen11] Kasper Jensen. *Quantum information, entanglement and magnetometry with macroscopic gas samples and non-classical light*. PhD thesis, University of Copenhagen, 2011.
- [JKP01] Brian Julsgaard, Alexander Kozhokin, and Eugene S Polzik. Experimental long-lived entanglement of two macroscopic objects. *Nature*, 413(6854):400–403, sep 2001.
- [JSC⁺04] Brian Julsgaard, Jacob Sherson, J Ignacio Cirac, Jaromír Fiurášek, and Eugene S Polzik. Experimental demonstration of quantum memory for light. *Nature*, 432:482, nov 2004.
- [JSSP04] B Julsgaard, J Sherson, J L Sørensen, and E S Polzik. Characterizing the spin state of an atomic ensemble using the magneto-optical resonance method. *Journal of Optics B: Quantum and Semi-classical Optics*, 6(1):5–14, jan 2004.
- [Jul03] Brian Julsgaard. *Entanglement and Quantum Interactions with Macroscopic Gas Samples*. PhD thesis, University of Aarhus, 2003.
- [KBB⁺03] A Kuzmich, W P Bowen, A D Boozer, A Boca, C W Chou, L M Duan, and H J Kimble. Generation of nonclassical photon pairs for scalable quantum communication with atomic ensembles. *Nature*, 423:731–734, 2003.
- [KDM77] H J Kimble, M Dagenais, and L Mandel. Photon Antibunching in Resonance Fluorescence. *Physical Review Letters*, 39(11):691–695, sep 1977.
- [KLB⁺18] K T Kaczmarek, P M Ledingham, B Brecht, S E Thomas, G S Thekkadath, O Lazo-Arjona, J H D Munns, E Poem, A Feizpour, D J Saunders, J Nunn, and I A Walmsley. High-speed noise-free optical quantum memory. *Phys. Rev. A*, 97(4):42316, apr 2018.
- [KMdR17] Kutlu Kutluer, Margherita Mazzera, and Hugues de Riedmatten. Solid-State Source of Nonclassical Photon Pairs with Embedded Multimode Quantum Memory. *Phys. Rev. Lett.*, 118(21):210502, 2017.
- [LCB89] P Laurent, A Clairon, and C Breant. Frequency Noise Analysis of Optically Self-Locked Diode Lasers. *IEEE Journal of Quantum Electronics*, 25(6), 1989.
- [LCD⁺07] J Laurat, K S Choi, H Deng, C W Chou, and H J Kimble. Heralded Entanglement between Atomic Ensembles: Preparation, Decoherence, and Scaling. *Phys. Rev. Lett.*, 99(18):180504, nov 2007.

- [LdRF⁺06] Julien Laurat, Hugues de Riedmatten, Daniel Felinto, Chin-Wen Chou, Erik W Schomburg, and H Jeff Kimble. Efficient retrieval of a single excitation stored in an atomic ensemble. *Optics Express*, 14(15):6912, 2006.
- [LJE⁺17] Cyril Laplane, Pierre Jobez, Jean Etesse, Nicolas Gisin, and Mikael Afzelius. Multimode and Long-Lived Quantum Correlations Between Photons and Spins in a Crystal. *Physical Review Letters*, 118(21):210501, 2017.
- [LRB⁺07] Jaroslaw Labaziewicz, Philip Richerme, Kenneth R Brown, Isaac L Chuang, and Kazuhiro Hayasaka. Compact, filtered diode laser system for precision spectroscopy. *Optics Letters*, 32(5):572–574, 2007.
- [LS69] W E Lamb and M O Scully. The photoelectric effect without photons. *Polarization, Matière et Rayonnement*, 1969.
- [MCS⁺15] P S Michelberger, T F M Champion, M R Sprague, K T Kaczmarek, M Barbieri, X M Jin, D G England, W S Kolthammer, D J Saunders, J Nunn, and I A Walmsley. Interfacing GHz-bandwidth heralded single photons with a warm vapour Raman memory. *New Journal of Physics*, 17, 2015.
- [MKL⁺14] Sreraman Muralidharan, Jungsang Kim, Norbert Lütkenhaus, Mikhail D Lukin, and Liang Jiang. Ultrafast and Fault-Tolerant Quantum Communication across Long Distances. *Phys. Rev. Lett.*, 112(25):250501, jun 2014.
- [MPFB13] Alan Migdall, Sergey V Polyakov, J. Fan, and J C Bienfang. Single-Photon Generation and Detection. In Alan Migdall, Sergey V Polyakov, Jingyun Fan, and Joshua C B T Experimental Methods in the Physical Sciences Bienfang, editors, *Single-Photon Generation and Detection*, volume 45. Academic Press, 2013.
- [MSD⁺12] W J Munro, A M Stephens, S J Devitt, K A Harrison, and Kae Nemoto. Quantum communication without the necessity of quantum memories. *Nature Photonics*, 6:777, oct 2012.
- [MSKT15] Lijun Ma, Oliver Slattery, Paulina Kuo, and Xiao Tang. EIT quantum memory with Cs atomic vapor for quantum communication. In Ronald E Meyers, Yanhua Shih, and Keith S Deacon, editors, *Proc. of SPIE*, page 96150D, sep 2015.
- [NLK⁺13] J Nunn, N K Langford, W S Kolthammer, T F M Champion, M R Sprague, P S Michelberger, X.-M. Jin, D G England, and I A Walmsley. Enhancing Multiphoton Rates with Quantum Memories. *Phys. Rev. Lett.*, 110(13):133601, mar 2013.

- [NMT⁺17] J Nunn, J H D Munns, S Thomas, K T Kaczmarek, C Qiu, A Feizpour, E Poem, B Brecht, D J Saunders, P M Ledingham, Dileep V Reddy, M G Raymer, and I A Walmsley. Theory of noise suppression in Λ -type quantum memories by means of a cavity. *Physical Review A*, 96(1):12338, jul 2017.
- [Pet09] Jonas Meyer Petersen. *An Ion Crystal Quantum Repeater*. Master's thesis, University of Copenhagen, 2009.
- [PGN08] Nathaniel B Phillips, Alexey V Gorshkov, and Irina Novikova. Optimal light storage in atomic vapor. *Physical Review A*, 78(2):23801, aug 2008.
- [POS⁺17] L Podhora, P Obšil, I Straka, M Ježek, and L Slodička. Nonclassical photon pairs from warm atomic vapor using a single driving laser. *Optics Express*, 25(25):31230, nov 2017.
- [Rak00] Malik Rakhmanov. Transfer functions for fields in a 3-mirror nested cavity. *AIP Conference Proceedings*, 523(1):204–207, jun 2000.
- [RDZ⁺10] A G Radnaev, Y O Dudin, R Zhao, H H Jen, S D Jenkins, A Kuzmich, and T A B Kennedy. A quantum memory with telecom-wavelength conversion. *Nature Physics*, 6(11):894–899, 2010.
- [RML⁺11] K F Reim, P Michelberger, K C Lee, J Nunn, N K Langford, and I A Walmsley. Single-Photon-Level Quantum Memory at Room Temperature. *Phys. Rev. Lett.*, 107(5):53603, jul 2011.
- [RW92] F J Raab and S E Whitcomb. Estimation of special optical properties of a triangular ring cavity, 1992.
- [RXY⁺17] Ji-Gang Ren, Ping Xu, Hai-Lin Yong, Liang Zhang, Sheng-Kai Liao, Juan Yin, Wei-Yue Liu, Wen-Qi Cai, Meng Yang, Li Li, Kui-Xing Yang, Xuan Han, Yong-Qiang Yao, Ji Li, Hai-Yan Wu, Song Wan, Lei Liu, Ding-Quan Liu, Yao-Wu Kuang, Zhi-Ping He, Peng Shang, Cheng Guo, Ru-Hua Zheng, Kai Tian, Zhen-Cai Zhu, Nai-Le Liu, Chao-Yang Lu, Rong Shu, Yu-Ao Chen, Cheng-Zhi Peng, Jian-Yu Wang, and Jian-Wei Pan. Ground-to-satellite quantum teleportation. *Nature*, 549:70, aug 2017.
- [RZTN16] Sören Richter, Felix Zimmermann, Andreas Tünnermann, and Stefan Nolte. Laser welding of glasses at high repetition rates - Fundamentals and prospects. *Optics & Laser Technology*, 83:59–66, 2016.

- [SAA⁺10] C Simon, M Afzelius, J Appel, A Boyer de la Giroday, S J Dewhurst, N Gisin, C Y Hu, F Jelezko, S Kröll, J H Müller, J Nunn, E S Polzik, J G Rarity, H De Riedmatten, W Rosenfeld, A J Shields, N Sköld, R M Stevenson, R Thew, I A Walmsley, M C Weber, H Weinfurter, J Wrachtrup, and R J Young. Quantum memories. *The European Physical Journal D*, 58(1):1–22, 2010.
- [SDS09] Nicolas Sangouard, Romain Dubessy, and Christoph Simon. Quantum repeaters based on single trapped ions. *Phys. Rev. A*, 79(4):42340, apr 2009.
- [SEG⁺99] U Schünemann, H Engler, R Grimm, M Weidemüller, and M Zielonkowski. Simple scheme for tunable frequency offset locking of two lasers. *Review of Scientific Instruments*, 70(1):242–243, jan 1999.
- [She14] Heng Shen. *Spin squeezing and entanglement with room temperature atoms for quantum sensing and communication*. PhD thesis, University of Copenhagen, 2014.
- [SKO⁺06] Jacob F Sherson, Hanna Krauter, Rasmus K Olsson, Brian Julsgaard, Klemens Hammerer, Ignacio Cirac, and Eugene S Polzik. Quantum teleportation between light and matter. *Nature*, 443:557, oct 2006.
- [SLDR13] D Sheng, S Li, N Dural, and M V Romalis. Subfemtotesla Scalar Atomic Magnetometry Using Multipass Cells. *Phys. Rev. Lett.*, 110(16):160802, apr 2013.
- [SMC⁺16] D J Saunders, J H D Munns, T F M Champion, C Qiu, K T Kaczmarek, E Poem, P M Ledingham, I A Walmsley, and J Nunn. Cavity-Enhanced Room-Temperature Broadband Raman Memory. *Physical Review Letters*, 116(9):90501, mar 2016.
- [SSB⁺12] P Sekatski, N Sangouard, F Bussièrès, C Clausen, N Gisin, and H Zbinden. Detector imperfections in photon-pair source characterization. *Journal of Physics B: Atomic, Molecular and Optical Physics*, 45(12):124016, 2012.
- [SSdRG11] Nicolas Sangouard, Christoph Simon, Hugues de Riedmatten, and Nicolas Gisin. Quantum repeaters based on atomic ensembles and linear optics. *Reviews of Modern Physics*, 83(1):33–80, mar 2011.
- [SSM⁺14] Neil Sinclair, Erhan Saglamyurek, Hassan Mallahzadeh, Joshua A Slater, Mathew George, Raimund Ricken, Morgan P Hedges, Daniel Oblak, Christoph Simon, Wolfgang Sohler, and

- Wolfgang Tittel. Spectral Multiplexing for Scalable Quantum Photonics using an Atomic Frequency Comb Quantum Memory and Feed-Forward Control. *Physical Review Letters*, 113(5):53603, jul 2014.
- [Ste10] Daniel Adam Steck. *Cesium D Line Data*. available online at <http://steck.us/alkalidata>, revision 2 edition, 2010.
- [Ste13] Martin J Stevens. Chapter 2 - Photon Statistics, Measurements, and Measurements Tools. In Alan Migdall, Sergey V Polyakov, Jingyun Fan, and Joshua C B T Experimental Methods in the Physical Sciences Bienfang, editors, *Single-Photon Generation and Detection*, volume 45, pages 25–68. Academic Press, 2013.
- [Ste15] Daniel Adam Steck. *Quantum and Atom Optics*. available online at <http://steck.us/teaching>, 2015.
- [STTV07] Jonathan Simon, Haruka Tanji, James K Thompson, and Vladan Vuletić. Interfacing Collective Atomic Excitations and Single Photons. *Phys. Rev. Lett.*, 98:183601, 2007.
- [Sud63] E C G Sudarshan. Equivalence of Semiclassical and Quantum Mechanical Descriptions of Statistical Light Beams. *Phys. Rev. Lett.*, 10(7):277–279, apr 1963.
- [TSLSS⁺11] Haruka Tanji-Suzuki, Ian D Leroux, Monika H Schleier-Smith, Marko Cetina, Andrew T Grier, Jonathan Simon, and Vladan Vuletić. Chapter 4 - Interaction between Atomic Ensembles and Optical Resonators: Classical Description. In E Arimondo, P R Berman, and C C Lin, editors, *Advances in Atomic, Molecular, and Optical Physics*, volume 60 of *Advances In Atomic, Molecular, and Optical Physics*, pages 201–237. Academic Press, 2011.
- [VB13] Igor Vurgaftman and Mark Bashkansky. Suppressing four-wave mixing in warm-atomic-vapor quantum memory. *Physical Review A*, 87(6):63836, jun 2013.
- [vdWEA⁺03] C H van der Wal, M D Eisaman, A André, R L Walsworth, D F Phillips, A S Zibrov, and M D Lukin. Atomic Memory for Correlated Photon States. *Science*, 301(July):196–200, 2003.
- [WEA⁺07] P Walther, M D Eisaman, A André, F Massou, M Fleischhauer, A S Zibrov, and M D Lukin. Generation of Narrow-Bandwidth Single Photons Using Electromagnetically Induced Transparency in Atomic Ensembles. *International Journal of Quantum Information*, 05(01n02):51–62, feb 2007.

- [WZ82] W K Wootters and W H Zurek. A single quantum cannot be cloned. *Nature*, 299:802, oct 1982.
- [YCZ⁺08] Zhen-Sheng Yuan, Yu-Ao Chen, Bo Zhao, Shuai Chen, Jörg Schmiedmayer, and Jian-Wei Pan. Experimental demonstration of a BDCZ quantum repeater node. *Nature*, 454:1098, aug 2008.
- [YWBP16] Sheng-jun Yang, Xu-jie Wang, Xiao-hui Bao, and Jian-wei Pan. An efficient quantum light-matter interface with sub-second lifetime. *Nature Photonics*, 10(6):381–384, 2016.
- [ZDS⁺18] M Zugenmaier, K. B. Dideriksen, A. S. Sørensen, B Albrecht, and E. S. Polzik. Long-lived non-classical correlations for scalable quantum repeaters at room temperature. *ArXiv e-prints*, 1801.03286, 2018.
- [ZGS⁺17] Lingbang Zhu, Xianxin Guo, Chi Shu, Heejeong Jeong, and Shengwang Du. Bright narrowband biphoton generation from a hot rubidium atomic vapor cell. *Applied Physics Letters*, 110(16):161101, apr 2017.
- [ZHA⁺15] Manjin Zhong, Morgan P Hedges, Rose L Ahlefeldt, John G Bartholomew, Sarah E Beavan, Sven M Wittig, Jevon J Longdell, and Matthew J Sellars. Optically addressable nuclear spins in a solid with a six-hour coherence time. *Nature*, 517(7533):177–180, jan 2015.